



**HAL**  
open science

## Interplay of Protein Disorder in Retinoic Acid Receptor Heterodimer and Its Corepressor Regulates Gene Expression

Tiago N Cordeiro, Nathalie Sibille, Pierre Germain, Philippe Barthe, Abdelhay Boulahtouf, Frédéric Allemand, Rémy Bailly, Valérie Vivat, Christine Ebel, Alessandro Barducci, et al.

► **To cite this version:**

Tiago N Cordeiro, Nathalie Sibille, Pierre Germain, Philippe Barthe, Abdelhay Boulahtouf, et al.. Interplay of Protein Disorder in Retinoic Acid Receptor Heterodimer and Its Corepressor Regulates Gene Expression. *Structure*, 2019, 27 (8), pp.1270-1285.e6. 10.1016/j.str.2019.05.001 . hal-03078485

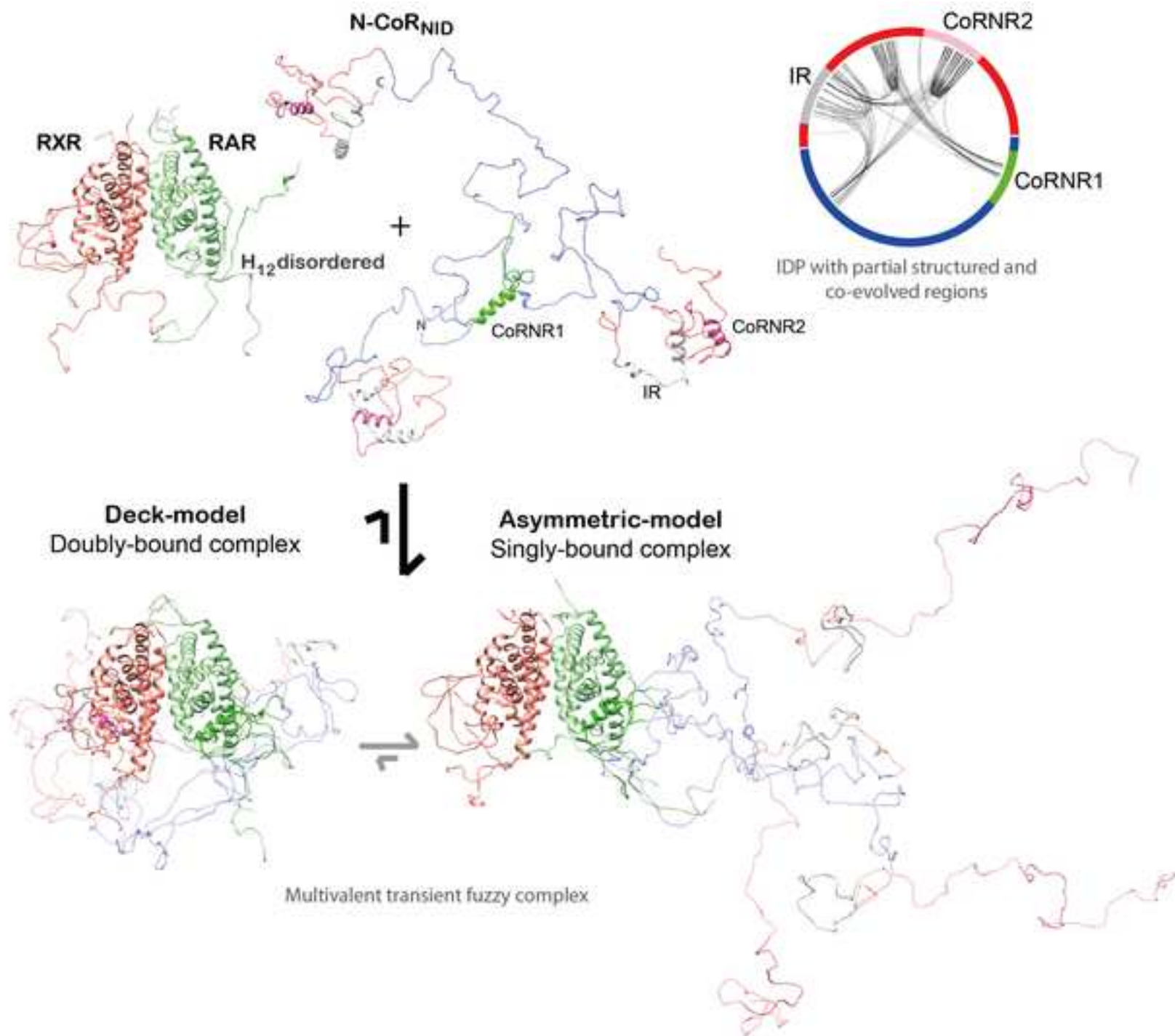
**HAL Id: hal-03078485**

**<https://hal.univ-grenoble-alpes.fr/hal-03078485>**

Submitted on 16 Dec 2020

**HAL** is a multi-disciplinary open access archive for the deposit and dissemination of scientific research documents, whether they are published or not. The documents may come from teaching and research institutions in France or abroad, or from public or private research centers.

L'archive ouverte pluridisciplinaire **HAL**, est destinée au dépôt et à la diffusion de documents scientifiques de niveau recherche, publiés ou non, émanant des établissements d'enseignement et de recherche français ou étrangers, des laboratoires publics ou privés.



1 **Interplay of protein disorder in retinoic acid receptor heterodimer and its**  
2 **corepressor regulates gene expression**

3  
4  
5 3

6  
7 4 Tiago N. Cordeiro<sup>1,2</sup>, Nathalie Sibille<sup>1</sup>, Pierre Germain<sup>1</sup>, Philippe Barthe<sup>1</sup>, Abdelhay  
8  
9 5 Boulahtouf<sup>3</sup>, Frédéric Allemand<sup>1</sup>, Rémy Bailly<sup>1</sup>, Valérie Vivat<sup>4</sup>, Christine Ebel<sup>5</sup>,  
10  
11 6 Alessandro Barducci<sup>1</sup>, William Bourguet<sup>1</sup>, Albane le Maire<sup>1,6,\*</sup>, Pau Bernadó<sup>1,7,\*</sup>

12  
13  
14 7

15  
16  
17 8 <sup>1</sup>Centre de Biochimie Structurale (CBS). CNRS, INSERM, Université de Montpellier.  
18  
19 9 29, rue de Navacelles. 34090 Montpellier, France

20  
21  
22 10 <sup>2</sup>Instituto de Tecnologia Química e Biológica, Universidade Nova de Lisboa, 2790-  
23  
24 11 157 Oeiras, Portugal

25  
26 12 <sup>3</sup>IRCM, INSERM, ICM, Univ Montpellier, 34298 Montpellier, France

27  
28  
29 13 <sup>4</sup>NovAliX, 67400 Illkirch, France

30  
31 14 <sup>5</sup>IBS, Univ. Grenoble Alpes, CEA, CNRS, 38000 Grenoble, France

32  
33  
34 15 <sup>6</sup>Brazilian Biosciences National Laboratory (LNBio), Brazilian Center for Research in  
35  
36 16 Energy and Materials (CNPEM), 13083-970 Campinas, Sao Paulo, Brazil.

37  
38  
39 17 <sup>7</sup>Lead contact

40  
41 18 \*Correspondence: [albane.lemaire@cbs.cnrs.fr](mailto:albane.lemaire@cbs.cnrs.fr); [pau.bernado@cbs.cnrs.fr](mailto:pau.bernado@cbs.cnrs.fr)

42  
43  
44 19

45  
46 20

1  
2  
3  
4  
5  
6  
7  
8  
9  
10  
11  
12  
13  
14  
15  
16  
17  
18  
19  
20  
21  
22  
23  
24  
25  
26  
27  
28  
29  
30  
31  
32  
33  
34  
35  
36  
37  
38  
39  
40  
41  
42  
43  
44  
45  
46  
47  
48  
49  
50  
51  
52  
53  
54  
55  
56  
57  
58  
59  
60  
61  
62  
63  
64  
65

## 21 **Summary**

22 In its unliganded form, the retinoic acid receptor (RAR) in heterodimer with the  
23 retinoid X receptor (RXR) exerts a strong repressive activity facilitated by the  
24 recruitment of transcriptional corepressors in the promoter region of target genes. By  
25 integrating complementary structural, biophysical, and computational information, we  
26 demonstrate that intrinsic disorder is a required feature for the precise regulation of  
27 RAR activity. We show that structural dynamics of RAR and RXR H12 regions is an  
28 essential mechanism for RAR regulation. Unexpectedly, we found that, while mainly  
29 disordered, the corepressor N-CoR presents evolutionary conserved structured regions  
30 involved in transient intramolecular contacts. In the presence of RXR/RAR, N-CoR  
31 exploits its multivalency to form a cooperative multi-site complex that displays an  
32 equilibrium between different conformational states, that can be tuned by cognate  
33 ligands and receptor mutations. This equilibrium is key to preserve the repressive  
34 basal state while allowing the conversion to a transcriptionally active form.

## 36 **Introduction**

37 Nuclear Receptors (NRs) are transcription factors that have a direct role in  
38 regulating the expression of ligand-responsive genes. This regulatory capacity of NRs  
39 occurs through their ability to recognize specific sequences in the promoters of their  
40 target genes and their relationships with the RNA polymerase II holocomplex as well  
41 as the chromatin environment that surrounds these genes (Roeder, 1998). Like many  
42 other members of the NR family, retinoic acid receptors (NR1B1 (RAR $\alpha$ ), NR1B2  
43 (RAR $\beta$ ) and NR1B3 (RAR $\gamma$ )) form heterodimeric complexes with the retinoid X  
44 receptors (NR2B1 (RXR $\alpha$ ), NR2B2 (RXR $\beta$ ) and NR2B3 (RXR $\gamma$ )) and function as  
45 ligand (retinoic acid)-regulated transcription factors (Gronemeyer et al., 2004; Perissi

1  
2  
3  
4  
5  
6  
7  
8  
9  
10  
11  
12  
13  
14  
15  
16  
17  
18  
19  
20  
21  
22  
23  
24  
25  
26  
27  
28  
29  
30  
31  
32  
33  
34  
35  
36  
37  
38  
39  
40  
41  
42  
43  
44  
45  
46 and Rosenfeld, 2005). In fact, RXR/RAR heterodimers may act either as repressors or  
47 activators of gene transcription depending on their ligation status that in turn  
48 determines the ability of these DNA-bound receptors to recruit coregulators (either  
49 corepressors or coactivators) to target gene promoters (Perissi and Rosenfeld, 2005).  
50 Coactivator recruitment is usually ligand-dependent, whereas corepressors interact in  
51 most cases with unliganded (apo) receptors.

52 RARs and RXRs have a conserved modular structure with an N-terminal  
53 activation function (AF-1), a central DNA-binding domain (DBD) and a C-terminal  
54 ligand-binding domain (LBD) (Germain et al., 2006). The multifunctional LBD is  
55 responsible for ligand binding and dimerization and contains a ligand-dependent  
56 activation function (AF-2), which corresponds to coregulator interaction surfaces that  
57 can be modulated by natural (e.g. retinoic acid) or pharmacological ligands  
58 (Gronemeyer et al., 2004). Over the years, different classes of synthetic ligands have  
59 been generated to induce or repress gene transcription. While agonists enhance the  
60 recruitment of coactivators and destabilize interaction with corepressors, thus  
61 inducing the transcription of target genes, inverse agonists do the opposite, decreasing  
62 the basal transcriptional activity of apo-receptors (Germain et al., 2002; le Maire et  
63 al., 2012). Neutral antagonists inhibit both interactions and block the receptor in an  
64 inactive conformation.

46  
47  
48  
49  
50  
51  
52  
53  
54  
55  
56  
57  
58  
59  
60  
61  
62  
63  
64  
65  
66 In the absence of ligand or in the presence of inverse agonists, RAR $\alpha$  (named  
67 RAR hereafter) exhibits strong repressive activity that is brought about by the  
68 recruitment of corepressors (Glass and Rosenfeld, 2000; McKenna et al., 1999;  
69 Germain et al., 2002; Germain et al., 2009; le Maire et al., 2010). The two main  
70 corepressors, Nuclear receptor CoRepressor (N-CoR/NCoR1/RIP13) (Hörlein et al.,  
1995) and the Silencing Mediator of Retinoic acid receptor and Thyroid hormone

1  
2  
3  
4  
5  
6  
7  
8  
9  
10  
11  
12  
13  
14  
15  
16  
17  
18  
19  
20  
21  
22  
23  
24  
25  
26  
27  
28  
29  
30  
31  
32  
33  
34  
35  
36  
37  
38  
71 receptors (SMRT/NCoR2/TRAC) (Chen and Evans, 1995), have been shown to reside  
72 in, or recruit, high molecular weight complexes that display histone deacetylase  
73 activity (Heinzel et al., 1997; Nagy et al., 1997). Deacetylated histones are associated  
74 with silent regions of the genome, and it is generally accepted that histone acetylation  
75 and deacetylation shuffle nucleosomal targets between a relaxed and condensed  
76 chromatin configuration, the former being requisite for transcriptional activation.  
77 From a mechanistic point of view, ligand binding to receptors induces a  
78 rearrangement of the C-terminal region of the LBD, the so-called helix H12, leading  
79 to corepressor dissociation and coactivator recruitment. Coactivators, such as those of  
80 the TIF-2/SRC-1/RAC3 (p160) family, mediate the interaction of coactivator  
81 complexes with NRs. CBP, p300, P/CAF, and some p160 coactivators themselves are  
82 reported to act as histone acetyltransferases (HATs) (Glass and Rosenfeld, 2000;  
83 Lonard and O'Malley, 2007). They are capable of acetylating specific residues in the  
84 N-terminal tails of different histones, a process that is believed to play an important  
85 role in the opening of chromatin during transcription activation (Chen and Evans,  
86 1995; Imhof et al., 1997).

39  
40  
41  
42  
43  
44  
45  
46  
47  
48  
49  
50  
51  
52  
53  
54  
55  
56  
57  
58  
59  
60  
61  
62  
63  
64  
65  
87 Like many proteins in signaling pathways, coregulators are mainly disordered  
88 proteins that act as a platform where multiple proteins attach to perform activities  
89 linked to gene transcription (Csizmok et al., 2016; Hegyi et al., 2007). These  
90 interactions are mediated by Short Linear Motifs (SLiMs) that are embedded in the  
91 sequence and that enable the simultaneous recognition of multiple partners (Van Roey  
92 et al., 2014). Regarding the interaction with NRs, two major conserved  
93 corepressor/NR recognition motifs (CoRNR box 1-2) LxxI/HIxxxI/L have been  
94 identified in SMRT and N-CoR (Hu and Lazar, 1999; Nagy et al., 1999; Perissi et al.,  
95 1999). The boxes, which are close in corepressor sequences, define the NR interaction

1  
2  
3  
4  
5  
6  
7  
8  
9  
10  
11  
12  
13  
14  
15  
16  
17  
18  
19  
20  
21  
22  
23  
24  
25  
26  
27  
28  
29  
30  
31  
32  
33  
34  
35  
36  
37  
38  
39  
40  
41  
42  
43  
44  
45  
46  
47  
48  
49  
50  
51  
52  
53  
54  
55  
56  
57  
58  
59  
60  
61  
62  
63  
64  
65

96 domain (NID). The co-existence of two NR interaction motifs in the NID of  
97 corepressors (multivalency) raises the question of the actual mode of binding to  
98 RXR/RAR heterodimer, namely, whether binding occurs to a single LBD (assymmetric  
99 model) or simultaneously to both LBDs using the two helical motifs (deck model).

100       Important information regarding the molecular mechanisms that regulate the  
101 alternative interactions of RAR LBD, with either class of cofactors has been decoded  
102 by crystallographic studies using short coregulator-derived peptides (Bourguet et al.,  
103 2000; le Maire et al., 2010; Pogenberg et al., 2005). Whereas H12 is primarily  
104 involved in the interaction with coactivators, the discovery of a specific interface  
105 between RAR and a fragment (CoRNR1) of N-CoR revealed that a secondary-  
106 structure transition affecting H11 plays a master role in corepressor association and  
107 release. The constitutive interaction of RAR with corepressors involves: (i) the  
108 formation of an antiparallel  $\beta$ -sheet between  $\beta$ -strand S3 of the receptor and  $\beta$ -strand  
109  $\beta$ 1 of the corepressors, and (ii) the binding of the four-turn  $\alpha$ -helix  $\alpha$ 1 of the  
110 corepressors to the coregulator groove of RAR. Agonist binding induces the S3 to  
111 H11 secondary-structure switch due to the stabilization of the H11 conformation, as  
112 observed in the crystal structure of RAR in complex with the synthetic agonist  
113 AM580 (le Maire et al 2010). On the contrary, in the structure of RAR in complex  
114 with the inverse agonist BMS493 (le Maire et al., 2010), the RAR–corepressor  
115 interaction is strengthened by the stabilization of the  $\beta$ -sheet S3– $\beta$ 1 interface.

116       However, multi-protein complexes containing intrinsically disordered  
117 segments, such as the NID of N-CoR, have an extraordinary structural heterogeneity,  
118 which poses significant technical challenges for their structural characterization.  
119 Indeed, X-ray crystallography is best suited for studies of rigid folded domains and  
120 tightly bound complexes. The application of solution Nuclear Magnetic Resonance

1  
2  
3  
4  
5  
6  
7  
8  
9  
10  
11  
12  
13  
14  
15  
16  
17  
18  
19  
20  
21  
22  
23  
24  
25  
26  
27  
28  
29  
30  
31  
32  
33  
34  
35  
36  
37  
38  
39  
40  
41  
42  
43  
44  
45  
46  
47  
48  
49  
50  
51  
52  
53  
54  
55  
56  
57  
58  
59  
60  
61  
62  
63  
64  
65

121 (NMR), which has been extensively used to study disordered proteins (Dyson and  
122 Wright, 2004; Jensen et al., 2013), encounters severe limitations when characterizing  
123 large biomolecular complexes. Lower resolution methods can synergistically  
124 complement these high-resolution techniques. In particular, small angle X-ray  
125 scattering (SAXS) offers a source of structural and dynamic information for highly  
126 flexible biomolecules (Bernadó and Svergun, 2012; Cordeiro et al., 2017a). Hybrid  
127 approaches, which integrate information from these different techniques into  
128 computational tools are the most promising strategy for the structural characterization  
129 of highly dynamic proteins and complexes in solution. Here, we report on the  
130 structural and dynamic details of the RXR/RAR heterodimer, the disordered NCoR  
131 NID, and the highly flexible complex that they form, by integrating solution  
132 techniques and computational methods.

133         Our study reveals that, in addition of the two CoRNR motifs, a conserved  
134 region of the NID is partially structured and forms transient intramolecular contacts.  
135 Furthermore, we show that NID binds to RXR/RAR through both CoRNR motifs in a  
136 highly cooperative manner inducing an equilibrium between several conformational  
137 states. Perturbations on the individual CoRNR/NR affinities using RAR ligands and  
138 point mutations have a global effect on the structure, dynamics and thermodynamics  
139 of the complex. Moreover, we demonstrate that although both receptors contribute to  
140 the interaction with N-CoR NID, RAR plays a dominant role over RXR. Thus, we  
141 report novel insights into the structural basis of the recruitment of corepressors by  
142 RXR/RAR heterodimer, emphasizing the interplay of N-CoR and H12 helix disorder-  
143 to-order transitions in the regulation of NR-mediated gene transcription.

144  
145

1  
2  
3  
4  
5  
6  
7  
8  
9  
10  
11  
12  
13  
14  
15  
16  
17  
18  
19  
20  
21  
22  
23  
24  
25  
26  
27  
28  
29  
30  
31  
32  
33  
34  
35  
36  
37  
38  
39  
40  
41  
42  
43  
44  
45  
46  
47  
48  
49  
50  
51  
52  
53  
54  
55  
56  
57  
58  
59  
60  
61  
62  
63  
64  
65

146 **Results**

147 **Disorder in RXR/RAR H12 helices is modulated by ligands and mutations.** The  
148 most remarkable observation of the multiple crystallographic structures of RXR and  
149 RAR reported so far is the conformational variability of their C-terminal helices H12  
150 depending on the ligands and cofactors bound (Bourguet et al., 1995; Bourguet et al.,  
151 2000; Chandra et al., 2017; Germain et al., 2002; Germain et al., 2009; le Maire et al.,  
152 2010; Pogenberg et al., 2005; Renaud et al., 1995; Sato et al., 2010). Nuclear  
153 Magnetic Resonance (NMR) and fluorescence anisotropy have also shown the  
154 plasticity of these helices in solution depending on the ligation state (Lu et al., 2006;  
155 Nahoum et al., 2007). Here, we have used SAXS to validate these previous  
156 observations and to analyze other non-crystallized conditions.

157 SAXS data indicate that unliganded RXR/RAR heterodimer is a globular  
158 particle in solution with a radius of gyration,  $R_g$  of  $26.6 \pm 0.4 \text{ \AA}$  and a maximum  
159 intramolecular distance,  $D_{max}$  of  $89.0 \pm 3.0 \text{ \AA}$  (Table S1; Fig. 1A). Molecular weight  
160 estimation suggests that the particle is a heterodimer, in line with Sedimentation  
161 Velocity Analytical Ultracentrifugation (SV-AUC) experiments,  $s_{20w} = 3.78 \pm 0.13 \text{ S}$   
162 and  $f/f_{min} = 1.30 \pm 0.05$  (Fig. S2). The smooth asymmetrical pair-wise distance  
163 distribution,  $P(r)$ , suggests the presence of moderate flexibility in the RXR/RAR  
164 heterodimer (Fig. 1A). Crystallographic structures of RXR/RAR (PDB entries 1DKF  
165 (Bourguet et al., 2000), 1XDK (Pogenberg et al., 2005), and 3A9E (Sato et al., 2010)  
166 (Table S2)), all obtained in the presence of agonist or antagonist of RXR and RAR,  
167 were not consistent with measured SAXS data ( $\chi^2 = 2.55, 2.34$  and  $1.83$ ,  
168 respectively). We hypothesized that the observed discrepancy can be attributed to two  
169 reasons: firstly, the missing flexible regions, including the N- and C-termini and the  
170 loops connecting helices 2 and 3 in both RXR and RAR (Fig. S1B), and secondly, the

171 positions of RXR and RAR H12 helices that are in antagonist or agonist-bound  
172 conformations in the X-ray structures. To validate this hypothesis and based on  
173 several crystallographic structures, we built three ensemble models for the RXR/RAR  
174 heterodimer in which both H12 helices were maintained disordered, in agonist or in  
175 antagonist conformation (see Fig. S1 and methods section for details). SAXS curves  
176 derived from these ensemble models were compared with the experimental one. As  
177 observed in Figure 1 and Figure S1, the average scattering profile computed from the  
178 ensemble model with disordered H12 fragments yielded an excellent agreement to the  
179 experimental curve ( $\chi^2 = 0.77$ ), in accordance with the high propensity of RXR and  
180 RAR H12 sequences to be disordered, in particular in their C-terminal part (Fig.  
181 S1A). The other two alternative ensembles with ordered H12 regions displayed a  
182 small but significant decrease in the agreement to the experimental curve, with  $\chi^2$  of  
183 1.37 and 2.44 for the antagonist and agonist positions, respectively (Fig. S1). These  
184 results indicate that in the unliganded form, H12 helices of both RXR and RAR are  
185 disordered, and highlight the sensitivity of SAXS measurements and analysis to  
186 minute structural changes in the heterodimer.

187 We have exploited this sensitivity to monitor the structural changes in  
188 RXR/RAR induced by the binding of two selective RAR ligands, BMS493 (RAR  
189 inverse agonist) and Am580 (RAR agonist). The presence of these two ligands  
190 induces subtle but noticeable differences in the resulting curves (Fig. 1, Fig. S1 and  
191 Table S1). In the presence of BMS493, the observed  $R_g$ ,  $26.5 \pm 0.3 \text{ \AA}$ , is similar to the  
192 one measured for the unliganded RXR/RAR heterodimer. Conversely, the presence of  
193 Am580 induces a compaction of the particle, with a  $R_g$  of  $25.6 \pm 0.2 \text{ \AA}$ . We have used  
194 the ensemble models based on the available X-ray structures to understand the  
195 structural bases of these differences. Concretely, two ensembles of the heterodimer

196 were built in which RXR H12 was maintained disordered whereas RAR H12 was  
197 assumed disordered or placed in agonist position (see methods section). The average  
198 curves from these ensembles were linearly combined with that of the disordered H12  
199 RAR to optimally describe the measured SAXS curves. SAXS curve of RXR/RAR in  
200 the presence of BMS493 is nicely described ( $\chi^2 = 0.87$ ) with models consisting in a  
201 major contribution (85%) of a fully disordered RAR H12 helix (Fig. 1). Conversely,  
202 in the presence of Am580, SAXS data are in agreement with the 100% of RAR H12  
203 folded in the agonist position ( $\chi^2 = 0.88$ ) (Fig. 1).

204 Similarly, we have analyzed the conformational changes of RAR H12 helix in  
205 the RARI396E point mutant in the context of the heterodimer (RXR/RARI396E).  
206 This point mutation, which was designed based on the crystal structure of the  
207 complex between RAR $\alpha$  and a corepressor peptide, is expected to destabilize the  
208 RAR  $\beta$ -strand S3 conformation and favor a helical conformation in H11, thus  
209 mimicking agonist-induced conformational change (le Maire et al., 2010).  
210 Interestingly, the SAXS analysis indicates that the main heterodimeric species of this  
211 mutant has the RAR H12 in a compact agonistic disposition although a certain  
212 population (~20%) of disordered H12 was also observed ( $\chi^2 = 1.11$ , Fig. 1D). Not  
213 surprisingly, the  $P(r)$  functions of the mutant RXR/RARI396E and Am580-bound  
214 heterodimer are similar, whereas the unliganded RXR/RAR resembles more the  
215 BMS493-bound RXR/RAR (Fig. 1A).

216 In summary, our structural analysis shows that H12 helices of unliganded  
217 RXR/RAR heterodimer are mainly disordered in solution, and that the flexibility of  
218 RAR H12 can be modulated by the presence of specific ligands or mutation. These  
219 observations substantiate the pivotal role of H12 region as a modulator of RAR  
220 activity.

1  
2  
3  
4  
5  
6  
7  
8  
9  
10  
11  
12  
13  
14  
15  
16  
17  
18  
19  
20  
21  
22  
23  
24  
25  
26  
27  
28  
29  
30  
31  
32  
33  
34  
35  
36  
37  
38  
39  
40  
41  
42  
43  
44  
45  
221 **N-CoR<sub>NID</sub> is a disordered protein with evolutionarily conserved and partially**  
222 **structured elements.** We produced and characterized a large fragment of the nuclear  
223 receptor corepressor N-CoR (Hörlein et al., 1995) spanning from residue Gln2059 to  
224 Glu2325. This fragment, N-CoR<sub>NID</sub> from now on, corresponds to the nuclear  
225 interaction domain (NID) of N-CoR and encompasses the two nuclear receptor  
226 binding motifs involved in the interaction of the protein with RXR/RAR heterodimer,  
227 CoRNR1 (from 2065 to 2088) and CoRNR2 (from 2269 to 2291) (Fig. 2). The  
228 biophysical characterization of N-CoR<sub>NID</sub> unambiguously indicates that the protein  
229 behaves as an Intrinsically Disordered Protein (IDP) (Table S3, Fig. S2 and Fig. 2).  
230 Concretely, N-CoR<sub>NID</sub> displays a reduced <sup>1</sup>H dispersion in NMR spectra (Fig. 2A),  
231 and the Kratky plot does not present a clear maximum (Fig. 2B). Moreover, the *s*<sub>20w</sub>  
232 and frictional ratio measured by SV-AUC,  $2.37 \pm 0.19$  S and  $1.53 \pm 0.13$ , are not  
233 compatible with a globular protein of this size ( $\approx 29$  kDa) (Fig. S2). Interestingly, far-  
234 UV Circular Dichroism (CD) measured on N-CoR<sub>NID</sub> presents features that suggest  
235 the presence of helical regions (Fig. 2C). Secondary structure is manifested by a shift  
236 in the negative maximum at 205 nm, rather than at 198 nm for a pure random coil  
237 profile, the negative shoulder near 220 nm, which is more pronounced than that  
238 observed for fully disordered proteins, and the positive signal at 190 nm (Bienkiewicz  
239 et al., 2002).

46  
47  
48  
49  
50  
51  
52  
53  
54  
55  
56  
57  
58  
59  
60  
61  
62  
63  
64  
65  
240 We performed the NMR study of N-CoR<sub>NID</sub> to identify structural features at  
241 the residue level (Fig. 2A). The resonances of backbone nuclei of N-CoR<sub>NID</sub> were  
242 assigned using standard triple resonance spectra at high spectrometer field. Out of the  
243 241 expected <sup>1</sup>H-<sup>15</sup>N HSQC backbone correlation peaks, only 183 could be  
244 unambiguously assigned (Fig. S3). The non-identified correlations were either non-  
245 visible peaks or had extremely low intensities precluding assignment. When mapping

1  
2  
3  
4  
5  
6  
7  
8  
9  
10  
11  
12  
13  
14  
15  
16  
17  
18  
19  
20  
21  
22  
23  
24  
25  
26  
27  
28  
29  
30  
31  
32  
33  
34  
35  
36  
37  
38  
39  
40  
41  
42  
43  
44  
45  
246 the missing peaks on the amino acid sequence of N-CoR<sub>NID</sub>, they clustered in three  
247 non-consecutive regions of the protein (Fig. 2E and Fig. S3B). Interestingly, two of  
248 these clusters were centered in the consensus NR binding domains CoRNR1 and  
249 CoRNR2 and extended towards both flanking regions (Fig. 2E). Furthermore, a third  
250 region, spanning from 2204 to 2234, also displayed absence or systematic decrease of  
251 NMR intensities. Within this third region, which will be named Intermediate Region  
252 (IR) from now on, no correlation peaks could be assigned for the residues 2204-2217  
253 and 2222-2223. We performed <sup>1</sup>H-<sup>15</sup>N HSQC experiments at different temperatures  
254 (283, 288 and 293 K) but the number of peaks in the spectra did not change. Based on  
255 these observations, we attributed the absence or decrease of NMR intensities in these  
256 three regions to the formation of transient secondary structural elements that  
257 experience chemical exchange processes in the  $\mu$ s-*ms* time-scale inducing severe  
258 broadening of the signals. The presence of partially structured regions was  
259 substantiated by the analysis of N-CoR<sub>NID</sub> sequence using several disorder prediction  
260 servers (Fig. 2F). All predictors applied coincided in identifying CoRNR1 and  
261 CoRNR2 as helices and their respective flanking regions as partially structured, both  
262 motifs named as ID1 and ID2, respectively, from now on. Interestingly, disorder  
263 predictors also identify the IR as partially structured, although to a lesser extent  
264 (Buchan et al., 2013).

46  
47  
48  
49  
50  
51  
52  
53  
54  
55  
56  
57  
58  
59  
60  
61  
62  
63  
64  
65  
265 A sequence conservation bioinformatics analysis of N-CoR<sub>NID</sub> fragments from  
266 multiple eukaryotic organisms indicates that ID1 and the large C-terminal region  
267 (LCR, 2190 to 2295), which encompasses IR and ID2, are evolutionarily conserved  
268 (Fig. 2G). On the contrary, the N-terminal region of the N-CoR<sub>NID</sub>, with the exception  
269 of ID1, is poorly conserved as typically observed in IDPs (Ota and Fukuchi, 2017).  
270 Interestingly, the LCR presents a sequence composition that is closer to globular

1  
2  
3  
4  
5  
6  
7  
8  
9  
10  
11  
12  
13  
14  
15  
16  
17  
18  
19  
20  
21  
22  
23  
24  
25  
26  
27  
28  
29  
30  
31  
32  
33  
34  
35  
36  
37  
38  
39  
40  
41  
42  
43  
44  
45  
46  
47  
48  
49  
50  
51  
52  
53  
54  
55  
56  
57  
58  
59  
60  
61  
62  
63  
64  
65

271 proteins according to the charge hydrophathy plot (Uversky and Gillespie, 2000), a  
272 behaviour that is different from the N-terminus (Fig. 2D).

273 **N-CoR<sub>NID</sub> presents intramolecular transient contacts between conserved, co-**  
274 **evolved and partially structured IR and ID2 regions.** The presence of local  
275 compaction and long-range contacts in the partially structured and conserved C-  
276 terminal region of N-CoR<sub>NID</sub> was explored using SAXS, Paramagnetic Relaxation  
277 Enhancement (PRE) NMR experiments, which report on distance-depending induced  
278 relaxation on NMR active nuclei, and Molecular Dynamics simulations (MD). In  
279 addition to the native Cys2074, which sits in the middle of the ID1 motif, Ser2213  
280 (preceding the IR) and Ser2288 (succeeding ID2) were mutated to cysteines. Note that  
281 for these two mutants, the native Cys2074 was mutated into serine (C2074S) to have  
282 only one cysteine at a time in the entire sequence of N-CoR<sub>NID</sub>. After incorporating a  
283 PROXYL stable radical on each of the cysteine residues independently, PRE-ratios  
284 were measured for the three samples. When the paramagnetic moiety was introduced  
285 in native Cys2074, no distal effects were observed, indicating that the N-terminal  
286 region of N-CoR<sub>NID</sub> does not present long-range interactions with the rest of the  
287 protein (Fig. 3A). Conversely, PRE data measured in the two point mutants, S2213C  
288 and S2288C, provide a different picture of N-CoR<sub>NID</sub>. For both single-cysteine  
289 variants, a substantial decrease in intensity is observed for <sup>1</sup>H-<sup>15</sup>N HSQC peaks from  
290 the region between the IR and ID2 indicating the presence of extensive long-range  
291 contacts (Fig. 3A). Interestingly, PREs measured in this region display a bell-shape  
292 with stronger PRE effects in the proximity of both partially structured regions.  
293 Moreover, PRE profiles for both mutants in the LCR are very similar suggesting a  
294 direct interaction between the IR and the ID2 motifs that also affects the connecting  
295 region (Fig. 3A). The compactness of N-CoR<sub>NID</sub> observed by PRE was substantiated

1  
2  
3  
4  
5  
6  
7  
8  
9  
10  
11  
12  
13  
14  
15  
16  
17  
18  
19  
20  
21  
22  
23  
24  
25  
26  
27  
28  
29  
30  
31  
32  
33  
34  
35  
36  
37  
38  
39  
40  
41  
42  
43  
44  
45  
46  
47  
48  
49  
50  
51  
52  
53  
54  
55  
56  
57  
58  
59  
60  
61  
62  
63  
64  
65

296 by SAXS. A simple random coil model built with Flexible-Meccano (Bernado et al.,  
297 2005) could not reproduce the experimental SAXS curve (Fig. 3B). Indeed, the  
298 theoretical ensemble turned out to be more extended than N-CoR<sub>NID</sub> in solution, with  
299  $R_g$  of 50.4 Å and  $47.2 \pm 1.2$  Å for the theoretical and experimental SAXS curves,  
300 respectively.

301         PRE and SAXS data were used to further characterize the structural  
302 compaction observed in N-CoR<sub>NID</sub>. Large ensembles of conformations were built with  
303 Flexible-Meccano to which multiple explicit dispositions of the PROXYL moiety  
304 were attached to the native or engineered cysteine residues. Subsequently, the  
305 theoretical averaged PRE ratios were computed as previously described (Salmon et  
306 al., 2010), and compared with the three experimental PRE profiles (see methods for  
307 details). Not surprisingly, the random coil model only presented contacts in the  
308 vicinity of the paramagnetic sites, and therefore did not reproduce the experimental  
309 profiles especially in the C-terminal region (Fig. 3A, blue lines). In order to interpret  
310 the long-range contacts observed in the LCR, a structurally biased model was built  
311 based on previous experimental and bioinformatics observations. Concretely,  
312 conformations with at least two contacts of  $\leq 15$  Å between residues from distal  
313 regions of the LCR presenting partial structuration (average disorder below 0.5, Fig.  
314 2F), evolutionary conservation (Bits  $\geq 1.6$ , Fig. 2G), or co-evolution (Fig. 3D), were  
315 selected from a large ensemble of random coil conformations. This filtered ensemble  
316 resulted too compact, and it was further refined using the SAXS curve to yield a sub-  
317 ensemble compatible with the scattering profile (Fig. 3B, C), which was subsequently  
318 used to compute the PRE values for the three PROXYL-tagged N-CoR<sub>NID</sub> constructs  
319 and compared with the experimental ones. The resulting theoretical PRE profiles  
320 displayed an excellent agreement with the experimental ones (Fig. 3A, red lines). Not

1  
2  
3  
4  
5  
6  
7  
8  
9  
10  
11  
12  
13  
14  
15  
16  
17  
18  
19  
20  
21  
22  
23  
24  
25  
26  
27  
28  
29  
30  
31  
32  
33  
34  
35  
36  
37  
38  
39  
40  
41  
42  
43  
44  
45  
46  
47  
48  
49  
50  
51  
52  
53  
54  
55  
56  
57  
58  
59  
60  
61  
62  
63  
64  
65

321 surprisingly, a systematic decrease of the PRE values in the LCR compared to the N-  
322 terminal region was observed. More interestingly, PRE fluctuations in the connecting  
323 region between the IR and the ID2 region were nicely reproduced for the S2213C and  
324 S2288C mutants.

325 In order to further investigate the formation of these long-range contacts, we  
326 performed MD simulations of N-CoR<sub>NID</sub> based on a coarse-grained model that was  
327 specifically designed for IDPs (Smith et al., 2014) and takes into account sequence-  
328 specific electrostatic and hydrophobic interactions. The resulting conformational  
329 ensemble, which was not biased by experimental data, revealed that N-CoR<sub>NID</sub>  
330 sequence is poised to form transient yet noticeable interactions in the C-terminal  
331 region. Importantly, the contact matrix derived from coarse-grained MD is in good  
332 agreement with the PRE-derived ensemble (Fig. 3E). These results substantiate the  
333 presence of transient intramolecular contacts between distal regions within the C-  
334 terminal region of N-CoR<sub>NID</sub>. Moreover, these regions present relatively stable  
335 secondary structural elements and a high level of evolutionary conservation.

336 **RXR/RAR heterodimer interacts with the corepressor mainly through RAR and**  
337 **in a cooperative manner.** After characterizing the individual partners, we  
338 investigated the complex between RXR/RAR and N-CoR<sub>NID</sub>. The affinities of  
339 RXR/RAR heterodimer for NCoR peptides encompassing either CoRNR1 or  
340 CoRNR2 motifs and for the N-CoR<sub>NID</sub> fragment were measured by fluorescence  
341 anisotropy and thermophoresis, respectively. As shown in Figure 4, formation of the  
342 RXR/RAR heterodimer does not modify the binding capacity of individual RXR and  
343 RAR monomers for isolated CoRNR peptides. In fact, the RXR/RAR heterodimer  
344 binds the two isolated CoRNR peptides with nearly the same affinity, 1.68 and 1.47  
345  $\mu\text{M}$  for CoRNR1 and CoRNR2, respectively (Fig. 4B). These affinity values are very

1  
2  
3  
4  
5  
6  
7  
8  
9  
10  
11  
12  
13  
14  
15  
16  
17  
18  
19  
20  
21  
22  
23  
24  
25  
26  
27  
28  
29  
30  
31  
32  
33  
34  
35  
36  
37  
38  
39  
40  
41  
42  
43  
44  
45  
46  
47  
48  
49  
50  
51  
52  
53  
54  
55  
56  
57  
58  
59  
60  
61  
62  
63  
64  
65

346 similar to those measured previously (le Maire et al., 2010) for the unliganded RAR  
347 monomer (1.40 and 1.55  $\mu\text{M}$  for peptides encompassing CoRNR1 and CoRNR2,  
348 respectively) (Fig. 4A). The slight preference observed for CoRNR1 is induced by the  
349 ability of this motif to form a  $\beta$ -sheet interface with S3 of RAR $\alpha$ , which is further  
350 stabilized in the presence of the inverse agonist BMS493 with an affinity of 0.17  $\mu\text{M}$ .  
351 Conversely, in its monomeric form, RXR presents a moderate affinity (22.5  $\mu\text{M}$ ) for  
352 CoRNR2, and no measurable interaction with CoRNR1 (Fig. 4A). As expected, the  
353 presence of the RAR-selective agonist Am580 or the RARI396E mutation cause a  
354 noticeable decrease in the affinity of RXR/RAR for both N-CoR peptides with a  
355 stronger effect on CoRNR1 (Fig. 4B). Conversely, the RAR inverse agonist BMS493  
356 efficiently increases the binding affinity of RXR/RAR for CoRNR1, but has not much  
357 effect on the interaction with CoRNR2 (Fig. 4A-B). These observations suggest a  
358 sequential and directional mechanism in which, in the context of N-CoR<sub>NID</sub>,  
359 comprising the two CoRNR motifs, the main anchoring point would involve RAR on  
360 the heterodimer side and CoRNR1 on the N-CoR side. This primary contact would  
361 then enable a second lower-affinity interaction between RXR and CoRNR2.

362         Microscale thermophoresis measurements further substantiated the  
363 cooperativity and directionality of the interaction. The affinity of RXR/RAR  
364 heterodimer for N-CoR<sub>NID</sub> was found to be much higher than for individual peptides  
365 with a value of  $0.21 \pm 0.09 \mu\text{M}$ , to be compared to 1.68 and 1.47  $\mu\text{M}$  for CoRNR1  
366 and CoRNR2, respectively (Fig. 4B-C). The inverse agonist BMS493 or deletion of  
367 RXR helix H12 (RXR $\Delta$ H12), which are known to enhance the interaction of RAR  
368 with CoRNR1 (Germain et al., 2009; le Maire et al., 2010) (Fig. 3A) and that of RXR  
369 for CoRNR2 (Hu and Lazar, 1999), respectively, were shown to increase significantly  
370 the overall affinity of the heterodimer for N-CoR<sub>NID</sub> (Fig. 4C). In contrast, the RAR

1  
2  
3  
4  
5  
6  
7  
8  
9  
10  
11  
12  
13  
14  
15  
16  
17  
18  
19  
20  
21  
22  
23  
24  
25  
26  
27  
28  
29  
30  
31  
32  
33  
34  
35  
36  
37  
38  
39  
40  
41  
42  
43  
44  
45  
46  
47  
48  
49  
50  
51  
52  
53  
54  
55  
56  
57  
58  
59  
60  
61  
62  
63  
64  
65

371 agonist Am580, or the RAR mutation I396E induced a strong decrease of the  
372 affinities with  $K_d$  values of  $8.6 \pm 3.70 \mu\text{M}$  or  $4.42 \pm 1.86 \mu\text{M}$ , respectively, due to the  
373 weakening of the interaction of RAR with CoRNR1 in both cases. The observation  
374 that the perturbation of individual anchoring points has severe consequences on the  
375 affinity of RXR/RAR for N-CoR<sub>NID</sub> demonstrates the cooperativity and directionality  
376 of the complex.

377 **N-CoR<sub>NID</sub> forms a transient multi-site complex with RXR/RAR.** Affinity  
378 measurements indicate that N-CoR<sub>NID</sub> binds cooperatively to RXR/RAR heterodimer.  
379 To unveil the structural bases of this cooperativity, we combined SAXS and NMR to  
380 study the N-CoR<sub>NID</sub>:RXR/RAR heterotrimeric complex.

381 SAXS data indicates that the complex is monodisperse with a  $R_g$  and  $D_{max}$   
382 values of  $48.4 \pm 1.1 \text{ \AA}$  and  $194 \pm 10 \text{ \AA}$ , and with a stoichiometry of 1:1:1 according to  
383 SV-AUC and mass spectrometry data (Table S3, Fig. S2 and Fig. S4). Moreover, the  
384 Kratky representation with elevated baseline at high  $s$ , and asymmetric  $P(r)$  function  
385 suggest that N-CoR<sub>NID</sub>:RXR/RAR has a significant degree of flexibility (Fig. S5).

386 The observation of cooperative effects prompted towards the possibility that  
387 the two binding regions of N-CoR<sub>NID</sub>, CoRNR1 and CoRNR2, could simultaneously  
388 interact with RXR/RAR forming the so-called deck model (le Maire and Bourguet,  
389 2014). The latter scenario is in contrast with the asymmetric model, where a single  
390 corepressor binding side would interact with the RXR/RAR heterodimer as observed  
391 for the complex between RXR/RAR and a fragment of the coactivator Med1 (Rochel  
392 et al., 2011). Ensembles of conformations were built for both the deck and the  
393 asymmetric binding modes (see SI Appendix for details), integrating previous  
394 knowledge of the system. This includes the directionality of the complex derived from  
395 affinity measurements, and two crystallographic structures of RAR and RXR with

1  
2  
3  
4  
5  
6  
7  
8  
9  
10  
11  
12  
13  
14  
15  
16  
17  
18  
19  
20  
21  
22  
23  
24  
25  
26  
27  
28  
29  
30  
31  
32  
33  
34  
35  
36  
37  
38  
39  
40  
41  
42  
43  
44  
45  
46  
47  
48  
49  
50  
51  
52  
53  
54  
55  
56  
57  
58  
59  
60  
61  
62  
63  
64  
65

396 corepressor peptides that were used to define the atomic details of the interacting sites  
397 (Table S2) (le Maire et al., 2010; Zhang et al., 2011). H12 helices from both RXR and  
398 RAR were considered disordered based on our SAXS analysis (see above). Finally,  
399 the non-interacting regions of N-CoR<sub>NID</sub> were assumed to adopt random coil  
400 conformations based on the NMR data (see below). Theoretical SAXS curves were  
401 computed from large ensembles of structures for both interacting modes yielding  
402 notably different profiles (Fig. S6). These curves were optimally combined to derive  
403 the relative population of both interacting modes by minimizing the agreement to the  
404 experimental curve. An excellent agreement ( $\chi^2 = 0.88$ ) to the experimental SAXS  
405 curve of N-CoR<sub>NID</sub>:RXR/RAR was obtained when a 85/15 ratio for the  
406 asymmetric/deck models was used (Fig. 5A, B). This result indicates that both  
407 binding modes coexist in solution although the asymmetric model is the major species  
408 in the absence of ligand. The similarity of the scattering curves between the two  
409 alternative asymmetric models (N-CoR<sub>NID</sub> bound to RAR through ID1 or N-CoR<sub>NID</sub>  
410 bound to RXR through ID2) precludes the identification of the major asymmetric  
411 species.

412 In order to understand the interaction at the residue level, we performed NMR  
413 experiments by adding an equimolar amount of RXR/RAR to a <sup>15</sup>N-isotopically  
414 labeled N-CoR<sub>NID</sub> sample. The NMR <sup>1</sup>H-<sup>15</sup>N HSQC spectrum of N-CoR<sub>NID</sub> presents  
415 correlation peaks that are superimposable to these obtained in the absence of  
416 heterodimer, and no correlation peaks shifted upon the addition of the heterodimer  
417 (Fig. S7). This observation indicates that the conformational properties of N-CoR<sub>NID</sub>  
418 are equivalent in the free and in the bound states, and that N-CoR<sub>NID</sub> remains mostly  
419 disordered when bound to the RXR/RAR heterodimer. However, in the presence of  
420 RXR/RAR, a systematic decrease in peak intensities is observed for N-CoR<sub>NID</sub> when

1  
2  
3  
4  
5  
6  
7  
8  
9  
10  
11  
12  
13  
14  
15  
16  
17  
18  
19  
20  
21  
22  
23  
24  
25  
26  
27  
28  
29  
30  
31  
32  
33  
34  
35  
36  
37  
38  
39  
40  
41  
42  
43  
44  
45  
46  
47  
48  
49  
50  
51  
52  
53  
54  
55  
56  
57  
58  
59  
60  
61  
62  
63  
64  
65

421 compared to the free form (Fig. S7 and Fig. 2E). We attribute this observation to the  
422 perturbation of the hydrodynamic properties of N-CoR<sub>NID</sub> upon binding to the  
423 heterodimer that senses the presence of a large globular particle and increases the  
424 apparent correlation time. Interestingly, the intensity decrease is not homogeneously  
425 distributed along the protein, and two regions of the protein can be clearly  
426 distinguished. The N-terminal region connecting ID1 and the IR presents moderate  
427 intensity decreases that are slightly larger in the proximity of both partially structured  
428 regions. Conversely, the region connecting the IR with ID2 displays a more important  
429 intensity reduction. The transient binding of ID2 to RXR as demonstrated by SAXS  
430 and the change in the dynamic regime for the intra-molecular interactions could  
431 explain the enhanced intensity reduction in the C-terminus. To explore this  
432 phenomenon, we performed PRE experiments for the complexes formed by the  
433 previously described N-CoR<sub>NID</sub> cysteine mutants and the heterodimer RXR/RAR. The  
434 incorporation of radical moieties on the N-CoR<sub>NID</sub> S2213C and S2288C point mutants  
435 induced a sequence-dependent decrease on the PRE ratios of residues placed at their  
436 flanking regions, a phenomenon which is typically observed in IDPs (Fig. 5D, E).  
437 Interestingly, for both mutants a small but systematic increase in the PRE ratios was  
438 found for the N-terminal residues when compared with the PRE data of the free forms  
439 (Fig. 3A). This is most probably caused by the reduced conformational exploration in  
440 N-CoR<sub>NID</sub> when bound to the heterodimer, which limits sporadic contacts of the C-  
441 terminal region with the N-terminus. Compared with the free form of N-CoR<sub>NID</sub>, the  
442 presence of the heterodimer causes a PRE-ratio increase in the region connecting the  
443 IR and ID2, and partially suppresses the above-described bell-shape of PRE ratios.  
444 This increase is not homogeneous and the region around 2250 presents strong PRE  
445 effects. These observations indicate that the population of conformations experiencing

1  
2  
3  
4  
5  
6  
7  
8  
9  
10  
11  
12  
13  
14  
15  
16  
17  
18  
19  
20  
21  
22  
23  
24  
25  
26  
27  
28  
29  
30  
31  
32  
33  
34  
35  
36  
37  
38  
39  
40  
41  
42  
43  
44  
45  
46  
47  
48  
49  
50  
51  
52  
53  
54  
55  
56  
57  
58  
59  
60  
61  
62  
63  
64  
65

446 long-range contacts in the C-terminus is diminished in the bound form. This last  
447 observation is coherent with the existence of a minor population of the deck model  
448 that conformationally restricts N-CoR<sub>NID</sub>, and partially hampers intra-molecular  
449 contacts involving ID2.

450 **Cognate ligands and mutations modulate the conformational equilibrium in the**  
451 **complex.** Thermophoresis experiments demonstrated that the affinity of N-CoR<sub>NID</sub> for  
452 RXR/RAR can be finely tuned by the addition of cognate ligands or by mutations at  
453 the recognition sites of both RXR and RAR. We applied SAXS and NMR to explore  
454 the structural bases of this affinity modulation.

455         The addition of the RAR inverse agonist BMS493 reinforced the interaction of  
456 RXR/RAR with N-CoR<sub>NID</sub> through CoRNR1 (Fig. 4B and 4C). The analysis of the  
457 SAXS curve of the ternary complex in the presence of BMS493 indicates that the  
458 overall size of the particle is slightly reduced with respect to the unliganded form of  
459 the complex,  $R_g = 47.5 \pm 1.0 \text{ \AA}$  (Table S3). The characterization of that curve in terms  
460 of atomistic ensemble models indicated that the asymmetric model is still the major  
461 species but the population of the doubly-bound deck model increases up to 35% (Fig.  
462 6A and 6B). A more extreme situation was observed when the complex was formed  
463 with RXR $\Delta$ H12/RAR that strongly reinforces the overall affinity with N-CoR<sub>NID</sub> by  
464 increasing the interaction of RXR with ID2 (Fig. 4B and 4C). This RXR H12 deletion  
465 renders the RXR hydrophobic groove more accessible and has been reported to  
466 significantly increase the interaction of RXR with corepressor (Hu and Lazar, 1999;  
467 Schulman et al., 1996; Zhang et al., 2011). In that situation, the SAXS curve, which  
468 presented a smaller  $R_g$  of  $42.0 \pm 2 \text{ \AA}$ , could be explained with the only presence of the  
469 deck model (Table S3, Fig. S5 and Fig. 6A and 6B). The <sup>15</sup>N N-CoR<sub>NID</sub> NMR  
470 intensities measured for both complexes, upon addition of RXR/RAR in the presence

1  
2  
3  
4  
5  
6  
7  
8  
9  
10  
11  
12  
13  
14  
15  
16  
17  
18  
19  
20  
21  
22  
23  
24  
25  
26  
27  
28  
29  
30  
31  
32  
33  
34  
35  
36  
37  
38  
39  
40  
41  
42  
43  
44  
45  
46  
47  
48  
49  
50  
51  
52  
53  
54  
55  
56  
57  
58  
59  
60  
61  
62  
63  
64  
65

471 of BMS493 and of RXR $\Delta$ H12/RAR, displayed a systematic decrease with respect to  
472 the unliganded N-CoR<sub>NID</sub>:RXR/RAR (Fig. 6C). We attributed this observation to the  
473 increase of the overall correlation time sensed by N-CoR<sub>NID</sub> when the population of  
474 the deck model increases. This is especially significant in the region close to ID2 that  
475 fits well with the higher interaction of ID2 with RXR $\Delta$ H12. Compared with the  
476 unliganded (Fig. S7), the region connecting the IR and ID2 in the N-  
477 CoR<sub>NID</sub>:RXR $\Delta$ H12/RAR displays a less prominent decrease of intensities, indicating  
478 that some of the structural and/or dynamical properties that cause the decrease in the  
479 native complex are abolished by the formation of a doubly-bound state.

480 We also performed SAXS experiments of the complex N-CoR<sub>NID</sub>:RXR/RAR  
481 in the presence of the RAR agonist Am580, and of the complex N-  
482 CoR<sub>NID</sub>:RXR/RARI396E. Affinity measurements indicated that both conditions  
483 diminished the interaction of RXR/RAR with N-CoR<sub>NID</sub> through CoRNR1 (Fig. 4B  
484 and 4C). The analysis of the SAXS data using explicit models indicated that the  
485 decrease of the interaction has severe structural consequences for both complexes. On  
486 one hand, the SAXS curve measured on N-CoR<sub>NID</sub>:RXR/RAR in the presence of  
487 Am580 can only be described ( $\chi^2 = 0.81$ ) if large populations, 51%, of unbound N-  
488 CoR<sub>NID</sub> and RXR/RAR are invoked (Fig. 6A and 6B), showing that Am580 partially  
489 breaks the complex by diminishing the interaction of CoRNR1 with RAR. Similarly,  
490 the SAXS curve measured for the complex N-CoR<sub>NID</sub>:RXR/RARI396E is optimally  
491 described using a combination of unbound species, asymmetric complex and a low  
492 percentage of deck complex. <sup>15</sup>N N-CoR<sub>NID</sub> NMR intensities measured in these two  
493 conditions were also coherent with SAXS observations (Fig. 6C). The general  
494 increase in these intensities is in line with the presence of a weaker complex with  
495 lower dragging forces and smaller apparent correlation time.

1  
2  
3  
4  
5  
6  
7  
8  
9  
10  
11  
12  
13  
14  
15  
16  
17  
18  
19  
20  
21  
22  
23  
24  
25  
26  
27  
28  
29  
30  
31  
32  
33  
34  
35  
36  
37  
38  
39  
40  
41  
42  
43  
44  
45  
46  
47  
48  
49  
50  
51  
52  
53  
54  
55  
56  
57  
58  
59  
60  
61  
62  
63  
64  
65

496 **Mammalian two-hybrid experiments confirm the interaction in cellular context.**

497 Mammalian two-hybrid experiments were performed to validate in a cellular context  
498 the cooperativity and the directionality of the interaction between N-CoR<sub>NID</sub> and  
499 RXR/RAR heterodimer, deduced from the measurements of *in vitro* binding constants  
500 and from the SAXS/NMR modelling. Two-hybrid analyses were performed in COS  
501 cells with chimeras containing GAL4 DNA-binding domain fused to a N-CoR  
502 fragment encompassing ID1 and ID2 (from 1629 to 2453 termed Gal-NCoR) or either  
503 CoRNR1 or CoRNR2 of N-CoR (Gal-CoRNR1 and Gal-CoRNR2, respectively), and  
504 the LBD of RXR $\alpha$  or of RAR $\alpha$  fused to the activation domain of VP16 (termed VP16-  
505 RXR or VP16-RAR, respectively).

506 First, we confirmed that wt RXR/RAR heterodimer interact with both  
507 CoRNR1 and CoRNR2 (Fig. 7A), with a slightly better effectiveness for CoRNR1.  
508 However, the interaction of RXR/RAR heterodimer with the longer N-CoR fragment  
509 (equivalent to N-CoR<sub>NID</sub>) is significantly stronger than the individual CoRNR regions.  
510 Therefore, in a cellular environment the two CoRNR motifs in N-CoR bind to the  
511 RXR/RAR heterodimer in a cooperative manner and may induce a stronger affinity.  
512 In addition, the selective RAR agonist TTNPB is able to release CoRNR1 and the N-  
513 CoR fragment from RXR/RAR heterodimer (Fig. 7A). Importantly, a significant  
514 interaction of CoRNR2 is measured even in the presence of TTNPB which only  
515 targets RAR likely reflecting the interaction of RXR with the CoRNR2 motif (Fig.  
516 7A). The directionality of the interaction between N-CoR<sub>NID</sub> and RXR/RAR  
517 heterodimer was further confirmed with two-hybrid experiment with the N-CoR  
518 fragment (Fig. 7B). Whereas RXR alone interacts very weakly with N-CoR, in  
519 agreement with previous observations of our group (Germain et al., 2002) and with  
520 our fluorescence anisotropy data on RXR monomer and CoRNR peptides (Fig. 4),

1  
2  
3  
4  
5  
6  
7  
8  
9  
10  
11  
12  
13  
14  
15  
16  
17  
18  
19  
20  
21  
22  
23  
24  
25  
26  
27  
28  
29  
30  
31  
32  
33  
34  
35  
36  
37  
38  
39  
40  
41  
42  
43  
44  
45  
46  
47  
48  
49  
50  
51  
52  
53  
54  
55  
56  
57  
58  
59  
60  
61  
62  
63  
64  
65

521 addition of RAR $\alpha$  allows to measure a significant interaction between the RXR/RAR  
522 heterodimer and Gal-NCoR. Interestingly, the addition of the RAR-selective agonist  
523 TTNPB was sufficient to decrease this interaction (Fig. 7B). Moreover, RAR alone  
524 can efficiently recruit N-CoR (Fig. 7C). All these observations confirm that RAR is  
525 indispensable for the corepressor recruitment by RXR/RAR heterodimer. On the other  
526 side, the role of RXR for the recruitment of N-CoR was subsequently addressed in a  
527 cellular environment (Fig. 7C). Relative to RAR alone, addition of RXR yielded a  
528 slight but significant increase of the N-CoR interaction confirming an active role of  
529 RXR in the heterodimeric form (Fig. 7C), and thus the cooperativity in the  
530 interaction. This effect was more pronounced for the RXR $\Delta$ H12 deletion mutant (Fig.  
531 7C), in agreement with MST experiments and SAXS modelling. We reasoned that the  
532 RXR H12 deletion may generate a new interaction surface for N-CoR. Contrary to the  
533 wt heterodimer, TTNPB does not reduce N-CoR interaction with RXR $\Delta$ H12/RAR  
534 heterodimer (Fig. 7C). This observation indicates that RXR $\Delta$ H12/RAR retains the  
535 ability to interact with N-CoR, through the RXR hydrophobic groove. Two-hybrid  
536 experiments with RXR $\Delta$ H12/RAR heterodimer and Gal-CoRNR1 and Gal-CoRNR2  
537 clearly demonstrated that CoRNR2 interacts with the more accessible groove of RXR  
538 as TTNPB was unable to reduce CoRNR2 association, and that CoRNR1 interacts  
539 with RAR as its binding is impaired by addition of TTNPB (Fig. 7D), confirming the  
540 directionality in the interaction of N-CoR with RXR $\Delta$ H12/RAR.

541

## 542 **Discussion**

543 In this study we have integrated multiple structural, biophysical and cell-  
544 biology techniques to decipher the molecular bases of transcriptional repression of the  
545 retinoic acid nuclear receptor by the corepressor N-CoR. Our results demonstrate that

1  
2  
3  
4  
5  
6  
7  
8  
9  
10  
11  
12  
13  
14  
15  
16  
17  
18  
19  
20  
21  
22  
23  
24  
25  
26  
27  
28  
29  
30  
31  
32  
33  
34  
35  
36  
37  
38  
39  
40  
41  
42  
43  
44  
45  
46  
47  
48  
49  
50  
51  
52  
53  
54  
55  
56  
57  
58  
59  
60  
61  
62  
63  
64  
65

546 the molecular mechanism relies on the interplay of the flexible elements found in  
547 RXR/RAR heterodimer and the intrinsically disordered N-CoR.

548 We have exploited the high sensitivity of SAXS to probe minute structural  
549 changes that perturb the shape of the RXR/RAR LBDs heterodimer in the absence or  
550 in the presence of various RAR ligands and point mutations. The main structural  
551 changes of the heterodimer reside in the conformation and position of helices H12 of  
552 each monomer. Our analyses demonstrate that helices H12 of RAR and RXR are  
553 better described as disordered in the absence of ligand, in line with previous NMR  
554 and amide hydrogen/deuterium (H/D) exchange experiments for a number of NRs  
555 including RXR (Johnson et al., 2000; Kallenberger et al., 2003; Lu et al., 2006).  
556 These results invalidate the initial hypothesis of allosteric inhibition of RXR by a  
557 subset of nuclear receptors, such as RAR and THR. It was suggested that, in  
558 unliganded RXR/RAR and RXR/THR heterodimers, H12 of RXR docks to the  
559 coregulator-interaction site of the partner (Westin et al., 1998; Zhang et al., 1999).

560 The lack of structural order of RAR helix H12 was also deduced from SAXS  
561 data measured on RXR/RAR heterodimer in the presence of RAR inverse agonist  
562 (BMS493), in agreement with the absence of density for RAR H12 in the crystal  
563 structure of the complex formed by RAR $\alpha$ -LBD, the corepressor N-CoRNR1 and the  
564 inverse agonist (le Maire et al., 2010). These two forms of RXR/RAR heterodimers,  
565 unliganded and in complex with the inverse agonist, bind corepressors, confirming  
566 that the disordered helices H12 are not directly involved in corepressor binding.  
567 Nevertheless, the disordered and highly flexible RXR and RAR helices H12 may  
568 sterically screen the interaction with corepressors. Indeed, RXR $\Delta$ H12 and RAR $\Delta$ H12  
569 deletion mutants recruit corepressors more efficiently than wt RXR and RAR (le  
570 Maire et al., 2010; Zhang et al., 1999), probably due to a higher accessibility of the

1  
2  
3  
4  
5  
6  
7  
8  
9  
10  
11  
12  
13  
14  
15  
16  
17  
18  
19  
20  
21  
22  
23  
24  
25  
26  
27  
28  
29  
30  
31  
32  
33  
34  
35  
36  
37  
38  
571 LBD interaction region for the corepressors. Conversely, addition of RAR agonist  
572 (Am580) induces a compaction of the heterodimer that fits with RAR helix H12  
573 adopting the agonist position, as observed in crystal and solution structures of RAR in  
574 the presence of agonists (Bourguet et al., 2000; Egea et al., 2001; Klaholz et al., 2000;  
575 le Maire et al., 2010). Our SAXS analysis of the mutant RARI396E, for which no  
576 structural data had been reported before, and whose mutation was suggested to induce  
577 the S3 strand to H11 helix transition (le Maire et al., 2010), also provokes a main  
578 rearrangement of RAR helix H12 that is compatible with an agonist conformation.  
579 The transition from a disordered state to an ordered and active conformation of RAR  
580 helix H12 is induced by the binding of an agonist that efficiently triggers corepressor  
581 release. Importantly, this release is dependent of the proportion of agonist  
582 conformation of this helix. With this analysis we confirm that the disorder to order  
583 transition of helix H12 conformation is a key mechanism of corepressor release and  
584 coactivator recruitment by RXR/RAR, contrary to the region corresponding to  
585 H11/S3 in RAR which is the master regulator of corepressor association to RAR (le  
586 Maire et al., 2010).

39  
40  
41  
42  
43  
44  
45  
46  
47  
48  
49  
50  
51  
52  
53  
54  
55  
56  
57  
58  
59  
60  
61  
62  
63  
64  
65  
66  
67  
68  
69  
70  
71  
72  
73  
74  
75  
76  
77  
78  
79  
80  
81  
82  
83  
84  
85  
86  
87  
88  
89  
90  
91  
92  
93  
94  
95  
96  
97  
98  
99  
100  
101  
102  
103  
104  
105  
106  
107  
108  
109  
110  
111  
112  
113  
114  
115  
116  
117  
118  
119  
120  
121  
122  
123  
124  
125  
126  
127  
128  
129  
130  
131  
132  
133  
134  
135  
136  
137  
138  
139  
140  
141  
142  
143  
144  
145  
146  
147  
148  
149  
150  
151  
152  
153  
154  
155  
156  
157  
158  
159  
160  
161  
162  
163  
164  
165  
166  
167  
168  
169  
170  
171  
172  
173  
174  
175  
176  
177  
178  
179  
180  
181  
182  
183  
184  
185  
186  
187  
188  
189  
190  
191  
192  
193  
194  
195  
196  
197  
198  
199  
200  
201  
202  
203  
204  
205  
206  
207  
208  
209  
210  
211  
212  
213  
214  
215  
216  
217  
218  
219  
220  
221  
222  
223  
224  
225  
226  
227  
228  
229  
230  
231  
232  
233  
234  
235  
236  
237  
238  
239  
240  
241  
242  
243  
244  
245  
246  
247  
248  
249  
250  
251  
252  
253  
254  
255  
256  
257  
258  
259  
260  
261  
262  
263  
264  
265  
266  
267  
268  
269  
270  
271  
272  
273  
274  
275  
276  
277  
278  
279  
280  
281  
282  
283  
284  
285  
286  
287  
288  
289  
290  
291  
292  
293  
294  
295  
296  
297  
298  
299  
300  
301  
302  
303  
304  
305  
306  
307  
308  
309  
310  
311  
312  
313  
314  
315  
316  
317  
318  
319  
320  
321  
322  
323  
324  
325  
326  
327  
328  
329  
330  
331  
332  
333  
334  
335  
336  
337  
338  
339  
340  
341  
342  
343  
344  
345  
346  
347  
348  
349  
350  
351  
352  
353  
354  
355  
356  
357  
358  
359  
360  
361  
362  
363  
364  
365  
366  
367  
368  
369  
370  
371  
372  
373  
374  
375  
376  
377  
378  
379  
380  
381  
382  
383  
384  
385  
386  
387  
388  
389  
390  
391  
392  
393  
394  
395  
396  
397  
398  
399  
400  
401  
402  
403  
404  
405  
406  
407  
408  
409  
410  
411  
412  
413  
414  
415  
416  
417  
418  
419  
420  
421  
422  
423  
424  
425  
426  
427  
428  
429  
430  
431  
432  
433  
434  
435  
436  
437  
438  
439  
440  
441  
442  
443  
444  
445  
446  
447  
448  
449  
450  
451  
452  
453  
454  
455  
456  
457  
458  
459  
460  
461  
462  
463  
464  
465  
466  
467  
468  
469  
470  
471  
472  
473  
474  
475  
476  
477  
478  
479  
480  
481  
482  
483  
484  
485  
486  
487  
488  
489  
490  
491  
492  
493  
494  
495  
496  
497  
498  
499  
500  
501  
502  
503  
504  
505  
506  
507  
508  
509  
510  
511  
512  
513  
514  
515  
516  
517  
518  
519  
520  
521  
522  
523  
524  
525  
526  
527  
528  
529  
530  
531  
532  
533  
534  
535  
536  
537  
538  
539  
540  
541  
542  
543  
544  
545  
546  
547  
548  
549  
550  
551  
552  
553  
554  
555  
556  
557  
558  
559  
560  
561  
562  
563  
564  
565  
566  
567  
568  
569  
570  
571  
572  
573  
574  
575  
576  
577  
578  
579  
580  
581  
582  
583  
584  
585  
586  
587  
588  
589  
590  
591  
592  
593  
594  
595  
596  
597  
598  
599  
600  
601  
602  
603  
604  
605  
606  
607  
608  
609  
610  
611  
612  
613  
614  
615  
616  
617  
618  
619  
620  
621  
622  
623  
624  
625  
626  
627  
628  
629  
630  
631  
632  
633  
634  
635  
636  
637  
638  
639  
640  
641  
642  
643  
644  
645  
646  
647  
648  
649  
650  
651  
652  
653  
654  
655  
656  
657  
658  
659  
660  
661  
662  
663  
664  
665  
666  
667  
668  
669  
670  
671  
672  
673  
674  
675  
676  
677  
678  
679  
680  
681  
682  
683  
684  
685  
686  
687  
688  
689  
690  
691  
692  
693  
694  
695  
696  
697  
698  
699  
700  
701  
702  
703  
704  
705  
706  
707  
708  
709  
710  
711  
712  
713  
714  
715  
716  
717  
718  
719  
720  
721  
722  
723  
724  
725  
726  
727  
728  
729  
730  
731  
732  
733  
734  
735  
736  
737  
738  
739  
740  
741  
742  
743  
744  
745  
746  
747  
748  
749  
750  
751  
752  
753  
754  
755  
756  
757  
758  
759  
760  
761  
762  
763  
764  
765  
766  
767  
768  
769  
770  
771  
772  
773  
774  
775  
776  
777  
778  
779  
780  
781  
782  
783  
784  
785  
786  
787  
788  
789  
790  
791  
792  
793  
794  
795  
796  
797  
798  
799  
800  
801  
802  
803  
804  
805  
806  
807  
808  
809  
810  
811  
812  
813  
814  
815  
816  
817  
818  
819  
820  
821  
822  
823  
824  
825  
826  
827  
828  
829  
830  
831  
832  
833  
834  
835  
836  
837  
838  
839  
840  
841  
842  
843  
844  
845  
846  
847  
848  
849  
850  
851  
852  
853  
854  
855  
856  
857  
858  
859  
860  
861  
862  
863  
864  
865  
866  
867  
868  
869  
870  
871  
872  
873  
874  
875  
876  
877  
878  
879  
880  
881  
882  
883  
884  
885  
886  
887  
888  
889  
890  
891  
892  
893  
894  
895  
896  
897  
898  
899  
900  
901  
902  
903  
904  
905  
906  
907  
908  
909  
910  
911  
912  
913  
914  
915  
916  
917  
918  
919  
920  
921  
922  
923  
924  
925  
926  
927  
928  
929  
930  
931  
932  
933  
934  
935  
936  
937  
938  
939  
940  
941  
942  
943  
944  
945  
946  
947  
948  
949  
950  
951  
952  
953  
954  
955  
956  
957  
958  
959  
960  
961  
962  
963  
964  
965  
966  
967  
968  
969  
970  
971  
972  
973  
974  
975  
976  
977  
978  
979  
980  
981  
982  
983  
984  
985  
986  
987  
988  
989  
990  
991  
992  
993  
994  
995  
996  
997  
998  
999  
1000

Our extensive experimental and computational analysis of N-CoR<sub>NID</sub> demonstrates that it is a disordered protein presenting local and long-range structural phenomena that are directly linked to its function. With the exception of the CoRNR1 motif, the N-terminal region presents the prototypical spectroscopic features of a random coil. Moreover, bioinformatics analyses on this region indicate a poor evolutionary conservation and the absence of co-evolutionary interactions with other parts of the protein has often been observed in disordered regions without direct functional roles (Ota and Fukuchi, 2017). Conversely, the C-terminal region including the CoRNR2 motif presents multiple structural features and is evolutionary

1  
2  
3  
4  
5  
6  
7  
8  
9  
10  
11  
12  
13  
14  
15  
16  
17  
18  
19  
20  
21  
22  
23  
24  
25  
26  
27  
28  
29  
30  
31  
32  
33  
34  
35  
36  
37  
38  
39  
40  
41  
42  
43  
44  
45  
46  
47  
48  
49  
50  
51  
52  
53  
54  
55  
56  
57  
58  
59  
60  
61  
62  
63  
64  
65

596 conserved. In solution, CoRNR1 and CoRNR2 are preformed molecular recognition  
597 elements (MOREs) (Mohan et al., 2006) that mediate the interaction with the  
598 heterodimer. The lack of NMR information for these regions is probably due to  
599 intermediate exchange regime processes linked to the transient formation of  
600 secondary structures. Very interestingly, NMR has unveiled a new region, IR, placed  
601 between the two NR interaction domains that is partially ordered and highly  
602 conserved in eukaryotes. These two observations suggest a relevant functional role for  
603 IR. Indeed, N-CoR<sub>NID</sub> experiences transient long-range tertiary interactions between  
604 the IR and ID2 that we have identified and structurally characterized using PREs. The  
605 accurate description of experimental PREs was achieved when the long-range  
606 interaction between co-evolved residues in partially structured regions of the C-  
607 terminal region of N-CoR<sub>NID</sub> was used. This long range contact is partially impaired  
608 when N-CoR interacts with NRs as demonstrated by our NMR analysis of N-CoR<sub>NID</sub>  
609 in complex with the RXR/RAR heterodimer. The formation of the complex would  
610 liberate the IR that would become available to interact with other proteins of the  
611 repressive macromolecular complex.

612 A number of structural and biophysical studies have already revealed the  
613 complex interactions between NR heterodimers and coactivators (Chandra et al.,  
614 2017; Osz et al., 2012; Pavlin et al., 2014; Pogenberg et al., 2005; Rochel et al., 2011;  
615 de Vera et al., 2017; Zheng et al., 2017). However, the interaction of NRs with  
616 corepressors that hampers gene transcription in the basal state are poorly understood.  
617 Our study, which included solution-state structural methods along with biochemical,  
618 biophysical and computational approaches, reveals for the first time the atomistic  
619 details in terms of ensembles of the interaction between RXR/RAR heterodimer and  
620 N-CoR. Our study shows a cooperative interaction of both CoRNR1 and CoRNR2

1  
2  
3  
4  
5  
6  
7  
8  
9  
10  
11  
12  
13  
14  
15  
16  
17  
18  
19  
20  
21  
22  
23  
24  
25  
26  
27  
28  
29  
30  
31  
32  
33  
34  
35  
36  
37  
38  
39  
40  
41  
42  
43  
44  
45  
46  
47  
48  
49  
50  
51  
52  
53  
54  
55  
56  
57  
58  
59  
60  
61  
62  
63  
64  
65

621 motifs with RXR/RAR as the binding affinity of N-CoR<sub>NID</sub> is stronger than the  
622 individual interactions. In addition, the interaction has a defined directionality: N-  
623 CoR<sub>NID</sub> is recruited primarily to RAR through CoRNR1 enabling CoRNR2 to  
624 subsequently bind to RXR for which it has a moderate affinity. Importantly, the other  
625 configuration would not produce a cooperative binding as CoRNR1 does not interact  
626 with RXR.

627         Taken together, our data suggest the mechanistic model that is depicted in  
628 Figure 8. In the absence of ligand, it exists an equilibrium between a major population  
629 of assymmetric binding of N-CoR<sub>NID</sub> to RXR/RAR and a minor population of doubly  
630 bound N-CoR<sub>NID</sub> (deck binding mode) in which both CoRNR boxes simultaneously  
631 interact with the heterodimer, accounting for the cooperativity of the interaction. The  
632 major species of the assymmetric binding mode can be reasonably assigned to N-  
633 CoR<sub>NID</sub> binding to RAR through the CoRNR1 motif, which presents the strongest  
634 local affinity. Our observations through mammalian two hybrid experiments  
635 substantiate with this model, also suggesting that the structural phenomena probed *in*  
636 *vitro* also occurs in cells. The addition of RAR ligands or point mutations in either  
637 RXR and RAR modify the strenght of the individual interactions and, consequently  
638 change the cooperativity and the equilibrium between the assymmetric and the deck  
639 binding modes. Concretely, the addition of a RAR inverse agonist, which strenghtens  
640 the interaction of CoRNR1 with RAR, or the use of a heterodimer with the truncated  
641 RXR H12 (RXR $\Delta$ H12), which increases the interaction of CoRNR2 with RXR,  
642 produce a notable increase of the overall affinity of the complex. This increase is a  
643 consequence of an enhancement of the cooperativity by the equilibrium displacement  
644 towards the deck model as observed in the SAXS and NMR analyses. Conversely,  
645 when weakening RAR binding site using a RAR agonist or the RARI396E mutant,

1  
2  
3  
4  
5  
6  
7  
8  
9  
10  
11  
12  
13  
14  
15  
16  
17  
18  
19  
20  
21  
22  
23  
24  
25  
26  
27  
28  
29  
30  
31  
32  
33  
34  
35  
36  
37  
38  
39  
40  
41  
42  
43  
44  
45  
46  
47  
48  
49  
50  
51  
52  
53  
54  
55  
56  
57  
58  
59  
60  
61  
62  
63  
64  
65

646 there is a decrease in the overall affinity of RXR/RAR for N-CoR<sub>NID</sub>, as a  
647 consequence of the reduction of the population of the deck complex in favour of the  
648 assymmetric binding mode that eventually dissociates. Therefore, the equilibrium  
649 between the two interaction modes has relevant consequences for gene transcription,  
650 the assymmetric mode facilitating coregulator swapping from corepressor to  
651 coactivator. Thus, despite the high overall affinity of the corepressor complex in the  
652 deck binding mode, the low affinity of the individual CoRNR motifs for the LBDs  
653 permits effective coregulator binding versatility upon environmental perturbations.  
654 The multivalency of coregulator proteins has important consequences in the  
655 thermodynamics of the interaction and the kinetics of the transition between repressed  
656 and active states. Multivalency is specially relevant for NR regulation as coactivators  
657 and corepressors have been described to contain several LBD interaction boxes with  
658 slightly different individual affinities. As a consequence, the number of coexisting  
659 assembly states increases dramatically, complexifying the regulation mechanism. In  
660 this context, the integrative approach applied in the present study will offer the  
661 opportunity to disentangle this complexity, structurally characterize the individual  
662 states and address the thermodynamics of NR gene transcription regulation.

663

#### 664 **Acknowledgments**

665 The CBS and the Grenoble Instruct center (ISBG; UMS 3518 CNRS-CEA-UGA-  
666 EMBL) are members of the France-BioImaging (FBI) and the French Infrastructure  
667 for Integrated Structural Biology (FRISBI), supported by the French National  
668 Research Agency (ANR-10-INBS-04-01 and ANR-10-INBS-05, respectively). The  
669 Grenoble Instruct center is also supported by the Grenoble Alliance for Integrated  
670 Structural Cell Biology GRAL (ANR-10-LABX-49-01) within the Grenoble

1  
2  
3  
4  
5  
6  
7  
8  
9  
10  
11  
12  
13  
14  
15  
16  
17  
18  
19  
20  
21  
22  
23  
24  
25  
26  
27  
28  
29  
30  
31  
32  
33  
34  
35  
36  
37  
38  
39  
40  
41  
42  
43  
44  
45  
46  
47  
48  
49  
50  
51  
52  
53  
54  
55  
56  
57  
58  
59  
60  
61  
62  
63  
64  
65

671 Partnership for Structural Biology (PSB). We acknowledge the use of BioSAXS  
672 BM29 beamline at ESRF-Grenoble and the use of NanoTemper equipment of  
673 Laboratory of Spectroscopy and Calorimetry (LEC) at LNBio, CNPEM (Campinas,  
674 Brasil). We acknowledge the financial support from the TGIR-RMN-THC Fr3050  
675 CNRS, the ANR GPCteR (ANR-17-CE11-0022 to NS), the Labex EpiGenMed, an  
676 «Investissements d’avenir» program (ANR-10-LABX-12-01), the CNPq Programa  
677 Ciencia Sem Fronteiras (BJT 300143/2015-0 to ALM), the CNPq Programa Universal  
678 (420416/2016-1 to ALM), from FEDER-COMPETE2020 and FCT (Project LISBOA-  
679 01-0145-FEDER-007660 to TNC) and from the ANR (ANR-14-ACHN-0016 to AB  
680 and RB)..

681

#### 682 **Author contributions**

683 T.C., W.B., P.G., N.S., A.IM. and Pa.B. designed research. T.C., Ph.B., F.A., V.V.,  
684 C.E., P.G., N.S., Al.B. R.B., and A.IM. performed experiments. Ab.B. provided  
685 reagents. T.C., W.B., N.S., A.IM. and Pa.B. analyzed data and wrote the manuscript.

686

687 The authors declare no conflict of interest.

688

#### 689 **Main figure titles and legends**

690 **Figure 1: Modulation of RAR H12 disorder.** (A) Pairwise distance distribution  
691 functions,  $P(r)$ , computed from experimental SAXS curves of wt RXR/RAR  
692 heterodimer (blue), in the presence of the ligands BMS493 (orange) and Am580 (light  
693 green), and for the RXR/RARI396E mutant (dark green). The inset is a heat-map  
694 showing their pairwise Kolmogorov-Smirnov-based similarities (KS). The scale is  
695 relative from low (red) to high (blue) KS values. (B) Ensemble models (5

696 conformations) of RXR/RAR with RXR H12 disordered (residues 441-467) and  
697 either RAR H12 in disordered (left, residues 394-421) or agonistic (right, residues  
698 408-414) conformation. (C) SAXS intensity profiles (gray dots) in logarithmic scale  
699 as a function of the momentum transfer  $s = (4\pi \sin \theta)/\lambda$ , where  $2\theta$  is the scattering  
700 angle, compared with the optimal combination of conformational ensembles for the  
701 RXR/RAR (blue), upon the addition of BMS493 (orange), Am580 (light green), and  
702 for the RXR/RARI396E (dark green). Bottom, point-by-point residuals of the fitting  
703 with the same color code. (D) Evolution of  $\chi^2$  as a function of the relative contribution  
704 of the ensembles corresponding to RXR/RAR with disordered H12 and RAR H12 in  
705 an agonistic conformation. Well-defined minima are observed for all scenarios.

706 **Figure 2: Structural characterization of N-CoR<sub>NID</sub>.** (A) <sup>1</sup>H-<sup>15</sup>N HSQC of N-  
707 CoR<sub>NID</sub> displaying the reduced backbone amide <sup>1</sup>H frequency dispersion typical from  
708 IDPs. (B) Kratky representation of the SAXS profile measured for N-CoR<sub>NID</sub>  
709 indicating its lack of compactness. (C) Far UV Circular Dichroism of N-CoR<sub>NID</sub>. (D)  
710 Charge Hydropathy (Uverky's plot) of N-CoR<sub>NID</sub>. Mean net charge versus mean  
711 hydropathy plot for the set of 275 folded (grey circles) and 91 natively unfolded  
712 proteins (white circles). The N-terminus of N-CoR<sub>NID</sub> (blue) is clearly in the cluster of  
713 disordered proteins, whereas C-terminus of N-CoR<sub>NID</sub> (red) is on the of folded  
714 proteins side. (E) Normalized <sup>1</sup>H-<sup>15</sup>N HSQC's intensities of <sup>15</sup>N -labeled N-CoR<sub>NID</sub>  
715 along the primary sequence. The colored bands represent the CoRNR1 and CoRNR2  
716 motifs in green and pink, respectively. The intermediate region (IR) is colored in grey.  
717 Secondary structure elements of CoRNR boxes are plotted as a red cylinder and blue  
718 arrow for  $\alpha$ -helix and  $\beta$ -strand, respectively. The PSIPRED predicted secondary  
719 structure elements are represented in black and dashed line for coil. (F) Average  
720 disorder prediction (solid grey line) and its standard deviation computed using

1  
2  
3  
4  
5  
6  
7  
8  
9  
10  
11  
12  
13  
14  
15  
16  
17  
18  
19  
20  
21  
22  
23  
24  
25  
26  
27  
28  
29  
30  
31  
32  
33  
34  
35  
36  
37  
38  
39  
40  
41  
42  
43  
44  
45  
46  
47  
48  
49  
50  
51  
52  
53  
54  
55  
56  
57  
58  
59  
60  
61  
62  
63  
64  
65

721 different computational tools along the N-CoR<sub>NID</sub> primary sequence. (G) Sequence  
722 conservation profile computed from a Hidden Markov Model multiple sequence  
723 alignment using Skyalign. The overall height indicates the conservation per position.

724 **Figure 3: Long-Range interactions in NCoR<sub>NID</sub>.** (A) Paramagnetic Relaxation  
725 Enhancement data of N-CoR<sub>NID</sub> measured on WT C2074 (top), S2213C (middle) and  
726 S2288C (bottom) N-CoR<sub>NID</sub> mutants. Experimental values (black bars) calculated  
727 from the ratio of intensity (PRE Ratio =  $I_{para}/I_{dia}$ ) of <sup>1</sup>H-<sup>15</sup>N HSQC spectra measured  
728 on the paramagnetic ( $I_{para}$ ) samples in the position indicated with a yellow star, and on  
729 the diamagnetic samples ( $I_{dia}$ ). Averaged theoretical PRE-ratio profiles computed  
730 from 10,000 N-CoR<sub>NID</sub> structures modelled as fully random coil (solid blue line) or  
731 assuming long-range interactions (solid red line) between predicted co-evolved,  
732 conserved and structured residues within the C-terminal region (LRC). (B)  
733 Experimental SAXS curve of N-CoR<sub>NID</sub> (gray open circles) overlapped with curves  
734 calculated from the random coil pool (blue) and EOM selected sub-ensemble with  
735 long-range contacts (red). The bottom panel shows the point-by-point residuals of the  
736 fitting for both conformational ensembles. (C) Radius of gyration,  $R_g$ , distributions  
737 obtained for the random coil ensemble (blue) and the EOM selected sub-ensemble  
738 (red). (D) Chord-plot of co-evolved residues predicted using BISAnalyser where the  
739 lines connect residues identified as co-evolving pairs. (E)  $\text{Ca-Ca}$  contact map with  
740 respect to a random coil model in logarithmic scale computed from the PRE/SAXS  
741 refined ensemble (top triangle) and from the coarse-grained MD trajectory (bottom  
742 triangle). Color scale quantifies the intensity of the contact where red indicates and  
743 average close contact and yellow indicates an average distance equivalent to the  
744 random coil model. CoRNR1, IR, and CoRNR2 are displayed in the diagonal to  
745 facilitate interpretation of the map.

1  
2  
3  
4  
5  
6  
7  
8  
9  
10  
11  
12  
13  
14  
15  
16  
17  
18  
19  
20  
21  
22  
23  
24  
25  
26  
27  
28  
29  
30  
31  
32  
33  
34  
35  
36  
37  
38  
39  
40  
41  
42  
43  
44  
45  
46  
47  
48  
49  
50  
51  
52  
53  
54  
55  
56  
57  
58  
59  
60  
61  
62  
63  
64  
65

746 **Figure 4: RXR/RAR heterodimer interacts with N-CoR<sub>NID</sub> mainly through RAR.**

747 (A) Affinities of CoRNR motifs of N-CoR for wt RAR, mutant RARI396E and RXR  
748 measured by fluorescence anisotropy, in the absence of ligand or the presence of  
749 Am580 (RAR agonist) or BMS493 (RAR inverse agonist). Data on RAR and  
750 RARI396E were previously published in <sup>23</sup> and are added here for clarity. (B)  
751 Affinities of CoRNR motifs of N-CoR for wt RXR/RAR and mutant RXR/RARI396E  
752 heterodimers measured by fluorescence anisotropy in same ligation states as in A. (C)  
753 Affinities of N-CoR<sub>NID</sub> fragment for wt RXR/RAR (in same ligation states as in A),  
754 mutant RXR/RARI396E and RXR $\Delta$ H12/RAR heterodimers measured by Microscale  
755 Thermophoresis. [Affinity measurements were done by triplicates.](#)

756 **Figure 5: Structural bases of the cooperative binding of N-CoR<sub>NID</sub> with the**

757 **RXR/RAR heterodimer.** (A) Ensemble models of the asymmetric and deck forms of  
758 the N-CoR<sub>NID</sub>:RXR/RAR. Three conformations for each of the ensembles are shown.  
759 (B) Optimization of the relative population of the asymmetric and deck forms of the  
760 N-CoR<sub>NID</sub>:RXR/RAR.  $\chi^2$  values (black dots) for different relative populations of the  
761 two forms of the complex (C) Scattering intensity,  $I(s)$ , as a function of the  
762 momentum transfer,  $s$ , for the SAXS curve measured for N-CoR<sub>NID</sub>:RXR/RAR (grey  
763 empty dots) and the theoretical ones for the deck model (pink line) and the  
764 combination of the asymmetric and deck models (88:12) (blue line). Residuals are  
765 displayed at the bottom of the figure to substantiate the quality of the agreement. (D)  
766 <sup>1</sup>H-<sup>15</sup>N HSQC peak intensity differences for N-CoR<sub>NID</sub> in its free state and in the  
767 presence of an equimolar amount of RXR/RAR. (E) PRE values for S2213C (top) and  
768 S2288C (bottom) N-CoR<sub>NID</sub> mutants (positions of the paramagnetic tags are indicated  
769 with yellow stars) in the presence of the RXR/RAR heterodimer (black bars).  
770 Theoretical PRE values obtained for a structurally biased model of free N-CoR<sub>NID</sub>

1  
2  
3  
4  
5  
6  
7  
8  
9  
10  
11  
12  
13  
14  
15  
16  
17  
18  
19  
20  
21  
22  
23  
24  
25  
26  
27  
28  
29  
30  
31  
32  
33  
34  
35  
36  
37  
38  
39  
40  
41  
42  
43  
44  
45  
46  
47  
48  
49  
50  
51  
52  
53  
54  
55  
56  
57  
58  
59  
60  
61  
62  
63  
64  
65

771 (equivalent to Fig. 3A) are displayed to highlight the differences in the long-range  
772 intramolecular interaction network between the free and bound states of the protein.

773 **Figure 6: Modeling of N-CoR<sub>NID</sub>:RXR/RAR complexes.** (A) Logarithmic  
774 representation of SAXS intensity,  $I$ , versus momentum transfer  $s$  (open circles) of N-  
775 CoR<sub>NID</sub>:RXR/RAR in the presence of inverse agonist BMS493 (orange) or agonist  
776 Am580 (light green), and N-CoR<sub>NID</sub>: RXR $\Delta$ H12/RAR (red) and N-  
777 CoR<sub>NID</sub>:RXR/RARI39E (green) variants. Simulated scattering patterns (solid black  
778 lines) are the best linear combination of theoretical scattering profiles of the species in  
779 panel B weighted by their relative population.  $\chi^2$  values indicate the goodness-of-fit.  
780 The bottom panels show the point-by-point residuals of the fitting for each scenario.  
781 (B) Schematic cartoon representation for all-atom ensembles generated for the  
782 different coexisting species in solution. RXR, RAR and N-CoR<sub>NID</sub> are colored in  
783 orange, green and grey, respectively. ID1 (green) and ID2 (red) NR binding motifs  
784 are represented as boxes in the N-CoR<sub>NID</sub> cartoon. The relative population of the  
785 different species are inside boxes with the same color code as the associated  
786 experimental SAXS. (C) <sup>1</sup>H-<sup>15</sup>N HSQC intensities along N-CoR<sub>NID</sub> in complex with  
787 wt RXR-RAR upon addition of RAR inverse agonist BMS493 (orange), or RAR  
788 agonist Am580 (light green); or in complex with RXR $\Delta$ H12-RAR (red) or  
789 RXR/RARI396E (green). The colored bars represent the CoRNR1 and CoRNR2  
790 motifs in green and pink, respectively.

791 **Figure 7: Interactions of RXR/RAR heterodimers with N-CoR using mammalian**  
792 **two-hybrid assays with (17m)<sub>5x</sub>-G-Luc reporter in COS cells.** (A) Transient  
793 transfections with VP16-RAR and RXR, and with Gal-NCoR or Gal-CoRNR1 or Gal-  
794 CoRNR2. Both CoRNR1 and CoRNR2 are able to interact with the RXR/RAR  
795 heterodimer. (B) Transient transfections with Gal-NCoR and with VP16-RXR alone

1  
2  
3  
4  
5  
6  
7  
8  
9  
10  
11  
12  
13  
14  
15  
16  
17  
18  
19  
20  
21  
22  
23  
24  
25  
26  
27  
28  
29  
30  
31  
32  
33  
34  
35  
36  
37  
38  
39  
40  
41  
42  
43  
44  
45  
46  
47  
48  
49  
50  
51  
52  
53  
54  
55  
56  
57  
58  
59  
60  
61  
62  
63  
64  
65

796 or in combination with RAR. RXR only minimally interacts with N-CoR and RAR is  
797 required for N-CoR-heterodimer complex formation. (C) Transient transfection with  
798 Gal-NCoR and with VP16-RAR alone (dark grey) or in combination with RXR  
799 (white) or RXR $\Delta$ H12 (light gray). (D) Transient transfections with VP16-RAR and  
800 RXR $\Delta$ H12, and with Gal-CoRNR1 or Gal-CoRNR2. N-CoR interacts with the  
801 RXR $\Delta$ H12/RAR heterodimer through an interaction between CoRNR2 and the RXR  
802 groove. In all assays TTNPB, an RAR-selective agonist activating RAR $\alpha$  as  
803 efficiently as Am580, and BMS493 were used at 10nM. [Each transfection was carried](#)  
804 [out in duplicate and repeated three to six times each.](#)

805 **Figure 8: Schematic illustrations summarizing the structural and**  
806 **thermodynamic data presented in this study.** The central part represents the free  
807 partners, RXR/RAR and N-CoR<sub>NID</sub>, and the three forms of the assembly. Size of  
808 arrows connecting these states indicates the thermodynamic preferences observed in  
809 our study. Equilibrium composition can be modified upon addition of ligands or the  
810 presence of mutations on the RXR/RAR heterodimer. These effects are depicted as  
811 gradient colored triangles on the top (affecting the RAR binding) and the right  
812 (affecting the RXR binding) sides of the figure. Asymmetric form bound through the  
813 CoRNR2 and the dissociated RXR/RAR can evolve towards the formation of  
814 complex with a coactivator upon addition of an RAR agonist. This transition from a  
815 repressive to an activated state of the NR is depicted on the right part of the figure.

816

817 **STAR Methods**

818 **Key Resources Table**

819 **Contact for Reagent and Resource Sharing**

1  
2  
3  
4  
5  
6  
7  
8  
9  
10  
11  
12  
13  
14  
15  
16  
17  
18  
19  
20  
21  
22  
23  
24  
25  
26  
27  
28  
29  
30  
31  
32  
33  
34  
35  
36  
37  
38  
39  
40  
41  
42  
43  
44  
45  
46  
47  
48  
49  
50  
51  
52  
53  
54  
55  
56  
57  
58  
59  
60  
61  
62  
63  
64  
65

820 Further information and requests for resources and reagents should be directed to  
821 and will be fulfilled by the Lead Contact, Pau Bernado (pau.bernado@cbs.cnrs.fr).

## 822 **Method Details**

### 823 **Ligands and peptides**

824 The ligands Am580, BMS493 and TTNPB were purchased from Tocris Bioscience.  
825 The fluorescent peptides CoRNR1 (fluorescein-RLITLADHICQITQDFAR) and  
826 CoRNR2 (fluorescein-DPASNLGLEDIIRKALMGSGFD) from N-CoR were  
827 purchased from EZbiolab.

### 828 **Constructs, expression and purification of proteins and complexes**

829 The heterodimer RXR/RAR (mRXR $\alpha$ /hRAR $\alpha$ , Uniprot codes P28700 and P10276,  
830 respectively) was prepared as previously described in (Pogenberg et al., 2005). The  
831 heterodimer RXR $\Delta$ H12/RAR (mRXR $\alpha$  $\Delta$ H12/hRAR $\alpha$ ) comprises a shorter form of  
832 RXR in which the region N227 to D444 including helix H12 is deleted. The  
833 heterodimer RXR/RARI396E (mRXR $\alpha$ /hRAR $\alpha$ I396E) comprises the I396E mutation  
834 of RAR $\alpha$  (Le Maire et al., 2010). The N-CoR<sub>NID</sub> protein corresponds to the sequence  
835 from Gln2059 to Glu2325 of mouse N-CoR (Uniprot code Q60974) and was prepared  
836 as described in (Harrus et al., 2018). For the preparation of the complexes, the  
837 purified heterodimers (RXR/RAR or RXR $\Delta$ H12/RAR) were mixed with a two-fold  
838 molar excess of purified N-CoR<sub>NID</sub> fragment and incubated overnight at 4°C. Then,  
839 the mix was loaded on a S200 superdex gel filtration column in a buffer consisting in  
840 50mM Tris HCl pH7.5, 150mM NaCl, 2mM DTT and fractions corresponding to the  
841 ternary complexes were pooled. The purity of the complexes was checked on a SDS-  
842 page gel.

### 843 **Analytical ultracentrifugation sedimentation velocity experiments (AUC-SV)**

1  
2  
3  
4  
5  
6  
7  
8  
9  
10  
11  
12  
13  
14  
15  
16  
17  
18  
19  
20  
21  
22  
23  
24  
25  
26  
27  
28  
29  
30  
31  
32  
33  
34  
35  
36  
37  
38  
39  
40  
41  
42  
43  
44  
45  
46  
47  
48  
49  
50  
51  
52  
53  
54  
55  
56  
57  
58  
59  
60  
61  
62  
63  
64  
65

844 Samples of N-CoR<sub>NID</sub>, RXR/RAR, N-CoR<sub>NID</sub>:RXR/RAR, N-CoR<sub>NID</sub>:RXR/RAR in  
845 the presence of BMS493, and N-CoR<sub>NID</sub>:RXRΔH12/RAR at about 1 g/L in 50 mM  
846 Tris pH 7.4, 150 mM NaCl, 2 mM DTT, were investigated in SV experiments. SV  
847 experiments were conducted in an XLI analytical ultracentrifuge (Beckman, Palo  
848 Alto, CA) using an ANTi-50 rotor and detection at 280 and 295 nm, at 42 000 revs.  
849 per minutes (rpm) (130 000g) and 12°C overnight, using double channel center pieces  
850 (Nanolytics, Germany) of 12 mm optical path length (loaded volume: 400μL, the  
851 reference channel being filled with the solvent) equipped with sapphire windows. For  
852 each sample, because the total absorbance at 280 nm exceeded 1.2, the set of SV  
853 profiles obtained at 295 nm was analyzed, using analysis in terms of a continuous  
854 distribution,  $c(s)$ , of sedimentation coefficients,  $s$ , and of one non interacting species,  
855 providing independent estimated of  $s$  and the molar mass,  $M$ , of the Sedfit software  
856 (Schuck, 2000), version 14.1 (freely available at:  
857 <http://www.analyticalultracentrifugation.com>). The related figures were made with  
858 the program Gussi (Brautigam et al., 2016) (freely available at:  
859 <http://biophysics.swmed.edu/MBR/software.html>). The values of  $s$  were corrected for  
860 experimental conditions (12°C, solvent density,  $\rho^\circ = 1.007$  g/mL, and viscosity,  $\eta^\circ$   
861  $= 1.235$  g/mL, estimated using the program Sednterp (freely available at:  
862 <http://sednterp.unh.edu/>) to values,  $s_{20w}$ , at 20°C in pure water ( $\rho^\circ = 0.99823$  g/mL,  
863 and viscosity,  $\eta^\circ = 1.002$  g/mL), and interpreted, through the Svedberg equation  $s = M$   
864  $(1 - \rho^\circ \bar{v}) / (N_A 6\pi \eta^\circ R_H)$ , where  $M$  is the molecular mass,  $\bar{v}$  is the partial specific  
865 volume (0.720 mL/g for N-CoR<sub>NID</sub>, 0.743 mL/g for RXR/RAR complexes, 0.735  
866 mL/g for N-CoR<sub>NID</sub>:RXR/RAR complexes, calculated using the program Sedfit), and  
867  $N_A$  is Avogadro's number.  $R_H$  is the hydrodynamic radius.  $R_H = f/f_{\min} R_{\min}$ , with  $f/f_{\min}$   
868 the frictional ratio and  $R_{\min}$  the radius of the anhydrous volume. The  $s_{20w}$ -values were

1  
2  
3  
4  
5  
6  
7  
8  
9  
10  
11  
12  
13  
14  
15  
16  
17  
18  
19  
20  
21  
22  
23  
24  
25  
26  
27  
28  
29  
30  
31  
32  
33  
34  
35  
36  
37  
38  
39  
40  
41  
42  
43  
44  
45  
46  
47  
48  
49  
50  
51  
52  
53  
54  
55  
56  
57  
58  
59  
60  
61  
62  
63  
64  
65

869 analyzed in term of  $f/f_{\min}$  considering the the molar masses calculated from different  
870 association states. Stoichiometries with  $f/f_{\min}$  in the range 1.25 to 1.5 were considered  
871 as acceptable, since corresponding to globular compact to reasonably  
872 anisotropic/elongated or extended shapes. The results of the non-interacting species  
873 analysis provided molar masses about 20% lower than the derived stoichiometry,  
874 which can reasonably be related to the low signal/noise level of the data.

#### 875 **Mass spectrometry (RPLC-UV/MS)**

876 Relative abundance of RAR, RXR and N-CoR<sub>NID</sub> in purified complex was assessed  
877 using reverse phase liquid chromatography (Waters Alliance 2695) coupled to UV  
878 (diode array detector) and MS (Waters LCT operated in the positive ion mode)  
879 detection. Protein sample was diluted in buffer A (0.1% TFA / 0.1% FA /water)  
880 before 600 pmol of complex were injected onto reverse phase Xbridge BEH300 C4  
881 column (3.5 $\mu$ m; 50  $\times$  2.1mm; T 65°C; flow rate 0.2 ml/min). Eluting gradient was  
882 ramped from 2 to 90% buffer B (0.08% TFA / 0.1% FA / 70% ACN / 30% IprOH) in  
883 40 min. Eluting species were detected by UV and mass spectrometry. Relative  
884 abundance of RAR, RXR and N-CoR<sub>NID</sub> was calculated from protein theoretical  
885 extinction coefficient and UV peak area ( $\lambda = 280$  nm) according to equation:  
886  $Abs_{280\text{ nm}}(P) = \epsilon_{280\text{ nm}}(P) \times L \times [P]$  where “Abs” and “ $\epsilon$ ” correspond to protein  
887 (P) absorbance and extension coefficient ( $M^{-1} \text{ cm}^{-1}$ ), respectively, at 280 nm. “L” is  
888 the light path length (cm) and [P] corresponds to protein concentration (M).

#### 889 **Steady-state fluorescence anisotropy**

890 We performed assays using a Safire microplate reader (TECAN) with the excitation  
891 wavelength set at 470 nm and emission measured at 530 nm for fluorescein-tagged  
892 peptides. The buffer solution for assays was 20 mM Tris-HCl, pH 7.5, 150 mM NaCl,  
893 1 mM EDTA, 5 mM DTT and 10% (v/v) glycerol. We initiated the measurements at

1  
2  
3  
4  
5  
6  
7  
8  
9  
10  
11  
12  
13  
14  
15  
16  
17  
18  
19  
20  
21  
22  
23  
24  
25  
26  
27  
28  
29  
30  
31  
32  
33  
34  
35  
36  
37  
38  
39  
40  
41  
42  
43  
44  
45  
46  
47  
48  
49  
50  
51  
52  
53  
54  
55  
56  
57  
58  
59  
60  
61  
62  
63  
64  
65

894 the highest concentration of protein (20  $\mu$ M) and diluted the protein sample  
895 successively two-fold with the buffer solution. For each point of the titration curve,  
896 we mixed the protein sample with 4 nM of fluorescent peptide and 40  $\mu$ M of ligand  
897 (two molar equivalents). We fitted binding data using a sigmoidal dose-response  
898 model (GraphPad Prism, GraphPad Software). The reported data are the average of at  
899 least three independent experiments.

#### 900 **MicroScale Thermophoresis (MST)**

901 A fluorescent probe (Atto647N maleimide, Sigma) was attached to the thiol group of  
902 the sole cysteine of the N-CoR<sub>NID</sub> fragment, according to the manufacturer's  
903 instructions. This cysteine (Cys 2074) is in the CoRNR1 motif but is not involved in  
904 the interaction between RAR and N-CoR as it points to the outside in the crystal  
905 structure of the complex (Le Maire et al., 2010). Heterodimers (RXR/RAR,  
906 RXR $\Delta$ H12/RAR and RXR/RARI396E) were prepared as a twofold serial dilution in  
907 MST buffer (NanoTemper Technologies GmbH) and added to an equal volume of 80  
908 nM labelled N-CoR<sub>NID</sub>, in MST buffer. After 10 min incubation time, the complex  
909 was filled into Monolith NT.115 Premium Coated Capillaries (NanoTemper  
910 Technologies GmbH) and thermophoresis was measured using a Monolith NT.115  
911 Microscale Thermophoresis device (NanoTemper Technologies GmbH) at an ambient  
912 temperature of 22°C, with 5 s/30 s/ 5 s laser off/on/off times, respectively. Instrument  
913 parameters were adjusted with 40% red LED power and 20% IR-laser power. Data  
914 from three independent measurements were analyzed (NT Analysis software last  
915 version, NanoTemper Technologies GmbH) using the signal from Thermophoresis +  
916 T-Jump.

#### 917 **Structural bioinformatics on N-CoR<sub>NID</sub>**

1  
2  
3  
4  
5  
6  
7  
8  
9  
10  
11  
12  
13  
14  
15  
16  
17  
18  
19  
20  
21  
22  
23  
24  
25  
26  
27  
28  
29  
30  
31  
32  
33  
34  
35  
36  
37  
38  
39  
40  
41  
42  
43  
44  
45  
46  
47  
48  
49  
50  
51  
52  
53  
54  
55  
56  
57  
58  
59  
60  
61  
62  
63  
64  
65

918 Local secondary structural features of N-CoR<sub>NID</sub> were predicted using the support  
919 vector machine-based PSIPRED3.2 server (Buchan et al., 2013). Disorder propensity  
920 of N-CoR<sub>NID</sub> was assessed with IUPRED (Dosztányi et al., 2005), PrDOS (Ishida and  
921 Kinoshita, 2007), PONDR-FIT (Xue et al., 2010) and DISOPRED3 (Jones and  
922 Cozzetto, 2015). The GREMLIN software (Kamisetty et al., 2013) was fed with the  
923 N-CoR<sub>NID</sub> sequence to capture evolutionary conserved sequences by searching a pre-  
924 clustered Uniprot database using the HHblits algorithm (Remmert et al., 2012). A  
925 Hidden Markov Model (HMM) multiple sequence alignment (MSA) was generated  
926 excluding hits with  $\geq 75$  % gaps. A final set of 61 sequences was used for detecting  
927 conservation and co-evolution signatures at residue-level. Conservation profile was  
928 extracted from the HMM MSA using Skylign to compute the probability of observing  
929 for a given position a specific residue above the background (Wheeler et al., 2014).  
930 Co-evolution analysis within the MSA was performed using BIS2 (Oteri et al., 2017),  
931 which bypass the statistics requirements to estimate the background noise and the  
932 relevance of the co-evolution signal. BIS2 is a combinatorial method that allows  
933 identifying co-evolving blocks, instead of only residues, in a small number of  
934 homologous sequences.

### 935 **Small-angle X-ray scattering**

936 Small-angle X-ray scattering data were measured at the BM29 beam-line from the  
937 ESRF (Grenoble, France) using the X-ray wavelength of 0.99Å and a sample-to-  
938 detector distance of ~2.9 m (Pernot et al., 2013). Several datasets were collected at  
939 multiple concentrations (Table S1 and S3) in 50mM Tris HCl pH7.5, 150mM NaCl,  
940 2mM TCEP. Prior to data collection, the isolated proteins and the ternary complexes  
941 were supplemented with 2mM TCEP and concentrated. When necessary, ligands  
942 (BMS493 and Am580) were added to the complex in a three molar excess before

1  
2  
3  
4  
5  
6  
7  
8  
9  
10  
11  
12  
13  
14  
15  
16  
17  
18  
19  
20  
21  
22  
23  
24  
25  
26  
27  
28  
29  
30  
31  
32  
33  
34  
35  
36  
37  
38  
39  
40  
41  
42  
43  
44  
45  
46  
47  
48  
49  
50  
51  
52  
53  
54  
55  
56  
57  
58  
59  
60  
61  
62  
63  
64  
65

943 concentration. Repetitive measurements allowed to detect and to correct for radiation  
944 damage and scattering patterns of the buffer solutions were recorded before and after  
945 the measurements of each protein sample. Final curves for each concentration were  
946 derived after subtracting the averaged buffer scattering from the protein sample  
947 patterns using PRIMUS. SAXS curves of different concentrations were merged to  
948 avoid interparticle interactions using standard protocols with ATSAS software  
949 (Franke et al., 2017).

950 The  $R_g$  values in Table S1 and Table S3 were estimated by applying the Guinier  
951 approximation in the range  $s < 1.3/R_g$  for globular proteins and  $s < 0.8/R_g$  for free N-  
952 CoR<sub>NID</sub>. Pair-wise distance distribution functions,  $P(r)$ , were obtained by indirect  
953 Fourier Transform of the scattering intensities with GNOM (Svergun et al., 1988). We  
954 used CRY SOL (Svergun et al., 1995) to compute the theoretical SAXS profiles from  
955 conformational ensembles of free N-CoR<sub>NID</sub>, RXR/RAR, and N-CoR<sub>NID</sub>:RXR/RAR  
956 complexes. All theoretical curves were obtained with 101 points, and a maximum  
957 scattering vector of  $0.5 \text{ \AA}^{-1}$  using 25 harmonics. The resulting ensemble-based  
958 CRY SOL SAXS curves, or their weighted combination, were directly compared to  
959 the corresponding experimental SAXS data with OLIGOMER (Konarev et al., 2003).

#### 960 **Nuclear Magnetic Resonance (NMR)**

961 NMR data were recorded using  $140 \mu\text{M}$  U- $^{15}\text{N}$  N-CoR<sub>NID</sub> and  $600 \mu\text{M}$  U- $^{13}\text{C}/^{15}\text{N}$   
962 N-CoR<sub>NID</sub> labeled protein in 50mM Bis Tris buffer at pH 6.7, 150mM NaCl, 1mM  
963 EDTA and 2mM TCEP with 7% (v/v)  $^2\text{H}_2\text{O}$ . NMR assignment experiments were  
964 recorded at 293 K on a 950 MHz Bruker Avance III spectrometer equipped with a  
965 cryogenic triple-resonance probe (IR-RMN Gif/Yvette).  $^1\text{H}$  chemical shifts were  
966 referenced directly, and  $^{15}\text{N}$  chemical shifts indirectly (Markley et al., 1998), to added  
967 2,2-dimethyl-2- silapentane-5-sulfonate (DSS, methyl  $^1\text{H}$  signal at 0.00 ppm). A set of

1  
2  
3  
4  
5  
6  
7  
8  
9  
10  
11  
12  
13  
14  
15  
16  
17  
18  
19  
20  
21  
22  
23  
24  
25  
26  
27  
28  
29  
30  
31  
32  
33  
34  
35  
36  
37  
38  
39  
40  
968 3D Best-TROSY HNCO, HN(CA)CO, HN(CO)CA, HNCA, iHNCA,  
969 HN(CO)CACB, HNCACB, iHNCACB (Lescop et al., 2007), and H-N-N experiments  
970 HN(CA)NH, HN(COCA)NH. NMR interaction and PRE experiments (Barrett et al.,  
971 2013) were recorded at 293 K on a 700 MHz Bruker Avance III spectrometer  
972 equipped with a cryogenic triple-resonance probe. Spectra were processed with  
973 nmrpipe and analyzed using nmrview (Johnson and Blevins, 1994). NMR  $^1\text{H}$ - $^{15}\text{N}$   
974 HSQC's have been recorded for  $^{15}\text{N}$  labelled N-CoR<sub>NID</sub>, and for  $^{15}\text{N}$ -N-  
975 CoR<sub>NID</sub>:RXR/RAR (1:1),  $^{15}\text{N}$ -N-CoR<sub>NID</sub>:RXR $\Delta$ H12/RAR (1:1),  $^{15}\text{N}$ -N-CoR<sub>NID</sub>:  
976 RXR/RARI396E (1:1.2).  $^1\text{H}$ - $^{15}\text{N}$  HSQCs were also measured for equimolar  
977 complexes of  $^{15}\text{N}$ -N-CoR<sub>NID</sub>:RXR/RAR in the presence of 1.2 molar excess of RAR  
978 agonist (Am580) or RAR inverse agonist (BMS493). For PRE measurements,  $^1\text{H}$ - $^{15}\text{N}$   
979 HSQC spectra of diamagnetic and paramagnetic samples of  $^{15}\text{N}$ -N-CoR<sub>NID</sub>:RXR/RAR  
980 (1:1.3) were acquired with a recycling delay between scans of 2 s to ensure that  
981 magnetization recovery level is identical for both states and using the same  
982 concentration and number of scans for both samples. The paramagnetic contribution  
983 to the relaxation rate was determined as the ratio of peak intensities in the  
984 paramagnetic and diamagnetic states.

#### 41 **Site-directed spin-labeling for paramagnetic studies**

42  
43  
44  
45  
46  
47  
48  
49  
50  
51  
52  
53  
54  
55  
56  
57  
58  
59  
60  
61  
62  
63  
64  
65  
986 In addition to the wt cysteine residue C2074, two additional single-cysteine variants  
987 of N-CoR<sub>NID</sub> (S2213C and S2288C) were engineered by site-directed mutagenesis  
988 after substitution of the native cysteine by a serine (C2074S), using QuikChange  
989 Lightning Site-Directed mutagenesis kit. All constructs were verified by DNA  
990 sequencing. In order to conjugate the paramagnetic tag, a 10-fold excess of 3-(2-  
991 Iodoacetamido)-2,2,5,5-tetramethyl-1-pyrrolidinyloxy (IA-PROXYL) spin label was  
992 immediately added to reducing agent-free samples, just after elution from PD-10

1  
2  
3  
4  
5  
6  
7  
8  
9  
10  
11  
12  
13  
14  
15  
16  
17  
18  
19  
20  
21  
22  
23  
24  
25  
26  
27  
28  
29  
30  
31  
32  
33  
34  
35  
36  
37  
38  
39  
40  
41  
42  
43  
44  
45  
46  
47  
48  
49  
50  
51  
52  
53  
54  
55  
56  
57  
58  
59  
60  
61  
62  
63  
64  
65

993 desalting columns, and left reacting for 3 h in the dark at room temperature. Excess of  
994 unreacted tag was removed by passing the reaction mixture twice through a PD-10  
995 column, and exchanged to 50mM Bis Tris buffer at pH 6.7, 150mM NaCl, 1mM  
996 EDTA. Reference diamagnetic samples were obtained after adding 5-fold of fresh  
997 ascorbic acid to the same sample used to acquire the paramagnetic spectra.

### 998 **Structural modeling of RXR/RAR heterodimer**

999 Multiple structural all-atoms models of the RXR/RAR were built in order to describe  
1000 SAXS curves of the heterodimer in different experimental conditions. The fully  
1001 disordered H12 scenario was built using the 1DKF structure as a template and by  
1002 adding the disordered N- and C-termini (including the H12) extensions as well as the  
1003 connecting linker between helices H1 and H3. Previous crystallographic structures  
1004 were used to model the other scenarios where one (RAR) or both (RAR and RXR)  
1005 H12 regions were placed folded and bound to the rest of the LDB in either an agonist  
1006 or antagonist conformation. Concretely, the structure 1DKF (Bourguet et al., 2000)  
1007 was used as a template for the antagonist conformation, and the structures 1XDK  
1008 (Pogenberg et al., 2005) and 3KMR (Le Maire et al., 2010) were used as templates for  
1009 the agonist conformation (Fig. S1 and Table S2). Ensembles of disordered fragments  
1010 were built using *Flexible-Meccano* (FM) (Bernado et al., 2005; Ozenne et al., 2012)  
1011 and attached to the X-ray templates using *in-house* scripts (Cordeiro et al., 2017b).  
1012 Briefly, for each disordered segment built, side-chains were added using SCCOMP  
1013 (Eyal et al., 2004) and then pre-processed with Rosetta 3.5 *fixbb* module (Kuhlman et  
1014 al., 2003) to alleviate steric clashes. Each structure was then refined in explicitly  
1015 solvent using Gromacs 5.0.2 (Hess et al., 2008). All ensembles of RXR/RAR  
1016 heterodimer comprised 5,000 conformers.

### 1017 **Structural ensembles of free N-CoR<sub>NID</sub>**

1018 A random coil ensemble model of N-CoR<sub>NID</sub> containing 10,000 conformations was  
1019 calculated also employing FM (Bernado et al., 2005; Ozenne et al., 2012) followed by  
1020 side-chains modelling and refinement as described above. A second structurally  
1021 biased ensemble derived from the evolutionary conservation and a co-evolutionary  
1022 analysis was computed in the following way. A starting random coil ensemble of  
1023 200,000 conformations of N-CoR<sub>NID</sub> was filtered selecting those structures presenting  
1024 at least two contacts ( $\leq 15$  Å) between residues in distal blocks of conserved (with  
1025 Bits  $\geq 1.6$ ), structured (average disorder propensity below 0.5), and/or co-evolving  
1026 residues (Fig. 2 and Fig. 3) within the C-terminal region. The filtered conformations  
1027 ( $\approx 35,000$ ) resulted in a compact ensemble that did not describe the SAXS data. We  
1028 further refined it by performing 200 independent Ensemble Optimization Method  
1029 (EOM) runs (Bernado et al., 2007), and those conformations that were not selected in  
1030 any of them were discarded. The SAXS-refined ensembles was more extended than  
1031 that obtained by distance restraints. The final ensemble of 10,000 conformations was  
1032 use to interpret the PRE data. Briefly, for each conformer, the theoretical  
1033 intramolecular  $^1\text{H}$ - $^{15}\text{N}$ -PRE-rates were computed using the Solomon-Bloembergen  
1034 approximation (Iwahara et al., 2004; Salmon et al., 2010). Dynamics of the  
1035 paramagnetic PROXYL moiety was accounted for by using multiple conformational  
1036 states derived from a 100 ns Molecular Dynamics (MD) simulation of a Gly-Gly-Cys-  
1037 Gly-Gly peptide in water at 298K, where the PROXYL moiety was attached to the  
1038 central cysteine residue (Beck et al., 2008; Polyhach et al., 2011). From this library,  
1039 the native and engineered single-cysteine residues were *in-silico* labelled with  
1040 multiple sterically allowed spin-label dispositions. This ensemble representation  
1041 enabled the estimation of the order parameters that account for the motion of the  
1042 dipolar proton-electron interaction vector (Iwahara et al., 2004; Salmon et al., 2010).

1043 The correlation time of N-CoR<sub>NID</sub> was estimated to be 5.79 ns using HYCUD (Parigi  
1044 et al., 2014). With this strategy, the PRE-rates for C2074, S2213C and S2288C were  
1045 independently calculated for each N-CoR<sub>NID</sub> conformer, averaged over the complete  
1046 ensembles of the three N-CoR<sub>NID</sub> forms, and compared with the experimental ones  
1047 without any optimization process (Salmon et al., 2010).

### 1048 **Molecular Dynamics Simulation**

1049 Simulations were based on the one-bead-per-residue coarse-grained model proposed  
1050 by (Smith et al., 2014) for intrinsically disordered proteins. N-CoR<sub>NID</sub> fragments with  
1051 high  $\alpha$ -helix propensity (2065-2088, 2214-2234, 2269-2291) were restrained to  
1052 helical conformation *via* an elastic network with a force constant of 500 kJ.mol<sup>-1</sup>.nm<sup>-2</sup>  
1053 whereas the original bonded potential for disordered chains was used for the  
1054 remaining regions. Electrostatic interactions between charged residues were  
1055 represented with a Debye Huckel energy functions ( $\lambda = 0.9$  nm and  $\epsilon_{ES} = 1.485$ ).  
1056 Excluded volume and attractive hydrophobic interactions were modeled combining a  
1057 purely repulsive Weeks-Chandler-Andersen (WCA) potential with the attractive part  
1058 of a Lennard Jones potential ( $\sigma = 0.58$  nm). The parameter  $\alpha_{CG}$ , which determines  
1059 the strength of the hydrophobic interactions, was specifically tuned for N-CoR<sub>NID</sub>  
1060 system by minimizing the  $\chi^2$  between experimental and simulated SAXS curves. The  
1061 latter were calculated from coarse-grained trajectories using CRY SOL (Svergun et al.,  
1062 1995) upon reconstruction of the full atomistic structure via BBQ (Gront et al., 2007)  
1063 and SCWRL4 (Krivov et al., 2009). Notably, this procedure revealed that an optimal  
1064 agreement with SAXS data ( $\chi^2 = 0.87$ ) was obtained for  $\alpha_{CG} = 0.5$ , which is  
1065 remarkably similar to the result obtained in the original publication for a set of diverse  
1066 disordered proteins by comparison with FRET data. All simulations were performed  
1067 with the GROMACS 5.4 molecular dynamics package (Abraham et al., 2015). An

1068 extended configuration was generated and used as initial structure for the simulation  
1069 inside a  $78733 \text{ nm}^3$  cubic box with periodic boundary conditions. The equations of  
1070 motion were integrated every 20 fs during stochastic dynamics with a damping  
1071 coefficient set to  $25 \text{ amu.ps}^{-1}$ . A plain cutoff of 5.0 nm was used for both Lennard-  
1072 Jones and electrostatic interactions. All of the simulations were performed in the NVT  
1073 ensemble and the temperature was kept constant to a reference value of 300 K. During  
1074 the production, five replicas of 1  $\mu\text{s}$  each were run for a total simulation length of 5  
1075  $\mu\text{s}$ .

### 1076 **Structural Modelling of N-CoR<sub>NID</sub>:RXR/RAR complexes**

1077 The structure of full-length N-CoR<sub>NID</sub> bound to RXR/RAR was modeled exploiting  
1078 the existing crystal structure of the RAR/NCOR CoRNR1 complex (3KMZ) (Le Maire  
1079 et al., 2010) and that of the RXR in complex with SMRT CoRNR2 complex (3R29)  
1080 (Zhang et al., 1999), which has a 75% of sequence identity with NCOR CoRNR2.  
1081 Using S-CoRNR2 as a template we created a homology model for bound CoRNR2. In  
1082 the complexes, the conformations of bound CoRNR1 and/or CoRNR2 were  
1083 maintained as in the crystal structures. For singly bound complexes (asymmetric),  
1084 with N-CoR<sub>NID</sub> bound to RAR or RXR through CoRNR1 or CoRNR2 respectively,  
1085 disordered statistical coil N- and C-terminal extensions were built onto the structured  
1086 peptide employing the above-described work-flow to model ensembles of flexible  
1087 fragments (Cordeiro et al., 2017a). The doubly bound complex was created in two  
1088 steps. Firstly, we use FM to generate a structural ensemble of 100,000 singly bound  
1089 complexes with N-CoR<sub>NID</sub> bound to RXR/RAR through CoRNR1, but with CoRNR2  
1090 structured as in the crystal. Secondly, this starting ensemble was refined by selecting  
1091 those conformers with CoRNR2 in the vicinity of RXR binding site (i.e.  $\leq 6.5$ ),  
1092 followed by a docking process driven by the surface contacts observed in the

1  
2  
3  
4  
5  
6  
7  
8  
9  
10  
11  
12  
13  
14  
15  
16  
17  
18  
19  
20  
21  
22  
23  
24  
25  
26  
27  
28  
29  
30  
31  
32  
33  
34  
35  
36  
37  
38  
39  
40  
41  
42  
43  
44  
45  
46  
47  
48  
49  
50  
51  
52  
53  
54  
55  
56  
57  
58  
59  
60  
61  
62  
63  
64  
65

1093 RXR/SMRT CoRNR2 complex (PDB:3R29), which were integrated as distance  
1094 restraints in the HADDOCK docking approach (Dominguez et al., 2003). Structures  
1095 were then ranked using the energy-based HADDOCK scoring function and a term  
1096 quantifying the RMSD of the binding interface with the RXR/SMRT CoRNR2  
1097 complex. In the apo-form and in the presence of BMS493, RAR/RXR was modelled  
1098 with disordered H12s. For RAR/RXRI396E mutant and in the presence of Am580,  
1099 RAR H12 was placed in the agonist position, and RXR H12 was removed in the  
1100 complex between N-COR<sub>NID</sub> and RXR $\Delta$ H12/RAR. All ensembles of N-  
1101 CoR<sub>NID</sub>:RXR/RAR complexes contained 2,000 conformers.

## 1102 **Two-hybrid experiments**

1103 COS cells derived from African green monkey kidney (ATCC) were cultured in  
1104 DMEM with Glutamax and 5% (v/v) FCS and transfected using JetPei transfectant  
1105 (Ozyme). After 24 h, the medium was changed to a medium containing the indicated  
1106 ligands or vehicle. Cells were lysed and assayed for reporter expression 48 h after  
1107 transfection. The luciferase assay system was used according to the manufacturer's  
1108 instruction (Promega). In each case, results were normalized to coexpressed  $\beta$ -  
1109 galactosidase. Each transfection was carried out in duplicate and repeated three to six  
1110 times each.

1111 **Data availability.** The NMR chemical shifts of N-CoR<sub>NID</sub> have been deposited at the  
1112 BMRB databank under the entry 27848. The SAXS data have been deposited at the  
1113 SASBDB under the project "Nuclear receptor CoRepressor (N-CoR) and retinoic acid  
1114 receptor heterodimer(RXR/RAR) Complex". The accession codes are SASDF34,  
1115 SASDF44, SASDF54, SASDF64, SASDF74 and SASDF84 for Free Nuclear receptor  
1116 CoRepressor NID, RXR/RAR Heterodimer:N-CoR<sub>NID</sub> Complex, RXR $\Delta$ H12/RAR  
1117 Heterodimer:N-CoR<sub>NID</sub> Complex, RXR/RAR Heterodimer:N-CoR<sub>NID</sub> Complex

1118 with RAR inverse agonist (BMS493), RXR/RARI396E Heterodimer:N-CoRNID  
1119 Complex and RXR/RAR Heterodimer:N-CoRNID Complex with RAR agonist  
1120 (Am580), respectively.

## 1121 **References**

- 1122 Abraham, M.J., Murtola, T., Schulz, R., Páll, S., Smith, J.C., Hess, B., and Lindah, E.  
1123 (2015). Gromacs: High performance molecular simulations through multi-level  
1124 parallelism from laptops to supercomputers. *SoftwareX* 1–2, 19–25.
- 1125 Barrett, P.J., Chen, J., Cho, M.-K., Kim, J.-H., Lu, Z., Mathew, S., Peng, D., Song,  
1126 Y., Van Horn, W.D., Zhuang, T., et al. (2013). The quiet renaissance of protein  
1127 nuclear magnetic resonance. *Biochemistry* 52, 1303–1320.
- 1128 Beck, D.A.C., Alonso, D.O.V., Inoyama, D., and Daggett, V. (2008). The intrinsic  
1129 conformational propensities of the 20 naturally occurring amino acids and reflection  
1130 of these propensities in proteins. *Proc. Natl. Acad. Sci.* 105, 12259–12264.
- 1131 Bernado, P., Blanchard, L., Timmins, P., Marion, D., Ruigrok, R.W., and Blackledge,  
1132 M. (2005). A structural model for unfolded proteins from residual dipolar couplings  
1133 and small-angle x-ray scattering. *Proc. Natl. Acad. Sci. U S A* 102, 17002–17007.
- 1134 Bernado, P., Mylonas, E., Petoukhov, M. V, Blackledge, M., and Svergun, D.I.  
1135 (2007). Structural characterization of flexible proteins using small-angle X-ray  
1136 scattering. *J. Am. Chem. Soc.* 129, 5656–5664.
- 1137 Bernadó, P., and Svergun, D.I. (2012). Structural analysis of intrinsically disordered  
1138 proteins by small-angle X-ray scattering. *Mol. BioSyst.* 8, 151–167.
- 1139 Bienkiewicz, E.A., Adkins, J.N., and Lumb, K.J. (2002). Functional consequences of  
1140 preorganized helical structure in the intrinsically disordered cell-cycle inhibitor  
1141 p27Kip1. *Biochemistry* 41, 752–759.
- 1142 Bourguet, W., Ruff, M., Chambon, P., Gronemeyer, H., and Moras, D. (1995). Crystal

1 1143 structure of the ligand-binding domain of the human nuclear receptor RXR- $\alpha$ . Nature  
2 1144 375, 377-82.  
3  
4 1145 Bourguet, W., Vivat, V., Wurtz, J.M., Chambon, P., Gronemeyer, H., and Moras, D.  
5  
6 1146 (2000). Crystal structure of a heterodimeric complex of RAR and RXR ligand-  
7  
8 1147 binding domains. Mol. Cell 5, 289–298.  
9  
10 1148 Brautigam, C.A., Zhao, H., Vargas, C., Keller, S., and Schuck, P. (2016). Integration  
11  
12 1149 and global analysis of isothermal titration calorimetry data for studying  
13  
14 1150 macromolecular interactions. Nat. Protoc. 11, 882–894. Buchan, D.W.A., Minnici, F.,  
15  
16 1151 Nugent, T.C.O., Bryson, K., and Jones, D.T. (2013). Scalable web services for the  
17  
18 1152 PSIPRED Protein Analysis Workbench. Nucleic Acids Res. 41, W349-57.  
19  
20 1153 Chandra, V., Wu, D., Li, S., Potluri, N., Kim, Y., and Rastinejad, F. (2017). The  
21  
22 1154 quaternary architecture of RAR $\beta$ -RXR $\alpha$  heterodimer facilitates domain-domain signal  
23  
24 1155 transmission. Nat. Commun. 8, 868.  
25  
26 1156 Chen, J.D., and Evans, R.M. (1995). A transcriptional co-repressor that interacts with  
27  
28 1157 nuclear hormone receptors. Nature 377, 454–457.  
29  
30 1158 Cordeiro, T.N., Herranz-Trillo, F., Urbanek, A., Estaña, A., Cortés, J., Sibille, N., and  
31  
32 1159 Bernadó, P. (2017a). Small-angle scattering studies of intrinsically disordered  
33  
34 1160 proteins and their complexes. Curr. Opin. Struct. Biol. 42, 15–23.  
35  
36 1161 Cordeiro, T.N., Chen, P.C., De Biasio, A., Sibille, N., Blanco, F.J., Hub, J.S.,  
37  
38 1162 Crehuet, R., and Bernadó, P. (2017b). Disentangling polydispersity in the PCNA-  
39  
40 1163 p15PAF complex, a disordered, transient and multivalent macromolecular assembly.  
41  
42 1164 Nucleic Acids Res. 45, 1501–1515.  
43  
44 1165 Csizmok, V., Follis, A.V., Kriwacki, R.W., and Forman-Kay, J.D. (2016). Dynamic  
45  
46 1166 Protein Interaction Networks and New Structural Paradigms in Signaling. Chem Rev  
47  
48 1167 116, 6424–6462.  
49  
50  
51  
52  
53  
54  
55  
56  
57  
58  
59  
60  
61  
62  
63  
64  
65

1 1168 Dominguez, C., Boelens, R., and Bonvin, A.M.J.J. (2003). HADDOCK: A protein-  
2 1169 protein docking approach based on biochemical or biophysical information. *J. Am.*  
3  
4 1170 *Chem. Soc.* *125*, 1731–1737.  
5  
6 1171 Dosztányi, Z., Csizmok, V., Tompa, P., and Simon, I. (2005). IUPred: Web server for  
7 1172 the prediction of intrinsically unstructured regions of proteins based on estimated  
8  
9 1173 energy content. *Bioinformatics* *21*, 3433–3434.  
10  
11 1174 Dyson, H.J., and Wright, P.E. (2004). Unfolded proteins and protein folding studied  
12 1175 by NMR. *Chem. Rev.* *104*, 3607–3622.  
13  
14 1176 Egea, P.F., Rochel, N., Birck, C., Vachette, P., Timmins, P.A., and Moras, D. (2001).  
15 1177 Effects of ligand binding on the association properties and conformation in solution of  
16 1178 retinoic acid receptors RXR and RAR. *J. Mol. Biol.* *307*, 557–576.  
17  
18 1179 Eyal, E., Najmanovich, R., Mcconkey, B.J., Edelman, M., and Sobolev, V. (2004).  
19 1180 Importance of Solvent Accessibility and Contact Surfaces in Modeling Side-Chain  
20 1181 Conformations in Proteins. *J. Comput. Chem.* *25*, 712–724.  
21  
22 1182 Franke, D., Petoukhov, M. V., Konarev, P. V., Panjkovich, A., Tuukkanen, A.,  
23 1183 Mertens, H.D.T., Kikhney, A.G., Hajizadeh, N.R., Franklin, J.M., Jeffries, C.M., et al.  
24 1184 (2017). ATSAS 2.8: A comprehensive data analysis suite for small-angle scattering  
25 1185 from macromolecular solutions. *J. Appl. Crystallogr.* *50*, 1212–1225.  
26  
27 1186 Germain, P., Iyer, J., Zechel, C., and Gronemeyer, H. (2002). Co-regulator  
28 1187 recruitment and the mechanism of retinoic acid receptor synergy. *Nature* *415*, 187–  
29 1188 192.  
30  
31 1189 Germain, P., Staels, B., Dacquet, C., Spedding, M., and Laudet, V. (2006). Overview  
32 1190 of Nomenclature of Nuclear Receptors. *Pharmacol. Rev.* *58*, 685–704.  
33  
34 1191 Germain, P., Gaudon, C., Pogenberg, V., Sanglier, S., Van Dorsselaer, A., Royer,  
35 1192 C.A., Lazar, M.A., Bourguet, W., and Gronemeyer, H. (2009). Differential Action on

1  
2  
3  
4  
5  
6  
7  
8  
9  
10  
11  
12  
13  
14  
15  
16  
17  
18  
19  
20  
21  
22  
23  
24  
25  
26  
27  
28  
29  
30  
31  
32  
33  
34  
35  
36  
37  
38  
39  
40  
41  
42  
43  
44  
45  
46  
47  
48  
49  
50  
51  
52  
53  
54  
55  
56  
57  
58  
59  
60  
61  
62  
63  
64  
65

1193 Coregulator Interaction Defines Inverse Retinoid Agonists and Neutral Antagonists.  
1194 *Chem. Biol.* *16*, 479–489.  
1195 Glass, C.K., and Rosenfeld, M.G. (2000). The coregulator exchange in transcriptional  
1196 functions of nuclear receptors. *Genes Dev.* *14*, 121–141.  
1197 Gronemeyer, H., Gustafsson, J.Å., and Laudet, V. (2004). Principles for modulation  
1198 of the nuclear receptor superfamily. *Nat. Rev. Drug Discov.* *3*, 950–964.  
1199 Gront, D., Kmiecik, S., and Kolinski, A. (2007). Backbone building from  
1200 quadrilaterals: A fast and accurate algorithm for protein backbone reconstruction from  
1201 alpha carbon coordinates. *J. Comput. Chem.* *28*, 1593–1597.  
1202 Harrus D, Déméné H, Vasquez E, Boulahtouf A, Germain P, Figueira AC, Privalsky  
1203 ML, Bourguet W, le M.A. (2018). Pathological Interactions Between Mutant Thyroid  
1204 Hormone Receptors and Corepressors and Their Modulation by a Thyroid Hormone  
1205 Analogue with Therapeutic Potential. *Thyroid* *28*, 1708-1722.  
1206 Hegyi, H., Schad, E., and Tompa, P. (2007). Structural disorder promotes assembly of  
1207 protein complexes. *BMC Struct Biol* *7*, 65.  
1208 Heinzl, T., Lavinsky, R.M., Mullen, T.M., Söderström, M., Laherty, C.D., Torchia,  
1209 J., Yang, W.M., Brard, G., Ngo, S.D., Davie, J.R., et al. (1997). A complex containing  
1210 N-CoR, mSin3 and histone deacetylase mediates transcriptional repression. *Nature*  
1211 *387*, 43–48.  
1212 Hess, B., Kutzner, C., van der Spoel, D., and Lindahl, E. (2008). GROMACS 4:  
1213 algorithms for highly efficient, load balanced, and scalable molecular simulations. *J.*  
1214 *Chem. Theory Comput.* *4*, 435–447.  
1215 Hörlein, A.J., Näär, A.M., Heinzl, T., Torchia, J., Gloss, B., Kurokawa, R., Ryan, A.,  
1216 Kamei, Y., Söderström, M., Glass, C.K., et al. (1995). Ligand-independent repression  
1217 by the thyroid hormone receptor mediated by a nuclear receptor co-repressor. *Nature*

1218 377, 397–404.

1219 Hu, X., and Lazar, M.A. (1999). The CoRNR motif controls the recruitment of  
1220 corepressors by nuclear hormone receptors. *Nature* 402, 93–96.

1221 Imhof, a, Yang, X.J., Ogryzko, V. V, Nakatani, Y., Wolffe, a P., and Ge, H. (1997).  
1222 Acetylation of general transcription factors by histone acetyltransferases. *Curr. Biol.*  
1223 7, 689–692.

1224 Ishida, T., and Kinoshita, K. (2007). PrDOS: Prediction of disordered protein regions  
1225 from amino acid sequence. *Nucleic Acids Res.* 35.

1226 Iwahara, J., Schwieters, C.D., and Clore, G.M. (2004). Ensemble Approach for NMR  
1227 Structure Refinement against 1H Paramagnetic Relaxation Enhancement Data Arising  
1228 from a Flexible Paramagnetic Group Attached to a Macromolecule. *J. Am. Chem.*  
1229 *Soc.* 126, 5879–5896.

1230 Jensen, M.R., Ruigrok, R.W.H., and Blackledge, M. (2013). Describing intrinsically  
1231 disordered proteins at atomic resolution by NMR. *Curr. Opin. Struct. Biol.* 23, 426-  
1232 35.

1233 Johnson, B.A., and Blevins, R.A. (1994). NMR View: A computer program for the  
1234 visualization and analysis of NMR data. *J. Biomol. NMR* 4, 603–614.

1235 Johnson, B.A., Wilson, E.M., Li, Y., Moller, D.E., Smith, R.G., and Zhou, G. (2000).  
1236 Ligand-induced stabilization of PPARgamma monitored by NMR spectroscopy:  
1237 implications for nuclear receptor activation. *J. Mol. Biol.* 298, 187–194.

1238 Jones, D.T., and Cozzetto, D. (2015). DISOPRED3: Precise disordered region  
1239 predictions with annotated protein-binding activity. *Bioinformatics* 31, 857–863.

1240 Kallenberger, B.C., Love, J.D., Chatterjee, V.K.K., and Schwabe, J.W.R. (2003). A  
1241 dynamic mechanism of nuclear receptor activation and its perturbation in a human  
1242 disease. *Nat. Struct. Biol.* 10, 136–140.

1  
2  
3  
4  
5  
6  
7  
8  
9  
10  
11  
12  
13  
14  
15  
16  
17  
18  
19  
20  
21  
22  
23  
24  
25  
26  
27  
28  
29  
30  
31  
32  
33  
34  
35  
36  
37  
38  
39  
40  
41  
42  
43  
44  
45  
46  
47  
48  
49  
50  
51  
52  
53  
54  
55  
56  
57  
58  
59  
60  
61  
62  
63  
64  
65

1243 Kamisetty, H., Ovchinnikov, S., and Baker, D. (2013). Assessing the utility of  
1244 coevolution-based residue-residue contact predictions in a sequence- and structure-  
1245 rich era. *Proc. Natl. Acad. Sci.* *110*, 15674–15679.  
1246 Klaholz, B.P., Mitschler, A., and Moras, D. (2000). Structural basis for isotype  
1247 selectivity of the human retinoic acid nuclear receptor. *J. Mol. Biol.* *302*, 155–170.  
1248 Konarev, P. V., Volkov, V. V., Sokolova, A. V, Koch, M.H.J., Svergun, D.I., and  
1249 Koch, H.J. (2003). PRIMUS : a Windows PC-based system for small-angle scattering  
1250 data analysis PRIMUS : a Windows PC-based system for small- angle scattering data  
1251 analysis. *Primus* *36*, 1277–1282.  
1252 Krivov, G.G., Shapovalov, M. V., and Dunbrack, R.L. (2009). Improved prediction of  
1253 protein side-chain conformations with SCWRL4. *Proteins Struct. Funct. Bioinforma.*  
1254 *77*, 778–795.  
1255 Kuhlman, B., Dantas, G., Ireton, G.C., Varani, G., Stoddard, B.L., and Baker, D.  
1256 (2003). Design of a Novel Globular Protein Fold with Atomic-Level Accuracy.  
1257 *Science* (80-. ). *302*, 1364–1368.  
1258 Lescop, E., Schanda, P., and Brutscher, B. (2007). A set of BEST triple-resonance  
1259 experiments for time-optimized protein resonance assignment. *J. Magn. Reson.* *187*,  
1260 163–169.  
1261 Lonard, D.M., and O’Malley, B.W. (2007). Nuclear Receptor Coregulators: Judges,  
1262 Juries, and Executioners of Cellular Regulation. *Mol. Cell* *27*, 691–700.  
1263 Lu, J., Cistola, D.P., and Li, E. (2006). Analysis of ligand binding and protein  
1264 dynamics of human retinoid X receptor alpha ligand-binding domain by nuclear  
1265 magnetic resonance. *Biochemistry* *45*, 1629–1639.  
1266 le Maire, A., and Bourguet, W. (2014). Retinoic acid receptors: Structural basis for  
1267 coregulator interaction and exchange. *Subcell. Biochem.* *70*, 37–54.

1268 le Maire, A., Alvarez, S., Shankaranarayanan, P., R de Lera, A., Bourguet, W., and  
1269 Gronemeyer, H. (2012). Retinoid Receptors and Therapeutic Applications of  
1270 RAR/RXR Modulators. *Curr. Top. Med. Chem.* *12*, 505–527.  
1271 le Maire, A., Teyssier, C., Erb, C., Grimaldi, M., Alvarez, S., De Lera, A.R.,  
1272 Balaguer, P., Gronemeyer, H., Royer, C.A., Germain, P., et al. (2010). A unique  
1273 secondary-structure switch controls constitutive gene repression by retinoic acid  
1274 receptor. *Nat. Struct. Mol. Biol.* *17*, 801–807.  
1275 Markley, J.L., Bax, A., Arata, Y., Hilbers, C.W., Kaptein, R., Sykes, B.D., Wright,  
1276 P.E., and Wuethrich, K. (1998). Recommendations for the presentation of NMR  
1277 structures of proteins and nucleic acids - (IUPAC Recommendations 1998). *Pure*  
1278 *Appl. Chem.* *70*, 117–142.  
1279 McKenna, N.J., Lanz, R.B., and O'Malley, B.W. (1999). Nuclear receptor  
1280 coregulators: Cellular and molecular biology. *Endocr. Rev.* *20*, 321–344.  
1281 Mohan, A., Oldfield, C.J., Radivojac, P., Vacic, V., Cortese, M.S., Dunker, A.K., and  
1282 Uversky, V.N. (2006). Analysis of Molecular Recognition Features (MoRFs). *J. Mol.*  
1283 *Biol.* *362*, 1043–1059.  
1284 Nagy, L., Kao, H.-Y., Chakravarti, D., Lin, R.J., Hassig, C.A., Ayer, D.E., Schreiber,  
1285 S.L., and Evans, R.M. (1997). Nuclear Receptor Rerepression Mediated by a Complex  
1286 Containing SMRT, mSin3A, and Histone Deacetylase. *Cell* *89*, 373–380.  
1287 Nagy, L., Kao, H.Y., Love, J.D., Li, C., Banayo, E., Gooch, J.T., Krishna, V.,  
1288 Chatterjee, K., Evans, R.M., and Schwabe, J.W.R. (1999). Mechanism of corepressor  
1289 binding and release from nuclear hormone receptors. *Genes Dev.* *13*, 3209–3216.  
1290 Nahoum, V., de Lera, A.R., and Bourguet, W. (2007). Modulator structure dynamics  
1291 retinoid X receptor rel function agonist antagonist. *Proc. Natl. Acad. Sci. USA* *104*,  
1292 17323-8.

1293 Oteri, F., Nadalin, F., Oteri, F., Nadalin, F., and Carbone, A. (2017). BIS2Analyzer :  
1294 A server for co-evolution analysis of conserved protein families BIS2Analyzer : a  
1295 server for co-evolution analysis of. *Nucleic Acids Res.* *45*.  
1296 Osz, J., Pethoukhov, M. V., Sirigu, S., Svergun, D.I., Moras, D., and Rochel, N.  
1297 (2012). Solution structures of PPAR $\gamma$ 2/RXR $\alpha$  complexes. *PPAR Res.* 701412.  
1298 Ota, H., and Fukuchi, S. (2017). Sequence conservation of protein binding segments  
1299 in intrinsically disordered regions. *Biochem. Biophys. Res. Commun.* *494*, 602–607.  
1300 Ozenne, V., Bauer, F., Salmon, L., Huang, J.R., Jensen, M.R., Segard, S., Bernadó,  
1301 P., Charavay, C., and Blackledge, M. (2012). Flexible-meccano: A tool for the  
1302 generation of explicit ensemble descriptions of intrinsically disordered proteins and  
1303 their associated experimental observables. *Bioinformatics* *28*, 1463–1470.  
1304 Parigi, G., Rezaei-Ghaleh, N., Giachetti, A., Becker, S., Fernandez, C., Blackledge,  
1305 M., Griesinger, C., Zweckstetter, M., and Luchinat, C. (2014). Long-range correlated  
1306 dynamics in intrinsically disordered proteins. *J. Am. Chem. Soc.* *136*, 16201–16209.  
1307 Pavlin, M.R., Brunzelle, J.S., and Fernandez, E.J. (2014). Agonist ligands mediate the  
1308 transcriptional response of nuclear receptor heterodimers through distinct  
1309 stoichiometric assemblies with coactivators. *J. Biol. Chem.* *289*, 24771–24778.  
1310 Perissi, V., and Rosenfeld, M.G. (2005). Controlling nuclear receptors: The circular  
1311 logic of cofactor cycles. *Nat. Rev. Mol. Cell Biol.* *6*, 542–554.  
1312 Perissi, V., Staszewski, L.M., Mcinerney, E.M., Kurokawa, R., Kronen, A., Rose,  
1313 D.W., Lambert, M.H., Milburn, M. V, Glass, C.K., and Rosenfeld, M.G. (1999).  
1314 Molecular determinants of nuclear receptor – corepressor interaction Molecular  
1315 determinants of nuclear receptor – corepressor interaction. *Genes Dev.* *13*, 3198–  
1316 3208.  
1317 Pernot, P., Round, A., Barrett, R., De Maria Antolinos, A., Gobbo, A., Gordon, E.,

1318 Huet, J., Kieffer, J., Lentini, M., Mattenet, M., et al. (2013). Upgraded ESRF BM29  
1319 beamline for SAXS on macromolecules in solution. *J. Synchrotron Radiat.* *20*, 660–  
1320 664.

1321 Pogenberg, V., Guichoul, J.F., Vivat-Hannah, V., Kammerer, S., Pérez, E., Germain,  
1322 P., De Lera, A.R., Gronemeyer, H., Royer, C.A., and Bourguet, W. (2005).  
1323 Characterization of the interaction between retinoic acid receptor/retinoid X receptor  
1324 (RAR/RXR) heterodimers and transcriptional coactivators through structural and  
1325 fluorescence anisotropy studies. *J. Biol. Chem.* *280*, 1625–1633.

1326 Polyhach, Y., Bordignon, E., and Jeschke, G. (2011). Rotamer libraries of spin  
1327 labelled cysteines for protein studies. *Phys. Chem. Chem. Phys.* *13*, 2356–2366.

1328 Remmert, M., Biegert, A., Hauser, A., and Söding, J. (2012). HHblits: Lightning-fast  
1329 iterative protein sequence searching by HMM-HMM alignment. *Nat. Methods* *9*,  
1330 173–175.

1331 Renaud, J.P., Rochel, N., Ruff, M., Vivat, V., Chambon, P., Gronemeyer, H., and  
1332 Moras, D. (1995). Crystal structure of the RAR-gamma ligand-binding domain bound  
1333 to all-trans retinoic acid. *Nature* *378*, 681–689.

1334 Rochel, N., Ciesielski, F., Godet, J., Moman, E., Roessle, M., Peluso-Iltis, C., Moulin,  
1335 M., Haertlein, M., Callow, P., Mély, Y., et al. (2011). Common architecture of  
1336 nuclear receptor heterodimers on DNA direct repeat elements with different spacings.  
1337 *Nat. Struct. Mol. Biol.* *18*, 564–570.

1338 Roeder, R.G. (1998). Role of general and gene-specific cofactors in the regulation of  
1339 eukaryotic transcription. *Cold Spring Harbor Symposia on Quantitative Biology.* *63*,  
1340 201–218.

1341 Schuck, P. (2000). Size-distribution analysis of macromolecules by sedimentation  
1342 velocity ultracentrifugation and Lamm equation modeling. *Biophys. J.*

1343 Van Roey, K., Uyar, B., Weatheritt, R.J., Dinkel, H., Seiler, M., Budd, A., Gibson,  
1344 T.J., and Davey, N.E. (2014). Short linear motifs: Ubiquitous and functionally diverse  
1345 protein interaction modules directing cell regulation. *Chem. Rev.* *114*, 6733-78.  
1346 Salmon, L., Nodet, G., Ozenne, V., Yin, G., Jensen, M.R., Zweckstetter, M., and  
1347 Blackledge, M. (2010). NMR characterization of long-range order in intrinsically  
1348 disordered proteins. *J. Am. Chem. Soc.* *132*, 8407–8418.  
1349 Sato, Y., Ramalanjaona, N., Huet, T., Potier, N., Osz, J., Antony, P., Peluso-Iltis, C.,  
1350 Poussin-Courmontagne, P., Ennifar, E., Mély, Y., et al. (2010). The “phantom effect”  
1351 of the rexinoid LG100754: Structural and functional insights. *PLoS One* *5*, e15119.  
1352 Schulman, I.G., Juguilon, H., and Evans, R.M. (1996). Activation and repression by  
1353 nuclear hormone receptors: hormone modulates an equilibrium between active and  
1354 repressive states. *Mol. Cell. Biol.* *16*, 3807–3813.  
1355 Smith, W.W., Ho, P.Y., and O’Hern, C.S. (2014). Calibrated Langevin-dynamics  
1356 simulations of intrinsically disordered proteins. *Phys. Rev. E - Stat. Nonlinear, Soft*  
1357 *Matter Phys.* *90*, 042709.  
1358 Svergun, D., Barberato, C., and Koch, M.H. (1995). CRY SOL - A program to  
1359 evaluate X-ray solution scattering of biological macromolecules from atomic  
1360 coordinates. *J. Appl. Crystallogr.* *28*, 768–773.  
1361 Svergun, D.I., Semenyuk, A. V., and Feigin, L.A. (1988). Small- angle- scattering-  
1362 data treatment by the regularization method. *Acta Crystallogr. Sect. A* *44*, 244–251.  
1363 Uversky, V.N., and Gillespie, J.R. (2000). Why are "natively unfolded" proteins  
1364 unstructured under physiologic conditions? *Proteins* *41*, 415-27.  
1365 de Vera, I.M.S., Zheng, J., Novick, S., Shang, J., Hughes, T.S., Brust, R., Munoz-  
1366 Tello, P., Gardner, W.J., Marciano, D.P., Kong, X., et al. (2017). Synergistic  
1367 Regulation of Coregulator/Nuclear Receptor Interaction by Ligand and DNA.

1  
2  
3  
4  
5  
6  
7  
8  
9  
10  
11  
12  
13  
14  
15  
16  
17  
18  
19  
20  
21  
22  
23  
24  
25  
26  
27  
28  
29  
30  
31  
32  
33  
34  
35  
36  
37  
38  
39  
40  
41  
42  
43  
44  
45  
46  
47  
48  
49  
50  
51  
52  
53  
54  
55  
56  
57  
58  
59  
60  
61  
62  
63  
64  
65

1368 Structure 25, 1506–1518.e4.

1369 Westin, S., Kurokawa, R., Nolte, R.T., Wisely, G.B., McInerney, E.M., Rose, D.W.,  
1370 Milburn, M. V., Rosenfeld, M.G., and Glass, C.K. (1998). Interactions controlling the  
1371 assembly of nuclear-receptor heterodimers and co-activators. *Nature* 395, 199–202.

1372 Wheeler, T.J., Clements, J., and Finn, R.D. (2014). Skylign: A tool for creating  
1373 informative, interactive logos representing sequence alignments and profile hidden  
1374 Markov models. *BMC Bioinformatics* 15.

1375 Xue, B., Dunbrack, R.L., Williams, R.W., Dunker, A.K., and Uversky, V.N. (2010).  
1376 PONDR-FIT: A meta-predictor of intrinsically disordered amino acids. *Biochim.*  
1377 *Biophys. Acta - Proteins Proteomics* 1804, 996–1010.

1378 Zhang, H., Chen, L., Chen, J., Jiang, H., and Shen, X. (2011). Structural basis for  
1379 retinoic X receptor repression on the tetramer. *J. Biol. Chem.* 286, 24593–24598.

1380 Zhang, J., Hu, X., and Lazar, M. (1999). A novel role for helix 12 of retinoid X  
1381 receptor in regulating repression. *Mol. Cell. Biol.* 19, 6448–6457.

1382 Zheng, J., Chang, M.R., Stites, R.E., Wang, Y., Bruning, J.B., Pascal, B.D., Novick,  
1383 S.J., Garcia-Ordonez, R.D., Stayrook, K.R., Chalmers, M.J., et al. (2017). HDX  
1384 reveals the conformational dynamics of DNA sequence specific VDR co-activator  
1385 interactions. *Nat. Commun.* 8, 923.

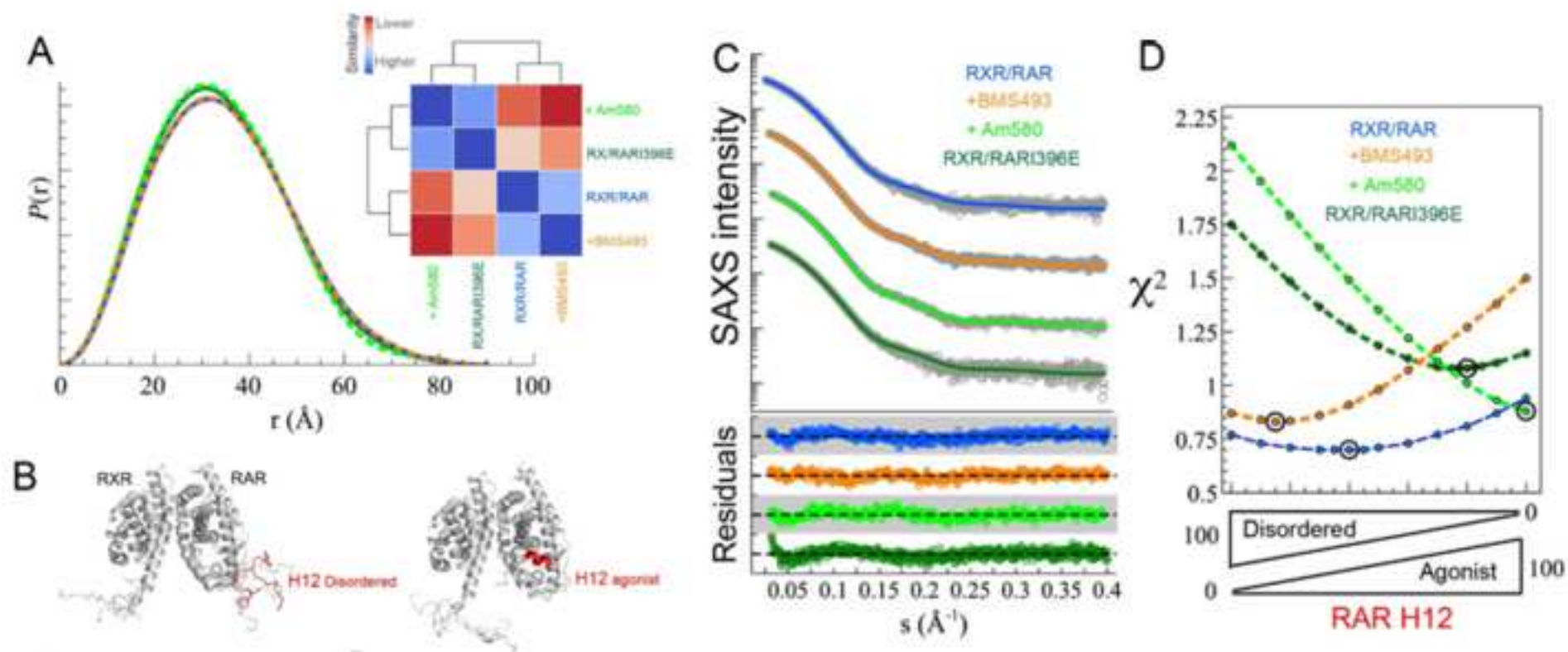
1386

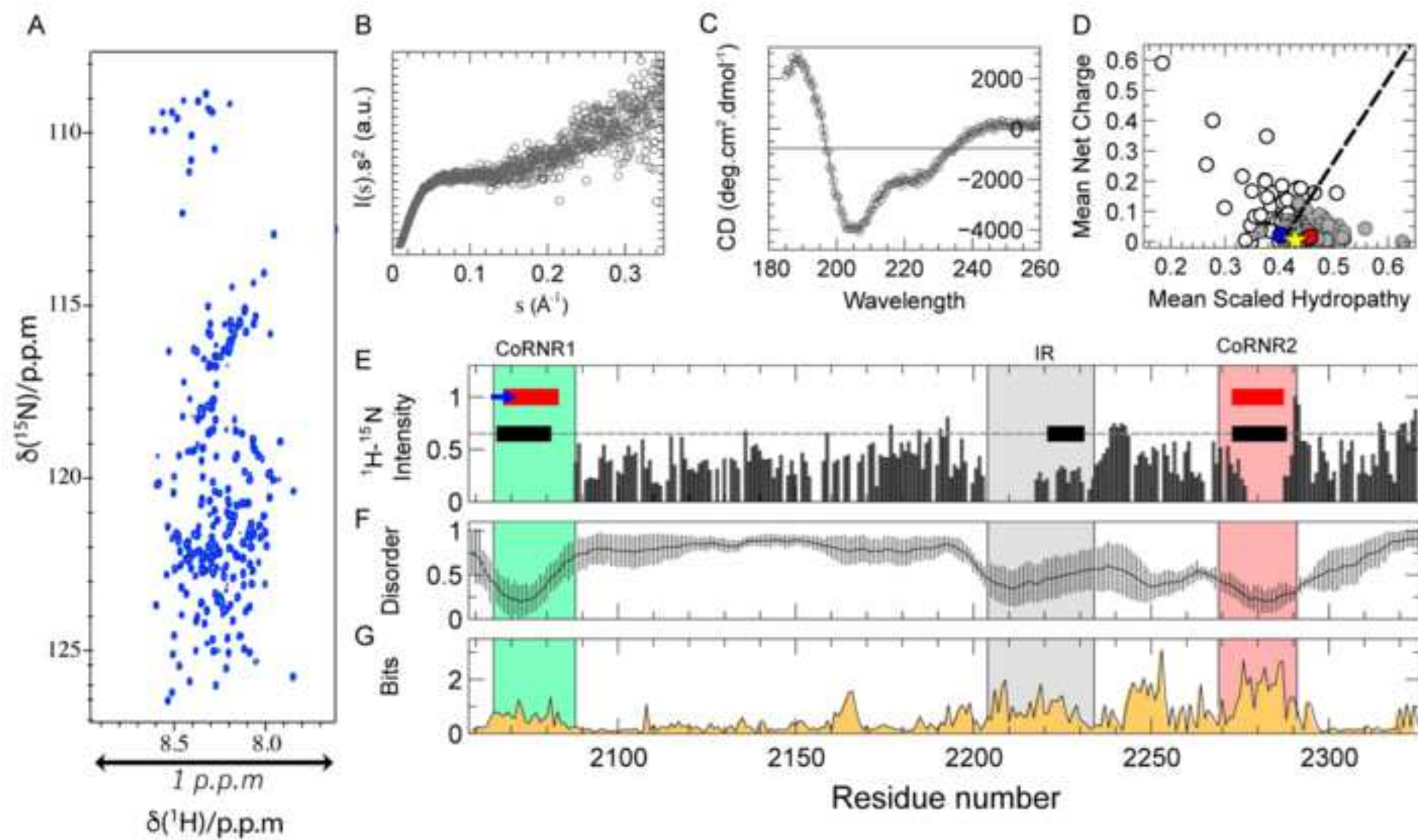
1387

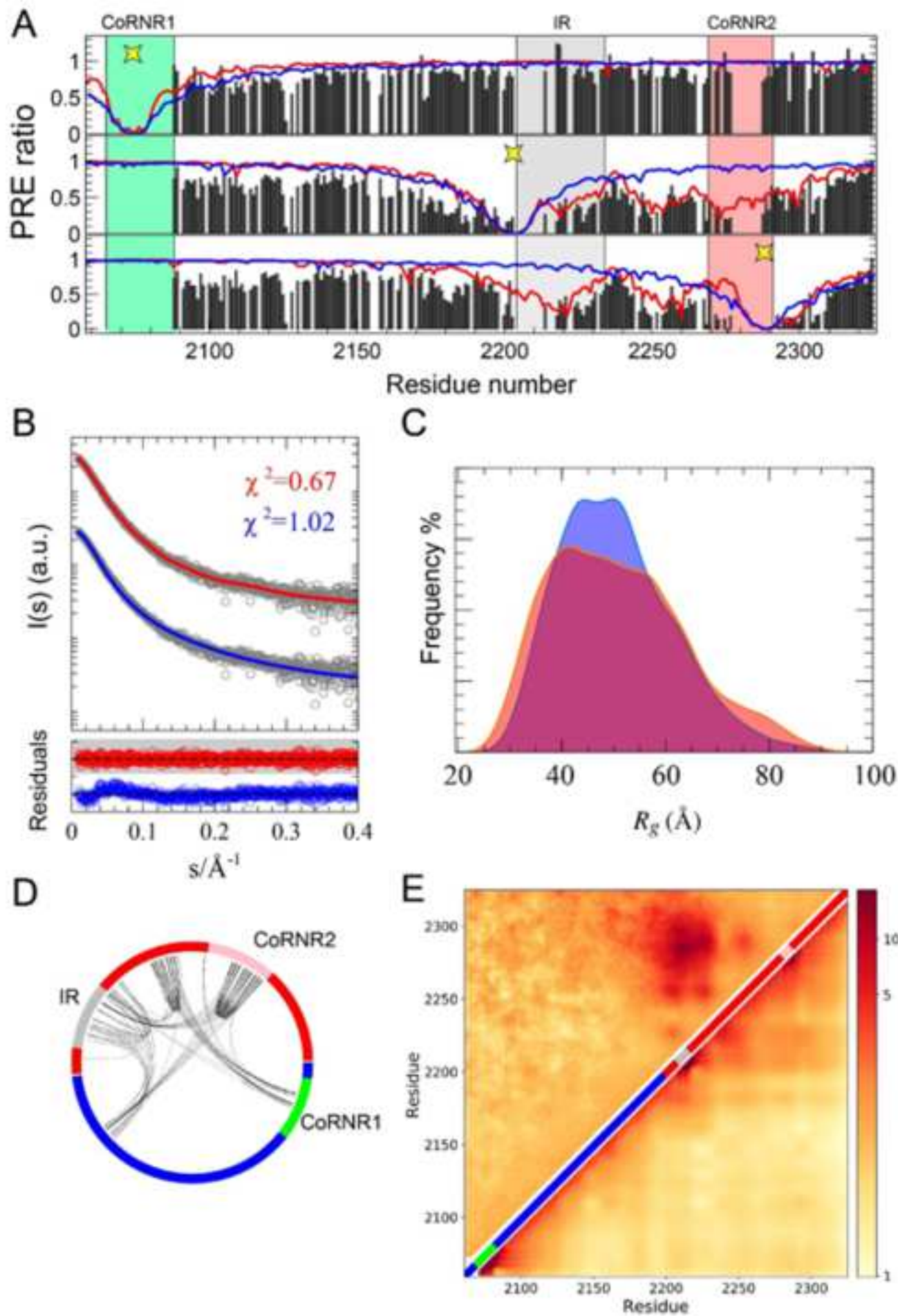
1388

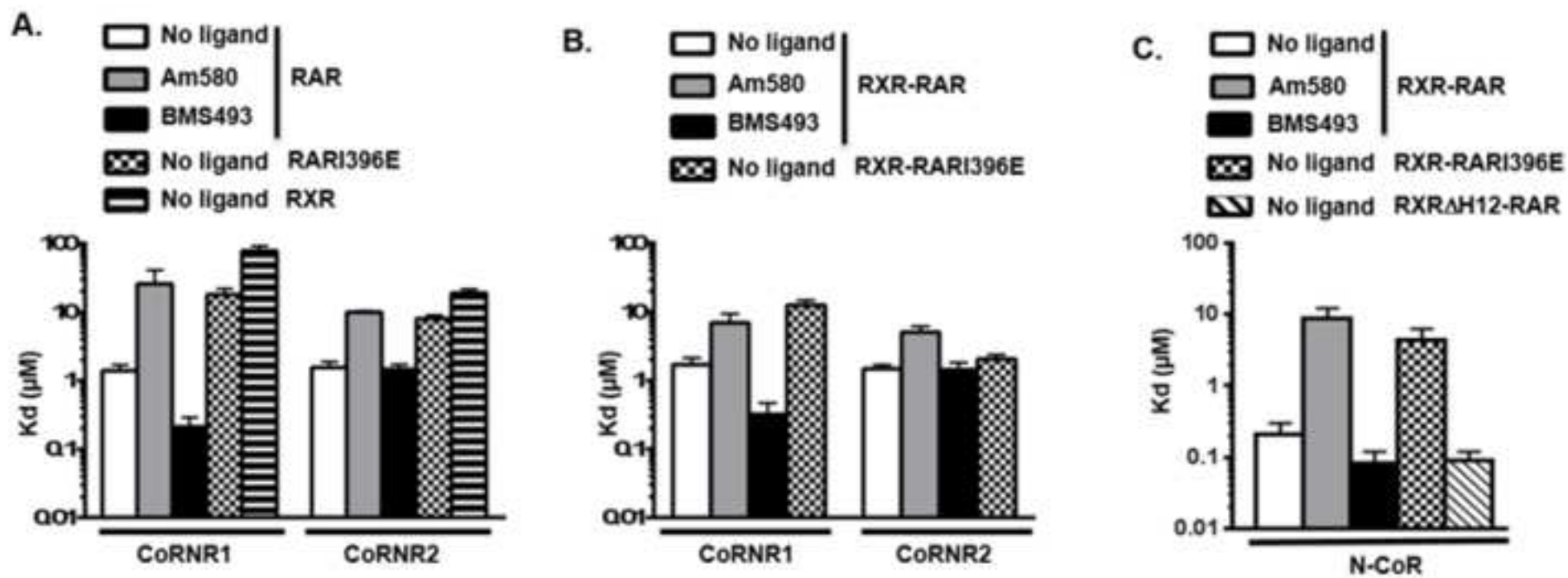
1389

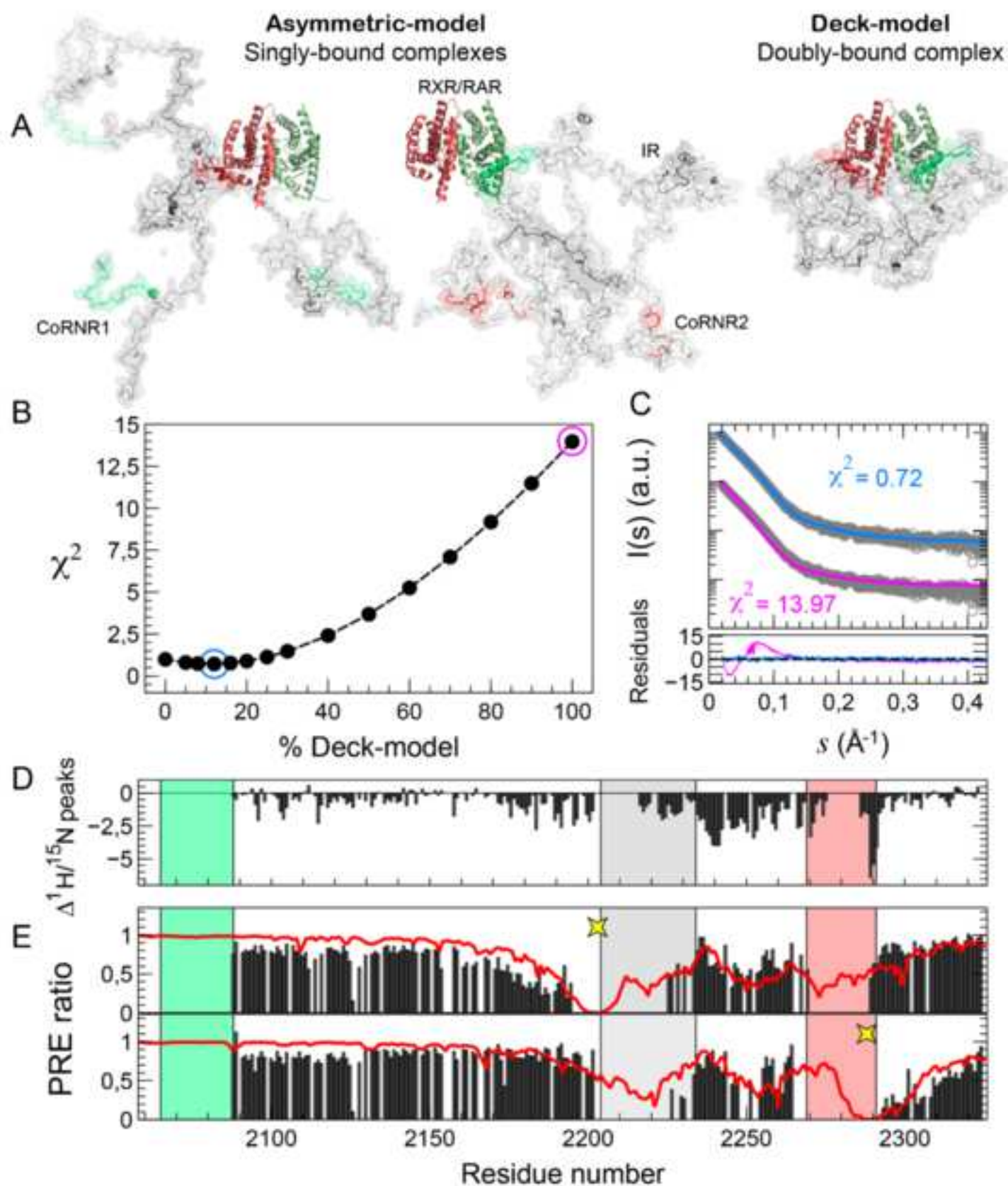
1390

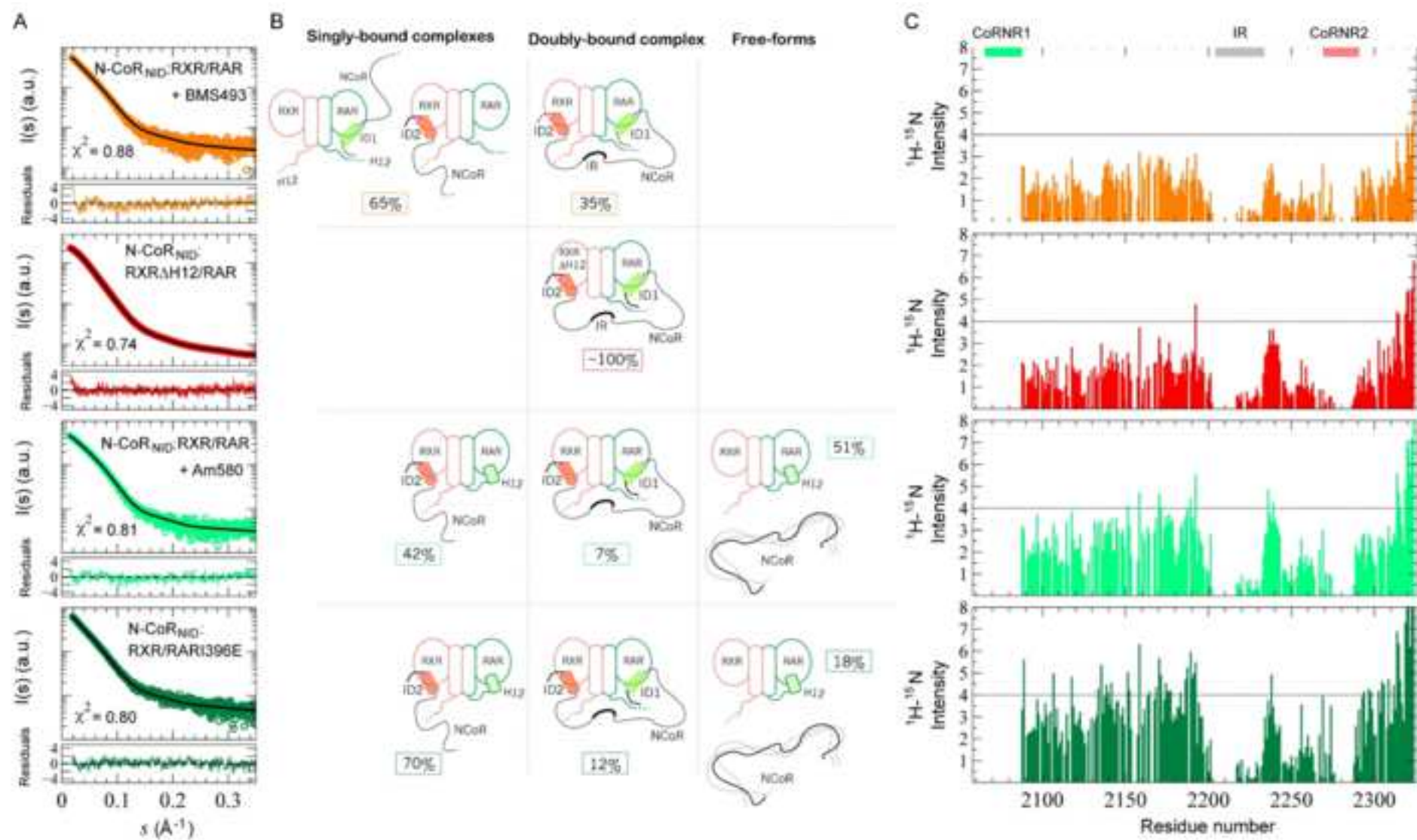






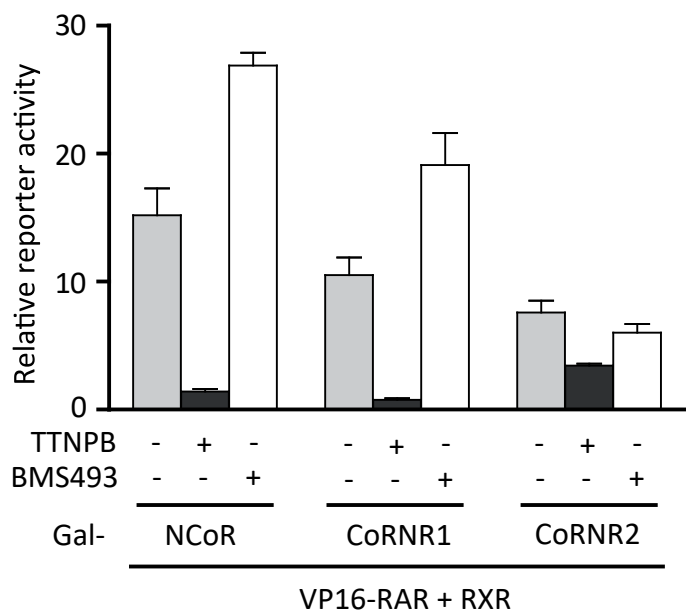




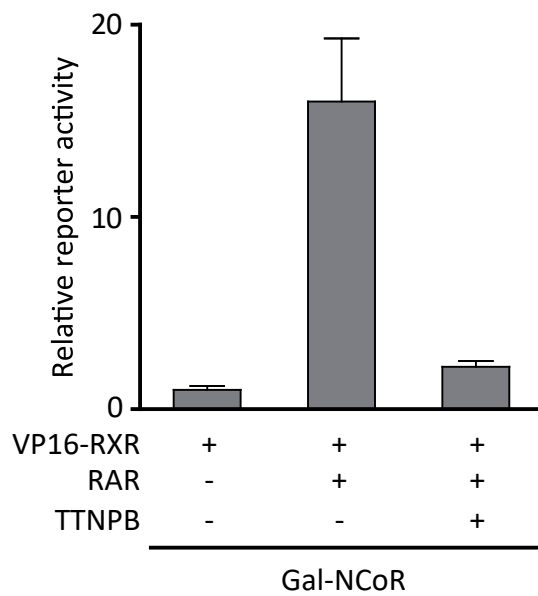


Figure

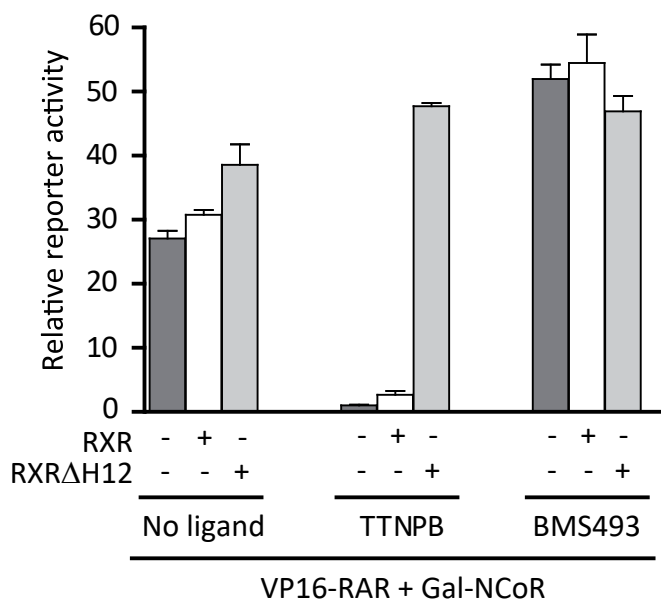
**A**



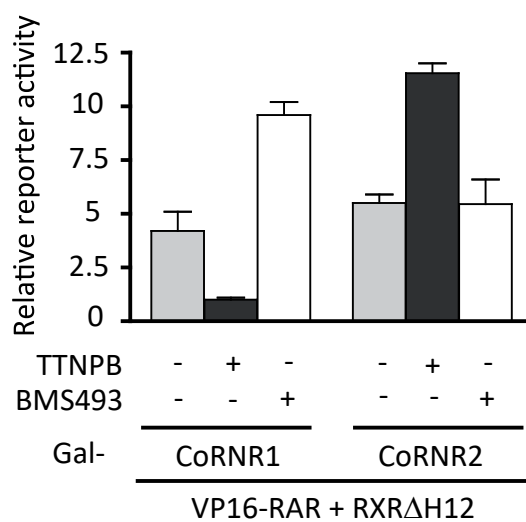
**B**



**C**



**D**





**KEY RESOURCES TABLE**

REAGENT or RESOURCE	SOURCE	IDENTIFIER
Bacterial and Virus Strains		
<i>BL21(DE3)</i>	Novagen	Cat # 69450-4
Chemicals, Peptides, and Recombinant Proteins		
AM580	Tocris Bioscience	<b>Cat. No. 0760/10</b>
BMS493	Tocris Bioscience	<b>Cat. No. 3509/10</b>
TTNPB	Tocris Bioscience	<b>Cat. No. 0761/10</b>
Fluo-N-CoRNR1 (fluorescein-RLITLADHICQIITQDFAR)	EZbiolab	N/A
Fluo-N-CoRNR2 (fluorescein-DPASNLGLEDIIRKALMGSD)	EZbiolab	N/A
Atto647N maleimide	SIGMA-ALDRICH	#05316
MST buffer	NanoTemper Technologies GmbH	N/A
3-(2-Iodoacetamido)-2,2,5,5-tetramethyl-1-pyrrolidinyloxy (IA-PROXYL)	Sigma	#253421
JetPei transfectant	Ozyme	POL101-10N
Critical Commercial Assays		
Luciferase assay system	Promega	E1500
Deposited Data		
Free Nuclear receptor CoRepressor NID	This paper	SASBDB: SASDF34
RXR/RAR Heterodimer:N-CoRNID Complex	This paper	SASBDB: SASDF44
RXR $\Delta$ H12/RAR Heterodimer:N-CoRNID Complex	This paper	SASBDB: SASDF54
RXR/RAR Heterodimer:N-CoRNID Complex with RAR inverse agonist (BMS493)	This paper	SASBDB: SASDF64
RXR/RAR1396E Heterodimer:N-CoRNID Complex	This paper	SASBDB: SASDF74
RXR/RAR Heterodimer:N-CoRNID Complex with RAR agonist (Am580)	This paper	SASBDB: SASDF84
NMR chemical shifts of N-CoRNID	This paper	BMRB: 27848
RXR $\alpha$ (fatty acid)-RAR $\alpha$ (antagonist) structure	(Bourguet et al., 2000)	PDB:1DKF
RXR $\alpha$ (agonist, CoA)-RAR $\beta$ (agonist, CoA) structure	(Pogenberg et al., 2005)	PDB:1XDK
RAR $\alpha$ (agonist, CoA) structure	(le Maire et al., 2010)	PDB:3KMR

RAR $\alpha$ (inverse agonist, CoR) structure	(le Maire et al., 2010)	PDB:3KMZ
RXR $\alpha$ (S-CoR) structure	(Zhang et al., 2011)	PDB:3R29
Experimental Models: Cell Lines		
COS cells	ATCC	CRL-1650
Recombinant DNA		
mRXR $\alpha$ LBD-pET3a	Pogenberg et al. (2005)	N/A
hRAR $\alpha$ LBD-pET15b	Pogenberg et al. (2005)	N/A
hRAR $\alpha$ 1396E LBD-pET15b	le Maire et al. (2010)	N/A
mRXR $\alpha$ $\Delta$ H12 LBD-pET3a	le Maire et al. (2010)	N/A
N-CORNID-PETTEV	Harrus et al. (2018)	N/A
Software and Algorithms		
GraphPad Prism	GraphPad Software	N/A
NT Analysis software	NanoTemper Technologies GmbH	N/A
PSIPRED3.2 server	(Buchan et al., 2013)	N/A
IUPRED	(Dosztányi et al. 2005)	N/A
PrDOS	(Ishida et al. 2007)	N/A
PONDR-FIT	(Xue et al. 2010)	N/A
DISOPRED3	(Jones et al, 2015)	N/A
GREMLIN software	(Kamisetty et al. 2013)	N/A
HHblits	(Remmert et al. 2012)	N/A
SkyIGN	(Wheeler et al. 2014)	N/A
BIS2Analyzer	(Oteri et al. 2017)	N/A
ATSAS Software	(Franke et al. 2017)	N/A
GNOM	(Svergun et al. 1988)	N/A
CRY SOL	(Svergun et al. 1995)	N/A
OLIGOMER	(Konarev et al. 2003)	N/A
NMR View	(Johnson et al. 1994)	N/A
<i>Flexible-Meccano</i>	(Bernado et al. 2005; Ozenne et al. 2012)	N/A
SCCOMP	(Eyal et al. 2004)	N/A
Rosetta 3.5 fixbb module	(Kuhlman et al. 2003)	N/A
Gromacs 5.0.2	(Hess et al. 2008)	N/A
EOM	(Bernado et al. 2007)	N/A
HYCUD	(Parigi et al. 2014)	N/A
GROMACS 5.4	(Abraham et al. 2015)	N/A
HADDOCK	(Dominguez et al. 2003)	N/A
Sedfit software	<a href="http://www.analyticalultracentrifugation.com">http://www.analyticalultracentrifugation.com</a>	N/A
Gussi	<a href="http://biophysics.swmed.edu/MBR/software.html">http://biophysics.swmed.edu/MBR/software.html</a>	N/A
Sednterp	<a href="http://sednterp.unh.edu/">http://sednterp.unh.edu/</a>	

Other		
HiLoad 16/600 Superdex 200	GE Healthcare	Cat#28-9893-35
Safire microplate reader	TECAN	N/A
Monolith NT.115 Premium Coated Capillaries	NanoTemper Technologies GmbH	MO-K025
Monolith NT.115 Microscale Thermophoresis device	NanoTemper Technologies GmbH	N/A
BM29 beamline	ESRF	N/A
950 MHz Bruker Avance III spectrometer equipped with a cryogenic triple-resonance probe	IR-RMN Gif/Yvette	N/A
700 MHz Bruker Avance III spectrometer equipped with a cryogenic triple-resonance probe	In house	N/A
QuikChange Lightning Site-Directed mutagenesis kit	Agilent	# 210518
PD 10 Desalting Columns	GE Healthcare	# 17-0851-01
XLI analytical ultracentrifuge	Beckman, Palo Alto, CA	N/A

## SUPPLEMENTARY INFORMATION FOR

### **Interplay of protein disorder in retinoic acid receptor heterodimer and its corepressor regulates gene expression**

Tiago N. Cordeiro<sup>1,2</sup>, Nathalie Sibille<sup>1</sup>, Pierre Germain<sup>1</sup>, Philippe Barthe<sup>1</sup>, Abdelhay Boulahtouf<sup>3</sup>, Frédéric Allemand<sup>1</sup>, Rémy Bailly<sup>1</sup>, Valérie Vivat<sup>4</sup>, Christine Ebel<sup>5</sup>, Alessandro Barducci<sup>1</sup>, William Bourguet<sup>1</sup>, Albane le Maire<sup>1,6,\*</sup>, Pau Bernadó<sup>1,\*</sup>

<sup>1</sup>Centre de Biochimie Structurale (CBS). CNRS, INSERM, Université de Montpellier. 29, rue de Navacelles. 34090-Montpellier, France

<sup>2</sup>Instituto de Tecnologia Química e Biológica, Universidade Nova de Lisboa, 2790-157 Oeiras, Portugal

<sup>3</sup>IRCM, INSERM, ICM, Univ Montpellier, 34298 Montpellier, France

<sup>4</sup>NovAliX, 67400 Illkirch, France

<sup>5</sup>IBS, Univ. Grenoble Alpes, CEA, CNRS, 38000 Grenoble, France

<sup>6</sup>Brazilian Biosciences National Laboratory (LNBio), Brazilian Center for Research in Energy and Materials (CNPEM), 13083-970 Campinas, Sao Paulo, Brazil.

\*Correspondence: [albane.lemaire@cbs.cnrs.fr](mailto:albane.lemaire@cbs.cnrs.fr); [pau.bernado@cbs.cnrs.fr](mailto:pau.bernado@cbs.cnrs.fr)

**TABLE S1.****Table S1, related to Figure 1. SAXS acquisition and analysis of RXR/RAR heterodimers**

Samples	RXR/RAR	RXR/RAR +BMS493	RXR/RAR +AM580	RXR/RAR1396E
<b>Data Collection Parameters</b>				
Instrument (Pernot et al., 2013)	ESRF-BM29	ESRF-BM29	ESRF-BM29	ESRF-BM29
Wavelength (Å)	0.99	0.99	0.99	0.99
<i>s</i> range (Å <sup>-1</sup> )	0.0031-0.49	0.0031-0.49	0.0031-0.49	0.0032-0.493
Concentration range (mg·mL <sup>-1</sup> )	0.7, 1.4, 2.7, 5.1	0.7, 1.4, 2.7, 5.1	0.7, 1.4, 2.7, 5.1	0.9, 1.93, 3.3, 4.0
Exposure Time (s)	10	10	10	10
Temperature (K)	283	283	283	283
<b>Structural parameters</b>				
<i>I</i> <sub>0</sub> (cm <sup>-1</sup> ) [from <i>P</i> ( <i>r</i> )]	0.3965±0.05	0.4407±0.1	0.3511±0.1	0.4224±0.1
<i>R</i> <sub>g</sub> (Å) [from <i>P</i> ( <i>r</i> )]	26.6±0.4	26.5±0.3	25.6±0.2	26.1±0.2
<i>I</i> <sub>0</sub> (cm <sup>-1</sup> ) [from Guinier]	0.4007	0.4483	0.3584	0.4266
<i>R</i> <sub>g</sub> (Å) [from Guinier]	27.5± 0.2	27.1± 0.3	26.2± 0.4	26.8± 0.3
<i>D</i> <sub>max</sub> (Å)	89.0± 3.0	90.0± 4.0	84.0±2.0	86.0±2.0
Porod volume estimate (Å <sup>3</sup> )	92709.7	91962.5	86092.5	91008.5
<b>Molecular mass determination</b>				
Molecular mass (from <i>I</i> <sub>0</sub> ) (KDa)	53.1±5.0	59.3±6.0	48.7±5.0	55.058±5.0
Calculated MW from sequence (KDa)	54.7	54.7	54.7	54.7
<b>Software</b> (Franke et al., 2017)				
1D data processing	PRIMUS	PRIMUS	PRIMUS	PRIMUS
<i>P</i> ( <i>r</i> )	GNOM	GNOM	GNOM	GNOM
Simulated SAXS	CRYSOL	CRYSOL	CRYSOL	CRYSOL

16  
17  
18  
19  
20  
21  
22  
23  
24  
25  
26  
27  
28  
29  
30  
31  
32  
33  
34  
35  
36  
37  
38  
39  
40  
41  
42  
43  
44  
45  
46  
47  
48  
49  
50  
51  
52  
53  
54  
55  
56  
57  
58  
59  
60  
61  
62  
63  
64  
65

**TABLE S2.**

**Table S2, related to Figure 1 and Figure S1. List of X-ray structures used to generate ensemble models of RXR/RAR for SAXS data interpretation.**

	<b>X-ray structures</b>				
	<b>1DKF</b> RXR $\alpha$ (fatty acid)- RAR $\alpha$ (antagonist)(Bourguet et al., 2000)	<b>1XDK</b> RXR $\alpha$ (agonist, CoA)- RAR $\beta$ (agonist, CoA)(Pogenberg et al., 2005)	<b>3KMR</b> RAR $\alpha$ (agonist, CoA)(le Maire et al., 2010)	<b>3KMZ</b> RAR $\alpha$ (inverse agonist, CoR)(le Maire et al., 2010)	<b>3R29</b> , RXR $\alpha$ (S- CoR)(Zhang et al., 2011)
<b>Models Figure S1</b>					
<b>RXR/RAR-apo, disordered H12s</b>	RXR/RAR disordered RXR (residues 441-467) and disordered RAR H12 (residues 394-421)				
<b>RXR/RAR-apo, antagonist H12s</b>	RXR/RAR RXR H12 antagonist conformation (residues 452-461) and RAR H12 antagonist conformation (residues 410-415)				
<b>RXR/RAR-apo, agonist H12s</b>	RXR RAR RXR H12 agonist conformation (residues 454-459) and RAR H12 agonist conformation (residues 408-414)				
<b>Models Figure 1</b>					
<b>RXR/RAR “agonist”</b>	RXR RAR disordered RXR (residues 441-467) and RAR H12 agonist conformation (residues 408-414)				
<b>RXR/RAR “disordered”</b>	RXR RAR disordered RXR (residues 441-467) and disordered RAR H12 (residues 394-421)				
<b>N-CoR<sub>NID</sub>:RXR/RAR complexes</b>					
Singly bound via RAR, disordered H12s	RXR			RAR:N-CoRNR1	
Singly bound via RXR, disordered H12s	RXR/RAR				S-CoRNR2
Singly bound via RXR, RAR-agonist	RXR		RAR		S-CoRNR2
Doubly bound	RXR			RAR:CoRNR1	S-CoRNR2

16  
17  
18  
19  
20  
21  
22 **TABLE S3.**  
23

24 **Table S3, related to Figure 6. SAXS acquisition and analysis of free N-CoR<sub>NID</sub> and N-CoR<sub>NID</sub>:RXR/RAR complexes.**  
25  
26

	N-CoR <sub>NID</sub>	N-CoR <sub>NID</sub> : RXR/RAR	N-CoR <sub>NID</sub> : RXR/RAR	N-CoR <sub>NID</sub> : RXRΔH12/RAR	N-CoR <sub>NID</sub> : RXR/RARI396E	N-CoR <sub>NID</sub> : RXR/RAR
<b>Ligand</b>	—	—	BMS493	—	—	Am580
<b>SASBDB code</b>	SASDF34	SASDF44	SASDF64	SASDF54	SASDF74	SASDF84
<b>Data-collection parameters</b>						
Instrument	ESRF - BM29	ESRF - BM29	ESRF - BM29	ESRF - BM29	ESRF - BM29	ESRF - BM29
Wavelength (Å)	0.99	0.99	0.99	0.99	0.99	0.99
<i>s</i> range (Å <sup>-1</sup> )	0.0031-0.4952	0.0031-0.4952	0.0031-0.49 52	0.0027-0.445	0.0033-0.497	0.0031-0.497
Concentration range (mg·mL <sup>-1</sup> )	1.3, 1.6, 2.0	0.9, 1.7, 2.6, 4.0, 5.0	0.9, 1.3, 3.5	0.8, 1.2, 2.2, 4.9, 11.2	0.6, 0.9, 3.0, 3.5	0.9, 1.3, 3.5
Exposure Time (s)	10	10	10	10	10	10
Temperature (K)	283	283	283	283	283	283
<b>Structural parameters</b>						
I0 (cm <sup>-1</sup> ) [from Pr]	0.271± 0.04	1.155± 0.1	0.751± 0.1	2.715±0.1	0.849± 0.05	0.507± 0.05
<i>R<sub>g</sub></i> (Å) [from Pr]	50.3± 1	52.8± 2	52.6± 2	42.4± 2	51.3± 2	43.2± 1
I0 (cm <sup>-1</sup> ) [from Guinier]	0.2664	1.1859± 0.1	0.731± 0.1	2.77±0.1	0.804± 0.05	0.5234
<i>R<sub>g</sub></i> (Å) [from Guinier]	47.2± 1.2	48.4± 1.1	47.5± 1.0	42.0± 2	44.9± 1.0	44.2± 0.5
<i>D<sub>max</sub></i> (Å)	177± 6	194± 10	195± 10	157.0± 5	190± 5	172± 10
Porod volume estimate (Å <sup>3</sup> )	101.897	163.06	178.3	182.771	170.65	131.09
<b>Molecular mass determination</b>						
Molecular mass [from I0] (kDa)	26.3± 3.0	120± 10.0	75.6± 8.0	N.D.	82.9± 9.0	50.3± 5.0
Molecular Mass [from sequence] (kDa)	29.17	83.53	83.53	83.53	85.44	83.53
<b>Software</b>						
1D data processing	PRIMUS	PRIMUS	PRIMUS	PRIMUS	PRIMUS	PRIMUS
<i>P</i> ( <i>r</i> )	GNOM	GNOM	GNOM	GNOM	GNOM	GNOM
Simulated SAXS	CRYSOL	CRYSOL	CRYSOL	CRYSOL	CRYSOL	CRYSOL

FIGURE S1.

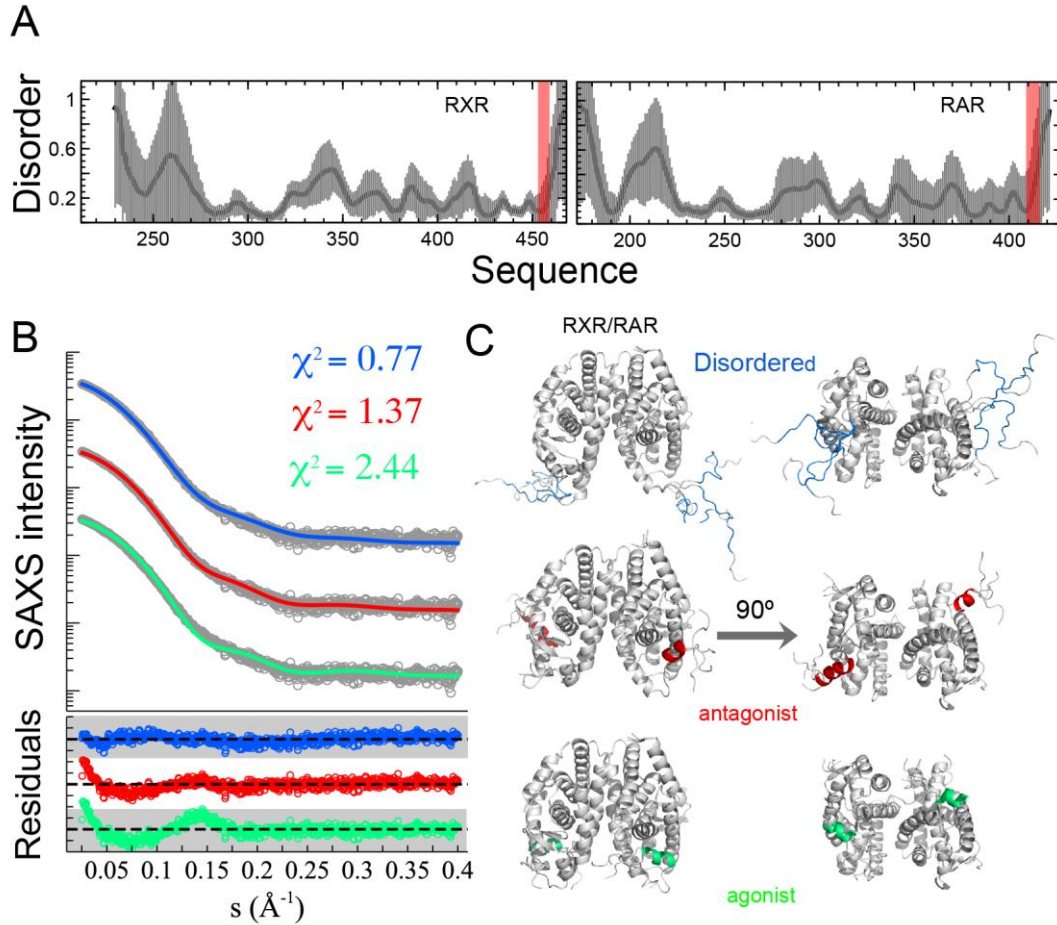


**Figure S1, related to Figure 1: SAXS analysis of RXR/RAR heterodimer.** (A) Average disorder prediction (solid grey line) and its standard deviation computed using different computational tools along the RXR and RAR LBD primary sequence. The limits of RXR H12 (residues 454-459) and RAR H12 (residues 408-414) are displayed in red. (B) The experimental SAXS profile for RXR/RAR in solution (black open circles) is compared with profiles derived from the structural models of the heterodimer displayed in (C). Point-by-point residuals for each model are shown at the bottom with the same colour code. The shaded regions correspond to  $\pm 5$  residual points. (C) Cartoon representations of the ligand-binding domain (LBD) of RXR/RAR models generated based on the X-ray structures referred on Table S2 (both helices H12 disordered, in antagonist and agonist conformations in the blue, red and green models, respectively).

16  
17  
18  
19  
20  
21  
22  
23  
24  
25  
26  
27  
28  
29  
30  
31  
32  
33  
34  
35  
36  
37  
38  
39  
40  
41  
42  
43  
44  
45  
46  
47  
48  
49  
50  
51  
52  
53  
54  
55  
56  
57  
58  
59  
60  
61  
62  
63  
64  
65

FIGURE S2.

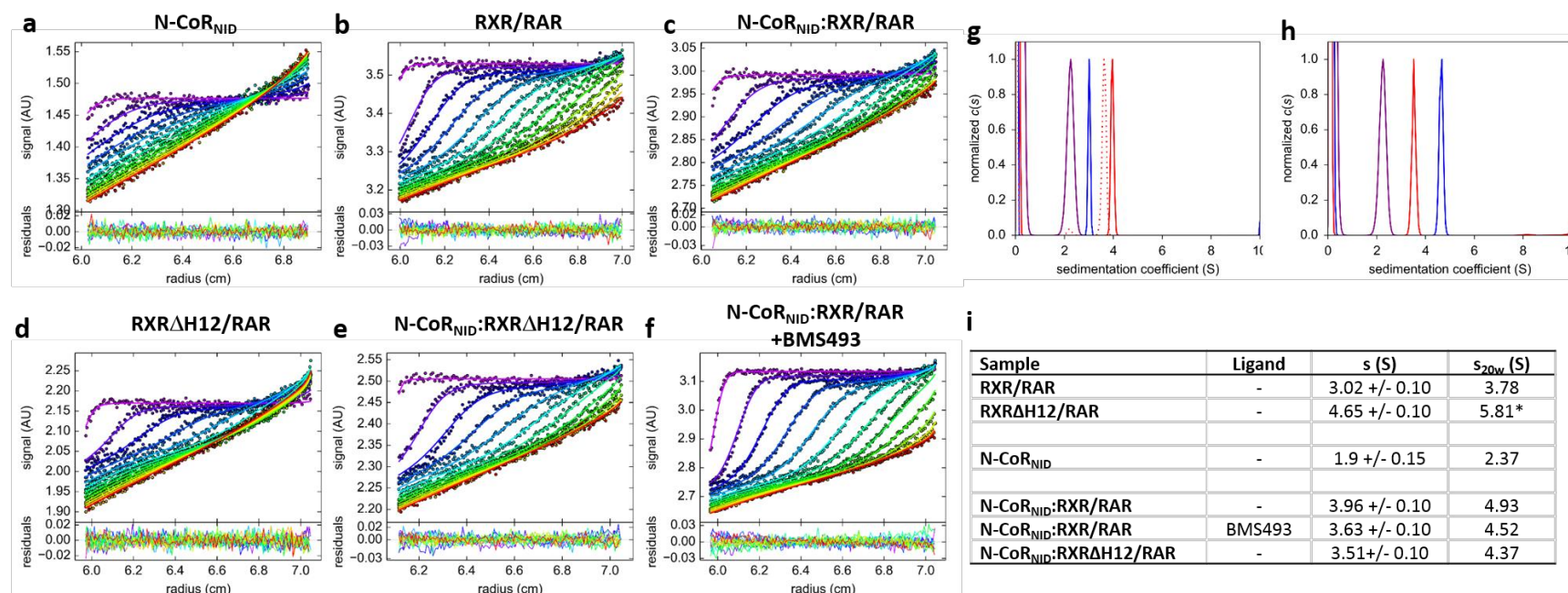
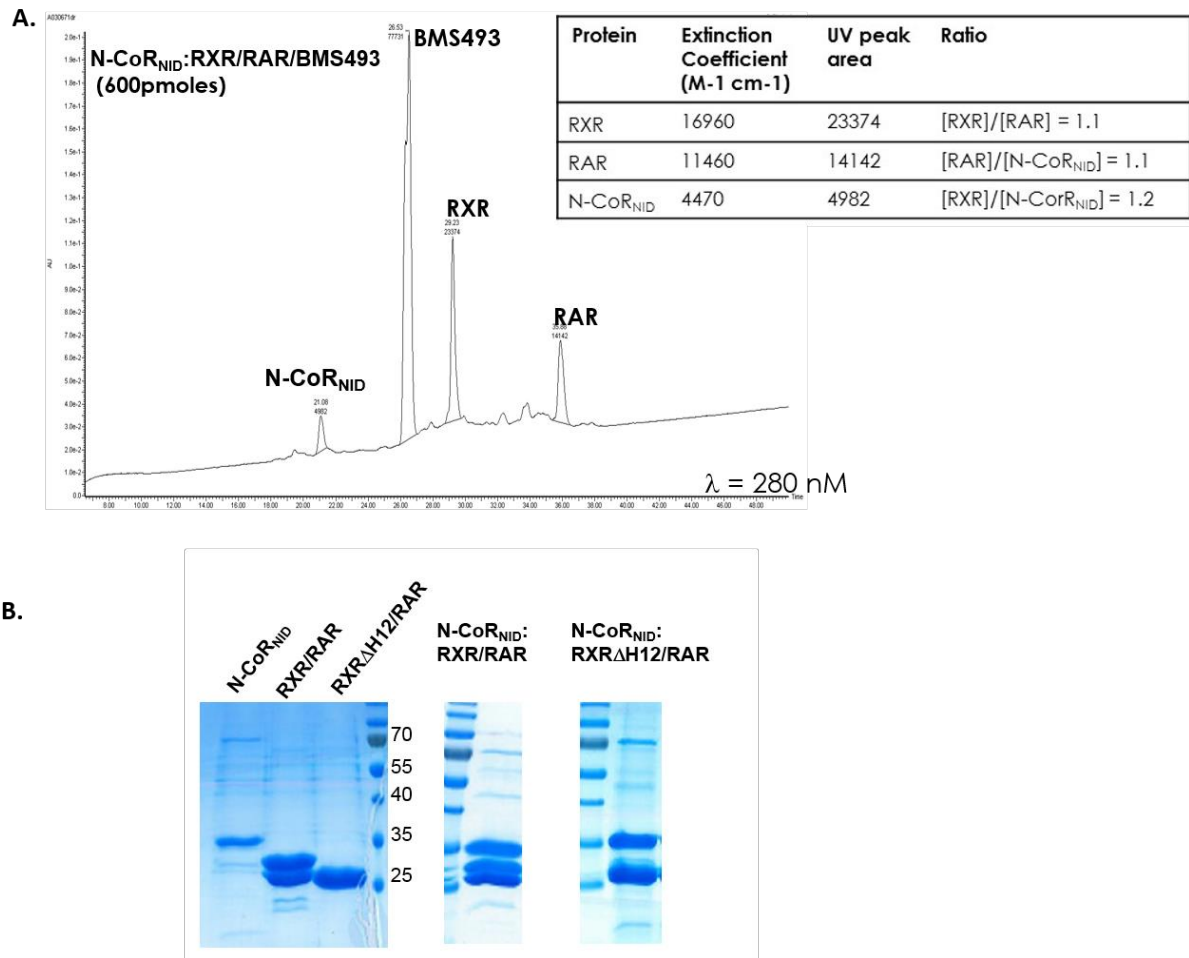


**Figure S2, related to Figures 1 and 2: Biophysical parameters derived from Analytical Ultracentrifugation Sedimentation velocity experiments.** (a-f) Sedimentation velocity of N-CoR<sub>NID</sub>, RXR/RAR, RXRΔH12/RAR and complexes. Superposition of selected experimental and fitted sedimentation velocity profiles obtained every 45 min. at 42,000 rpm, 12 °C, at 295 nm (top subpanels) and their differences (bottom subpanels). (g-h) Sedimentation coefficient distributions *c*(*s*) for N-CoR<sub>NID</sub> (purple), RXR/RAR (blue, g) or RXRΔH12/RAR (blue, h), N-CoR<sub>NID</sub>:RXR/RAR (continuous red, g) or N-CoR<sub>NID</sub>:RXRΔH12/RAR (continuous red, h) and N-CoR<sub>NID</sub>:RXR/RAR/BMS493 (dotted red) complexes. Protein concentration in each sample was about 1 g/L. (i) Experimental (*s*) and corrected to water at 20°C (*s*<sub>20w</sub>) sedimentation coefficients for free and bound forms of RXR/RAX and N-CoR<sub>NID</sub>. All species except RXRΔH12-RAR were considered with the lowest possible association state, since other stoichiometry would correspond to very elongated shapes. Note that in its unliganded form, the RXRΔH12/RAR heterodimer forms a dimer in solution, as observed in gel filtration.



FIGURE S4.



37  
38  
39  
40  
41  
42  
43  
44  
45  
46  
47  
48  
49  
50  
51  
52  
53  
54  
55  
56  
57  
58  
59  
60  
61  
62  
63  
64  
65

**Figure S4, related to Figure 5: Characterization of N-CoR<sub>NID</sub>:RXR-RAR complex.** (A) UV chromatogram ( $\lambda$  280nm) of the complex N-CoR<sub>NID</sub>:RXR-RAR in the presence of BMS493 submitted to RPLC. Theoretical extinction coefficients and UV peak area were used to determine the relative abundance of RXR, RAR and N-CoR<sub>NID</sub>. As shown in the table, quasi stoichiometric ratios were obtained for all three proteins. (B) Coomassie-stained SDS-PAGE of N-CoR<sub>NID</sub>, RXR-RAR, RXR $\Delta$ H12-RAR and the corresponding complexes after the final purification step.

FIGURE S5.

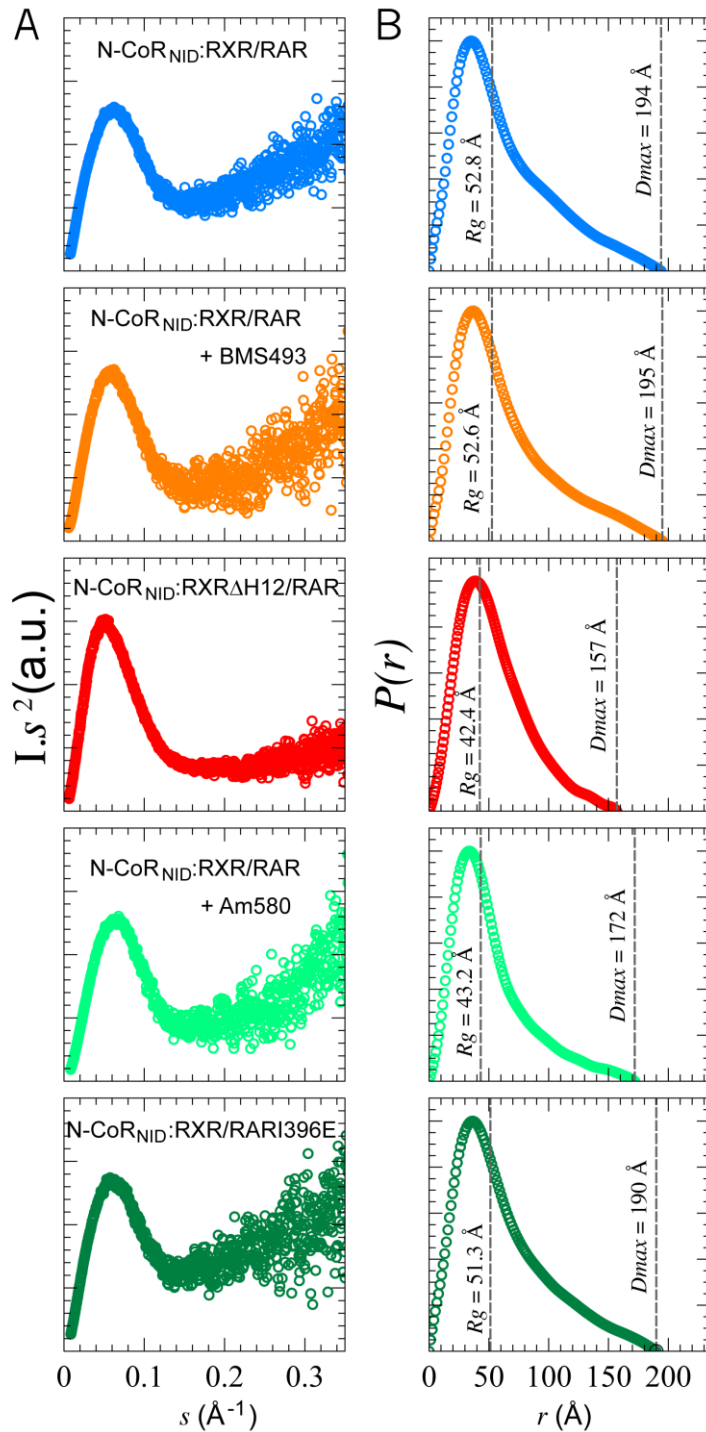


Figure S5, related to Figures 5 and 6: SAXS analysis of N-CoRNID:RXR/RAR complexes. (A) Kratky representations of SAXS intensity versus momentum transfers (open circles) of N-CoRNID:RXR/RAR in the absence of ligand (blue), in the presence of inverse agonist BMS493 (orange) or agonist Am580 (light green), as well as N-CoRNID:RXR $\Delta$ H12/RAR (red) and N-CoRNID:RXR/RARI396E (green) variants. (B) Asymmetric  $P(r)$  functions determined from each SAXS data are in the same colour code. The derived  $R_g$  and  $D_{max}$  values are displayed in dashed lines.

FIGURE S6.

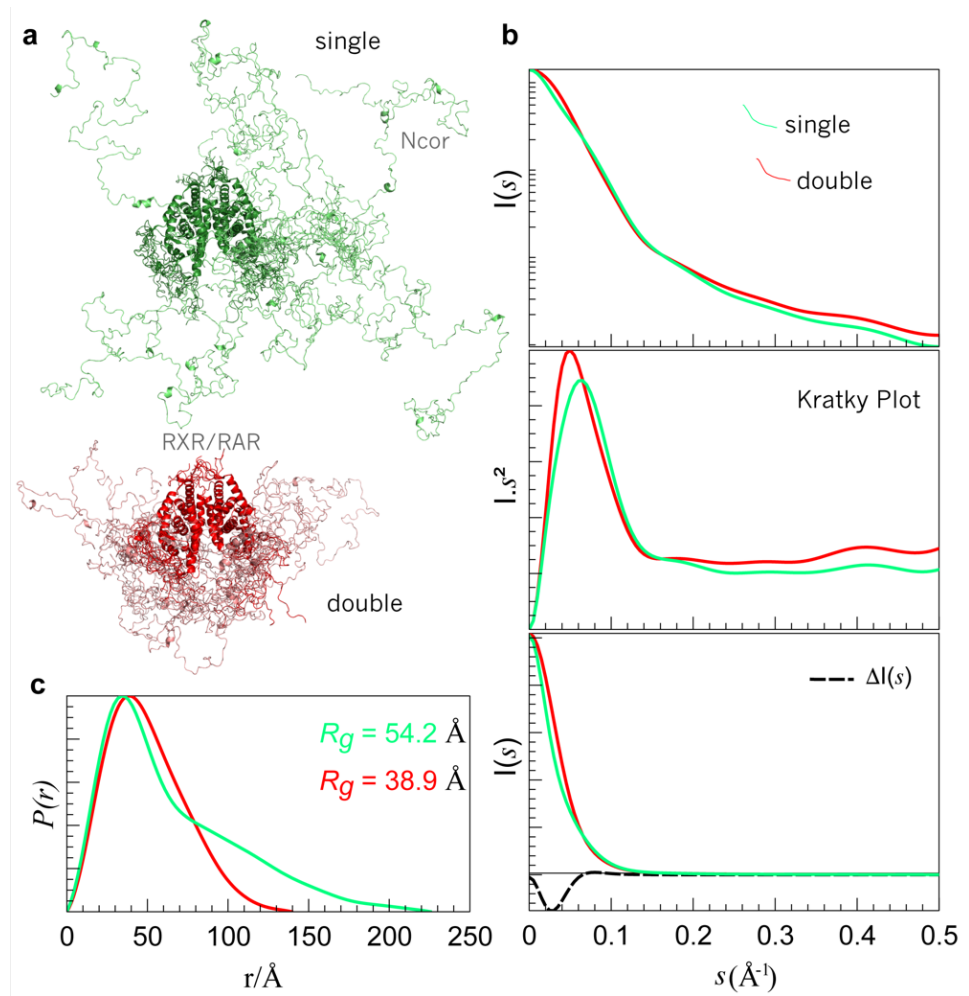
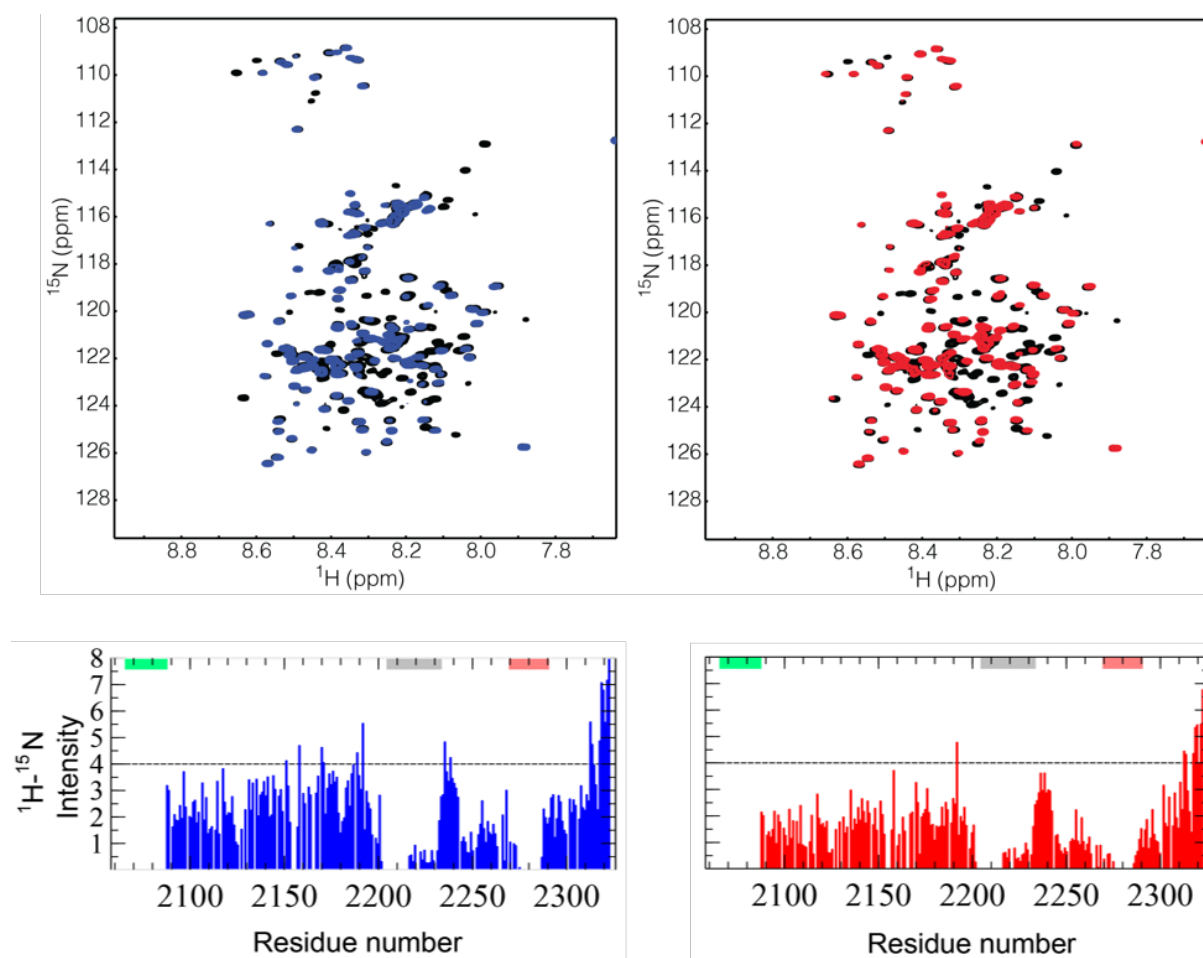


Figure S6, related to Figure 5: SAXS properties of the simulated N-CoR<sub>NID</sub>:RXR-RAR complexes. (A) Cartoon representations and ensemble models for both structural models: asymmetric singly-bound (green) and deck doubly-bound model (red). Theoretical SAXS profiles and Kratky plots (B) and  $P(r)$  (C) from both models with the same colour code. The difference between the two SAXS curves in absolute scale is depicted as a dashed black line in the bottom panel of (B).

FIGURE S7.



**Figure S7, related to Figure 6: Interaction of N-CoRN<sub>NID</sub> with RXR/RAR heterodimers.** (A)  $^1\text{H}$ - $^{15}\text{N}$  HSQC's of  $^{15}\text{N}$  labelled N-CoRN<sub>NID</sub> free in solution (black) and in the presence of equimolar concentration of RXR-RAR (blue, left), and RXR $\Delta$ H12-RAR (red, right). The spectra show that no chemical shift variation or the appearance of additional peaks in the presence of the partners, and only a decrease of intensity due to the increased molecular tumbling of N-CoRN<sub>NID</sub> as observed in the bottom panels for both complexes with the same color code.